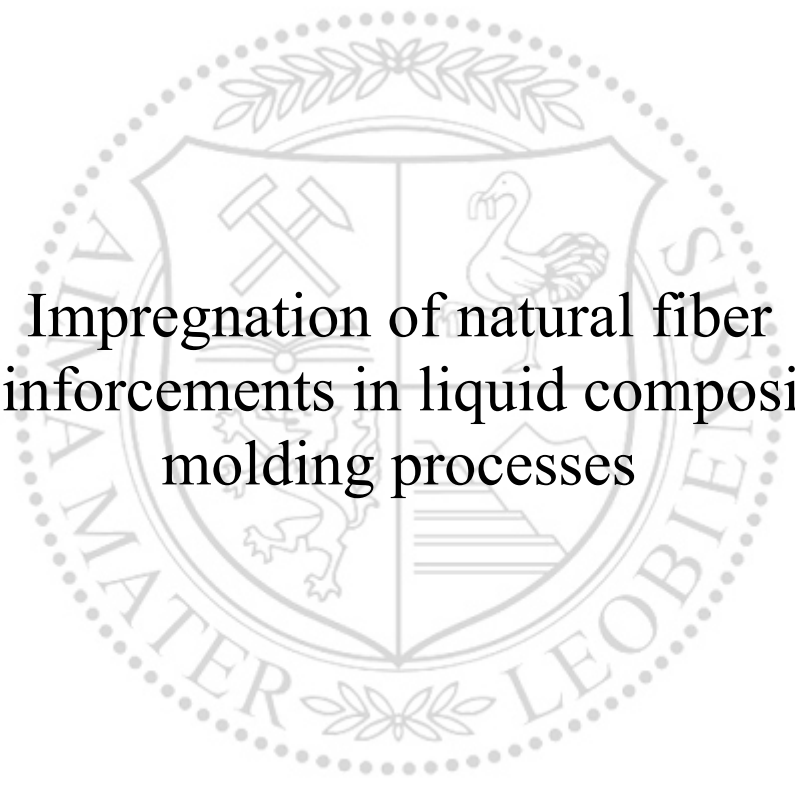




Chair of Processing of Composites

Doctoral Thesis



Impregnation of natural fiber
reinforcements in liquid composite
molding processes

Yannick Blößl, M.Sc.

April 2021



EIDESSTÄTLICHE ERKLÄRUNG

Ich erkläre an Eides statt, dass ich diese Arbeit selbständig verfasst, andere als die angegebenen Quellen und Hilfsmittel nicht benutzt, und mich auch sonst keiner unerlaubten Hilfsmittel bedient habe.

Ich erkläre, dass ich die Richtlinien des Senats der Montanuniversität Leoben zu "Gute wissenschaftliche Praxis" gelesen, verstanden und befolgt habe.

Weiters erkläre ich, dass die elektronische und gedruckte Version der eingereichten wissenschaftlichen Abschlussarbeit formal und inhaltlich identisch sind.

Datum 28.04.2021

Unterschrift Verfasser/in
Yannick Blöchl

Acknowledgements

Main parts of this research work were done within the context of the projects “Reliable and Sustainable composite production for Biobased Components” (RSBC) [Contract No. 858688] and “Green Composites for Green Technologies” (Green2Green) [Contract No. 848668], funded by the Ministry for Transportation, Innovation and Technology (BMVIT) in frame of the research, technology and innovation initiative “Production of the Future”. I kindly acknowledge the possibilities for my research work which were given to me in the course of these projects.

Many thanks to the people and colleagues who supported the progress of my work and actively participate on that fascinating research field.

Abstract

Natural fiber reinforced plastics (NFRP) becoming increasingly popular as an alternative for fully synthetic construction materials. They offer specific advantages like an excellent lightweight potential and a smaller ecological footprint which makes them part of bioeconomic strategies to achieve climate targets and to reduce dependencies from non-renewable resources. The recent developments related to bio-based polymer systems led to synergetic effects since their usage for NFRPs further increases the content of renewable resources while providing good mechanical performance. In this context, liquid composite molding (LCM) processes like resin transfer molding (RTM) enable the production of high quality, durable composites based on thermoset resin systems.

The present work addresses the characterization of the impregnation properties of common flax fiber reinforcements with different textile architectures. Besides the state-of-the-art permeability determination, the analysis of the capillary driven saturation effects is focused. The reinforcing fabrics are prone to flow-induced void formation during impregnation due to their complex pore morphology. These voids can detrimentally affect the mechanical properties of the resulting composite. Therefore, the main objective in this work is the development of a methodical approach to derive optimal impregnation velocities for natural fiber reinforcements in LCM processes.

Experimental series were conducted based on a specially developed test stand for capillary rise experiments. The textile-specific dynamic flow was modeled based on an adjusted version of the Ludwig-Washburn equation, which offers high accuracies for the description of the capillary driven saturation processes. Based on the experimental results, an approach to determine optimal impregnation velocities was applied and verified via an RTM test series. The comparison between the optimization approach and the empirical test results indicates the velocity range for optimal impregnation conditions for the considered flax fiber reinforcements. Therefore, the present investigations on the methodical optimization of the textile impregnation make a considerable contribution to the manufacturing of NFRP products with high quality and reliability.

Kurzfassung

Naturfaserverstärkte Kunststoffe (NFK) erfreuen sich als Alternative zu vollständig synthetischen Konstruktionswerkstoffen zunehmender Beliebtheit. Neben ihren spezifischen Vorteilen wie beispielsweise ein exzellentes Leichtbaupotential und eine potenziell gute Ökobilanz sind sie Teil bioökonomischer Strategien zur Erfüllung von Klimaschutzzielen und zur Reduktion der Abhängigkeit von nicht-erneuerbaren Rohstoffen. Synergieeffekte ergeben sich darüber hinaus aus der Entwicklung biobasierter Kunststoffe, die, eingesetzt als Matrixkomponente im NFK, den erneuerbaren Anteil im Verbundmaterial bei gleichzeitig gutem mechanischen Eigenschaftsprofil erhöhen. Flüssigimprägnierprozesse wie das Resin Transfer Molding (RTM) Verfahren stellen dabei eine Verarbeitungsvariante für Duomere dar, um qualitativ hochwertige und mechanisch belastbare NFK Komponenten herzustellen.

Die vorliegende Arbeit beschäftigt sich mit der Charakterisierung der Imprägniereigenschaften von gängigen Flachfaserverstärkungen mit unterschiedlicher Textilarchitektur. Neben den etablierten Verfahren zur Permeabilitätsbestimmung liegt der Fokus auf ergänzende Analysen, um das kapillare Sättigungsverhalten während der Flüssigimprägnierung zu berücksichtigen. Aufgrund der komplexen Porenmorphologie innerhalb der Faserverstärkungen kommt es während des Füllvorganges mit der flüssigen Matrixkomponente zu Einschlüssen, die sich negativ auf die mechanischen Eigenschaften des resultierenden Faserverbundwerkstoffes auswirken können. Das übergeordnete Ziel der Arbeit ist daher die Entwicklung eines methodischen Ansatzes zur Ableitung optimaler Imprägniergeschwindigkeiten für den Verarbeitungsprozess.

Unter Verwendung eines eigens entwickelten Prüfstandes werden kapillare Steighöhenversuche an den Verstärkungstextilien durchgeführt. Zur Beschreibung des dynamischen Fließvorgangs wird auf Basis der Ludwig-Washburn Gleichung eine modifizierte Version abgeleitet, die das textilabhängige Sättigungsverhalten mit hoher Genauigkeit beschreibt. Die Versuchsergebnisse werden anschließend für einen Ansatz zur Berechnung optimaler Füllgeschwindigkeiten verwendet und

anhand einer RTM Testserie validiert. Die Gegenüberstellung des Optimierungsansatzes und der empirischen Ergebnisse zeigt dabei den Bereich optimaler Prozessgeschwindigkeiten für die berücksichtigten Textilien. Die Untersuchungen zur methodischen Optimierung der Textilimprägnierung liefern folglich einen wertvollen Beitrag zur zuverlässigen Herstellung qualitativ hochwertiger NFK Produkte.

Table of contents

Affidavit	II
Acknowledgements	III
Abstract	IV
Kurzfassung	V
Table of contents	VII
Abbreviations and symbols	X
1 Introduction and Motivation	1
1.1 The use of natural fibers for fiber reinforced plastic products.....	3
1.2 Liquid composite molding processes	5
1.3 Scope and Objectives of this work	8
2 State of the art and Theoretical principles	10
2.1 Properties of natural (plant-based) fiber reinforcements	10
2.1.1 Fiber reinforcements and Textile architectures.....	14
2.1.2 Surface characteristics of natural fibers.....	15
2.2 Process-relevant characteristics of fibrous reinforcements	18
2.2.1 Compaction properties	18
2.2.2 Permeability characteristics.....	21
2.2.3 Capillary effects.....	28
2.3 Thermoset matrix systems	42
2.4 Flow-induced void formation in liquid composite molding processes	44

3	Materials.....	50
3.1	Flax fiber reinforcements.....	50
3.2	Epoxy resin system.....	53
4	Characterization of the in-plane permeability.....	55
4.1	Experimental setup.....	55
4.2	Test results and discussion.....	60
5	Investigations on the capillary action	66
5.1	Experimental setup	67
5.1.1	Camera image and Load-cell calibration	68
5.1.2	Test fluid properties	69
5.1.3	Experiment procedure and Test configurations	74
5.2	Data evaluation	76
5.2.1	Fluid height detection	77
5.2.2	Fluid mass intake.....	79
5.2.3	Application of the Capillary rise model.....	82
5.3	Test results	88
5.3.1	Dependence on the fabric architecture.....	89
5.3.2	Dependence on the fluid properties.....	100
5.4	Discussion.....	110
5.4.1	Optimization of the fiber impregnation in liquid composite molding processes.....	110
5.4.2	The capillary pressure and its contribution on the permeability determination	115
6	Analysis of flow-induced voids in resin transfer molding processes ..	118
6.1	Experimental setup	118

6.2	Test results	122
6.2.1	Impregnation velocities	122
6.2.2	Void contents	125
6.2.3	Mechanical properties	129
6.3	Discussion	131
6.3.1	Application of the Capillary number optimization approach	131
6.3.2	Appropriate measures for void reduction	136
7	Summary and Conclusion	139
	Literature	142
A	Appendix	160
A.1	Navier-Stokes equation for incompressible fluids	160
A.2	Continuity equation for incompressible fluids	162
A.3	Derivation of the velocity profile for steady laminar flow (Poiseuille flow) through a circular tube	163
A.4	Regression functions for the test fluid properties used for the capillary rise experiments	166
	Publications	167

Abbreviations and symbols

List of abbreviations:

Abbreviation	Term
LCM	Liquid composite molding
FRP	Fiber reinforced plastic
GFRP	Glass fiber reinforced plastic
CFRP	Carbon fiber reinforced plastic
NFRP	Natural fiber reinforced plastic
VARI	Vacuum assisted resin infusion
RTM	Resin transfer molding
NCF	Non-crimp fabric
NoE	Number of experiments
L-W	Ludwig-Washburn model
CKm	Carman-Kozeny model (modified)
NW300	Non-woven flax fiber fabric 'Fibrimat F300'
NW450	Non-woven flax fiber fabric 'Fibrimat F450'
W200	Woven flax fiber fabric 'Biotex Flax 200g/m ² 2x2 Twill'
W400	Woven flax fiber fabric 'Biotex Flax 400g/m ² 2x2 Twill'
UD300	Unidirectional flax fiber fabric 'ampliTex [®] Art. No. 5009'
DEC	n-Decane
IPA	2-Propanol
PDMS	Polydimethylsiloxane

List of symbols:

Symbol	SI Unit	Explanation
FAW	kg/m^2	Fabric areal weight
γ	N/m	Surface energy
γ_l	N/m	Liquid surface tension
θ	$^\circ$	Solid-liquid contact angle
V_f	m^3	Fiber volume
V_p	m^3	Pore volume (Free volume in dry reinforcement)
φ	%	Fiber volume fraction
ϕ	%	Porosity fraction (Free volume content of the dry fibrous preform)
m_f	kg	Fiber weight
ρ_f	kg/m^3	Fiber density
A_{tex}	m^2	Areal dimensions of the preform / textile cutting
t	m	Preform thickness
v_s	m/s	Superficial fluid velocity (Filter velocity, Darcy velocity)
p	Pa	Pressure
η	$Pa \cdot s$	Dynamic viscosity
\mathbf{k}	m^2	Permeability tensor
k_1, k_2	m^2	In-plane permeabilities in principal directions
α	—	Anisotropy factor
ϑ	$^\circ$	Angular orientation of the principal permeability direction
v_p	m/s	Pore velocity (Mean interstitial fluid velocity)
Δp_c	Pa	Capillary pressure
r_c	m	Capillary radius
g	m/s^2	Gravitational constant

ρ	kg/m^3	Fluid density
u	m/s	Capillary driven ascend velocity of the fluid
v_w	m/s	Peripheral fluid velocity through the porous tube wall
Ca	–	Capillary number
Ca^*	–	Modified capillary number
L_c	m	Characteristic mesoscopic length
$R_{px/l}$	px/m	Image pixel to length ratio
h	m	Capillary rise / Flow front height
t	s	Time
P	m/s	Fluid penetrativity
\dot{V}_m	m^3/s	Matrix/resin volume flow rate
\dot{m}_m	kg/s	Matrix/resin mass flow rate
ρ_m	kg/m^3	Matrix/resin density
V_c	m^3	Volume of the composite specimen
V_v	m^3	Void volume (Unfilled volume in final composite)
V_f	m^3	Fiber volume
V_m	m^3	Matrix volume
A_{spec}	m^2	Areal dimensions of the composite specimen
ε_m	%	Void content referred to the matrix volume

1 Introduction and Motivation

Fiber reinforced plastics (FRP) experienced growing interest over the past decades, due to their specific properties and outstanding performance in terms of an excellent lightweight potential, high stiffness and strength, high fatigue resistance and a high degree of freedom of design. The main market sectors demanding for FRP composite solutions are the automotive industry, the aerospace industry, the wind energy sector and the industrial machinery and equipment industry [1]. The market figures show that glass fiber reinforced plastics (GFRP) account by far for the largest portion with a quantity share of over 95%. The GFRP production volume in Europe was estimated at 1 141 kt for 2018. In comparison, the global production volume of carbon fiber reinforced plastics (CFRP) 2018 was just 128 kt, but is experiencing a higher average annual growth of approximately 10% since 2013 (GFRP: ca. 2%). [2]

Besides the most common man-made fiber types (glass, carbon, basalt, aramid) natural fibers are receiving growing interest, representing a renewable alternative for product and material developments which are affected by an increasing ecological awareness. The actual production volume of natural fiber reinforced plastics (NFRP) in Europe is around 100 kt based on data for 2012 and the prognosis for the following years, whereby the automotive industry contributes with an overwhelming portion to the industrial manufacturing of NFRP parts [3]. The bioeconomy strategies for Austria indicate the importance of traditional plant fibers like hemp and flax which include their promotion and expansion of their cultivation. The measures in this context are subordinated to the main goals: the achievement of climate targets and the reduction of dependencies on non-renewable resources [4]. Similar objectives are addressed within the actual bioeconomic strategy of Germany which promotes the development and market entry for biobased, sustainable products [5], [6].

Natural fibers provide various benefits used as reinforcement constituent in the composite dependent on the given requirements. In this context Table 1 shows the relevant advantages, but also depicts the challenges related to the characteristic of natural fibers. Extensive studies over the past years focused on the drawbacks of the fiber characteristics to overcome present limitations and make them more

attractive for further applications. These investigations and developments cover issues related to (i) fiber treatments to improve specific characteristics, (ii) quality assurances during harvesting, extraction, and preparation to achieve consistent fiber properties and (iii) characterizations of the fiber reinforcements to derive optimal process conditions during the composite manufacturing. As a result of these efforts, NFRPs provide the potential to replace traditional man-made fibers while offering ecologically benefits due to their renewable nature. But to enhance the acceptance in further market segments and make them accessible for more application it is still necessary to overcome problems associated with the manufacturing techniques of natural fiber-based composites [7]. An enhanced expansion of NFRP applications into sectors like the furniture and consumer goods industry is seen as a potential development with strong market growth [2].

Table 1: Advantages and drawbacks of natural fibers in FRPs [8]–[11]

Pros	Cons
<ul style="list-style-type: none"> • Renewable resource • Low density • High specific stiffness • Thermal insulation • Acoustic and vibration damping • Non-harmful, low hazard processing • Non-abrasive properties / No tool wear • Cost-effective raw material • Low energy consumption during production • Low carbon footprint due to CO₂ conversion during growth • Residue-free thermal utilization at the end of the product life cycle • No sharp edges or fragments in case of fracture / crash 	<ul style="list-style-type: none"> • Variances in quality / properties • Moisture absorption • Lower strength compared to synthetic fiber composites • Risk of poor fiber-matrix interface • Limited temperature resistance due to degradation effects • Flammability • Low resistance against environmental influences (UV, microbial, fungus) • Price fluctuations due to varying harvest yields and concurrent market demands (e.g. clothing industry)

1.1 The use of natural fibers for fiber reinforced plastic products

As mentioned before the automotive industry is a key driver for the usage and integration of NFRP components in an industrial scale. In this context the compression molding process is the predominant manufacturing technique. The natural fiber reinforcement material, generally a plant-fiber non-woven mat in combination with a thermoplastic or thermoset polymer system, is formed under heat and pressure into its intended part geometry. Exemplary components are side and back door panels, headliner and instrumental panels, seat backs and noise insulation panels, which are typically non-structural interior parts [8], [12]. A similar field of application was targeted in an own research project 'Reliable and Sustainable composite production for Biobased Components' (RSBC) in which a wheel loader tailgate was chosen as a representative project demonstrator for various body panels of construction machinery and commercial vehicles. The corresponding component is depicted in Figure 1.



Figure 1: Wheel loader tailgate made of flax fiber reinforced epoxy resin in the frame of the FFG project 'Reliable and Sustainable composite production for Biobased Components' (RSBC)

The processing of this part was done using liquid composite molding (LCM) techniques, whereby new developed bio-based resin systems were considered to increase the amount of renewable materials in the resulting product. The objective was to provide ecologically friendly composites and manufacturing solutions to enable the production of such semi-structural components.

Further examples of NFRP in products considering a use case with little or no structural role are sporting and leisure goods (skis, snow- and surfboards, archery

bows, tennis rackets, boat hulls), instruments (guitars, violines) or furniture and consumer goods (suitcases, trays, safety helmets, chairs) [12]–[14].

Despite of the growing interest in NFRPs for low loaded applications, the enabling of these composites for structural parts has been subjected within scientific frameworks but is not widespread on the market yet. In this context the usage of hemp fibers as reinforcing constituent in the composite for a small wind turbine blade was investigated in the frame of the research project with own participation ‘Green Composites for Green Technologies’ (Green2Green). The corresponding component, which was manufactured via vacuum assisted resin infusion (VARI), is depicted in Figure 2. The comparison between the original glass fiber reinforced blade and the NFRP version showed its excellent mechanical potential for the bio-based product, at least for the considered static load case. Similar results were reported in the case study on a flax fiber reinforced composite wind rotor blade published by Shah *et al* [12].

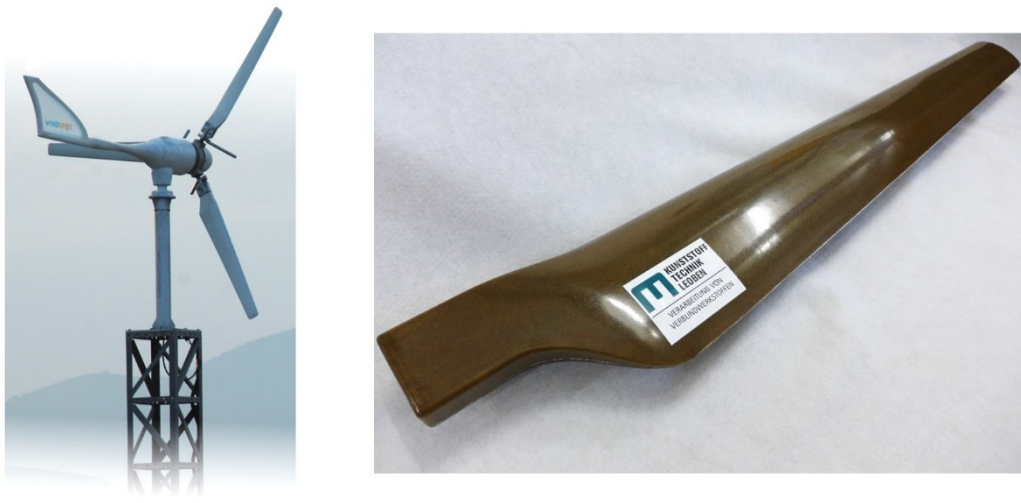


Figure 2: Rotor blade for a small wind turbine made of hemp fiber reinforced epoxy resin in the frame of the FFG project ‘Green Composites for Green Technologies’ (Green2Green)

Further recent developments in context to NFRP components with structural requirements have been made for exterior car parts, for example within the ‘Bioconcept-Car’ project series [15]. The related objective is the development of body parts and car components based on biopolymers and NFRPs. The project work of the consortium including the automobile manufacturer Porsche AG, Four

Motors GmbH and Fraunhofer WKI enabled the implementation of first small serial productions. The car doors and the rear spoiler for the 718 Cayman GT4 Clubsport are manufactured out of NFRP using flax and hemp fibers as reinforcement since its launch 2019. The production of the natural fiber reinforced components is done via resin transfer molding processes (RTM) [16]. This manufacturing technique allows the production of composite parts with good and reproducible quality and enables medium to high quantities due to a high level of automation and moderate process times [3].

The long term development of the RTM process for the production of FRP products shows a growth of the production volume of over 300% over the past 20 years [2]. Therefore, it is likely that LCM processes like RTM will get closer attention for the manufacturing of durable NFRP products in the future, besides the already established compression and injection molding techniques. The following section gives an overview of LCM processes and their characteristics with a focus on the RTM production method.

1.2 Liquid composite molding processes

LCM processes comprise all composite manufacturing approaches in which the matrix constituent is processed in an initial liquid or viscous state to impregnate the dry fiber reinforcement. The impregnation is usually achieved by an applied pressure gradient which acts as the driving force for the fluid flow. The main objective is to reach a full impregnation of the pore spaces inside the reinforcing structure to provide an optimal interconnection between the fiber and the matrix constituent without any voids and flaws.

A possibility to subdivide the LCM processing approach considers the type of driving pressure for the fluid flow through the textile fabrics. Either a vacuum pressure on the resin outlet side, an injection pressure at the resin inlet side or a combination of both pressure types can be utilized to force the liquid matrix system into the reinforcing material. In the first case the vacuum assisted resin infusion (VARI) allows the usage of just a single side mold cavity with a sealed flexible membrane as the counterpart, since the atmospheric pressure leads to a compacted state of

the materials inside the cavity. For injection processes like resin transfer molding (RTM) the pressure level is higher than the ambient pressure and requires a solid tooling approach with two or more matching mold parts, but therefore allows a higher compaction degree and fiber content for the resulting composite part. Continuous processes like winding or pultrusion processes, in which fiber bundles are impregnated inside an open resin bath or injection box, constitute a further group of LCM processes.

Since the RTM process is of particular interest in the present work the process cycle is explained in the following. The corresponding process steps are schematically depicted in Figure 3.

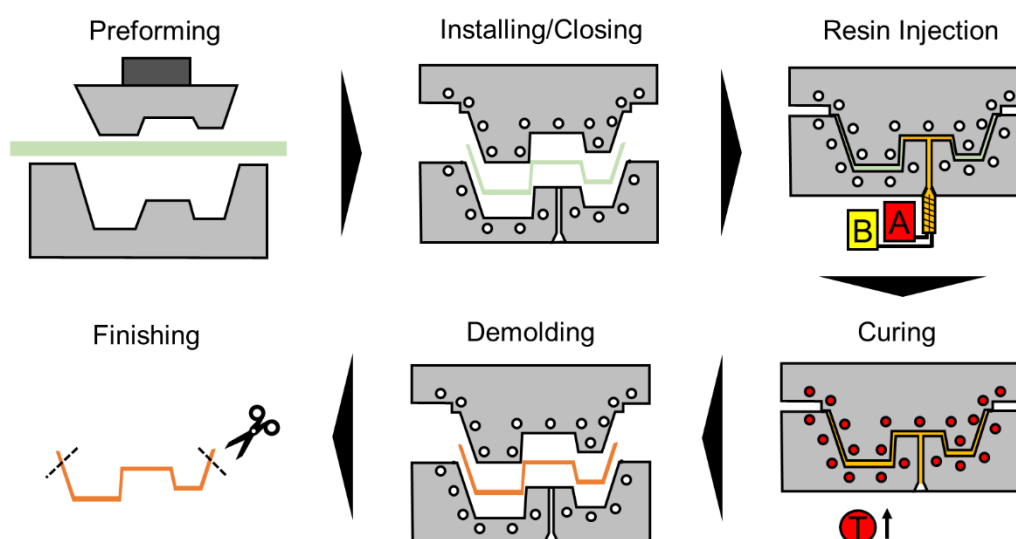


Figure 3: Resin Transfer molding process steps (Adapted from [17])

The RTM process starts with the preparation of the dry textile reinforcement, to manufacture the so-called preform. This step considers the cutting and assembly of the intended semi-finished textile reinforcements, the forming or draping to a near-net-shape geometry and the fixation of the dry fabric structure by using polymeric binder materials or auxiliary stitching threads. During the subsequent processing, the preform, which may consist of several parts, is positioned and compacted inside the RTM mold cavity. In this compacted state a liquid or viscous polymer system, generally a reactive thermoset resin system, is injected into the mold cavity to impregnate the preform and to fill the free spaces inside the cavity. Due to the cross-linking of the matrix constituents the resin system solidifies, which is referred to as

cure reaction. The impregnations step and the subsequent cure processes often takes place at elevated temperatures, dependent on the viscosity and reaction characteristics of the thermoset system. After the solidification reaches an appropriate state, the cured composite part is demolded. Subsequent finishing process steps like trimming and surface coating are applied to complete the production cycle.

Due to the complex characteristics of the fiber and matrix constituents and their interactions, the composite manufacturing is confronted by several types of defects that can occur in case of inappropriate process conditions and present uncertainties [18]. These can be subdivided into preform defects (fiber damage, misalignment, undulation), flow-induced defects (dry spots, voids, fiber washout) and cure-induced defects (microcracks, under- or overcuring, internal stresses) [19].

Regarding the impregnation-induced defects, dry spots, fiber washout or a general poor impregnation often result from conceptual process design flaws, like unsuitable injection strategies, a too low compaction state or too high injection pressures or an inappropriate fiber-matrix combination. Voids on the other hand also appear within a properly designed LCM process due to the complex saturation effects inside the porous reinforcements during the impregnation. The detrimental effects of voids on mechanical properties like interlaminar shear strength, tensile and flexural strength and stiffness, fatigue and impact resistance, was confirmed by numerous studies regardless of the utilized FRP composite type [19], [20]. Therefore, the scope of the present work focusses on the void formation in natural fiber textiles to improve the impregnation process, thus the resulting composite quality. The contents and objectives are presented in the following.

1.3 Scope and Objectives of this work

Having regard to the RTM process described before, the scope of this work focusses on the investigation of the impregnation process of plant fiber textile reinforcements. The overarching objective is the development and verification of a methodical approach for the characterization of the fibrous reinforcement and the derivation of optimized settings for the impregnation process. The principles for this optimization are based on an appropriate balance of viscous and capillary forces during the textile saturation. The intention is the reduction of flow-induced voids to a minimum due to their detrimental impact on the mechanical performance of the composite.

The hypothesis in this context is that the impregnation velocity in LCM processes has a relevant impact on the formation of flow-induced voids inside the resulting NFRP material. Therefore, the method-based textile characterization and subsequent optimization of the saturation conditions offer the possibility to improve the composite quality and its structural reliability. The novelty value of this work is the dedicated analysis on flax fiber textiles since previous research work put the focus mainly on synthetical fiber reinforcements like glass and carbon fiber types. This is being supported by the development and construction of a new test stand for the investigation of the capillary imbibition of fluids inside compacted textile structures. However, the findings obtained on new methodical approaches and underlying models in this work may also be utilized for different fiber types and are not limited to natural fibers in general.

The thematic areas of the present work are structured as follows:

In the following **chapter 2**, the underlying models for the experimental characterization are presented. This includes the model approach for the permeability characterization of porous media based on Darcy's law. Furthermore, the theoretical principles of the dynamic fluid flow due to capillary action are subjected. Based on the Lucas-Washburn (L-W) equation an adjusted model is derived which considers a peripheral fluid flow behind the main fluid flow front during the saturation process by including a permeable capillary tube wall in the model approach. This adjustment was considered due to the experimental observations

and deviations from the classical L-W model. Furthermore, the principles for fluid-induced void formation are illustrated and an approach for the optimal impregnation velocity is presented based on the characteristic capillary number.

In **chapter 3** the relevant composite materials are presented, including the properties of the flax fiber textiles and the epoxy resin system considered in this work, respectively.

Chapter 4 covers the experimental in-plane permeability characterization of the flax fiber reinforcements. Experimental test series were done on an RTM test mold with radially arranged capacitive line sensors which allow the tracking of the fluid flow during saturation. The resulting permeability characteristics and model equations are derived and discussed.

Chapter 5 presents the investigation on the capillary action inside the textile reinforcements. Based on a specially developed test stand to analyze the dynamic capillary flow, experimental test series on the considered reinforcements were conducted. The intended objective is an accurate description of the capillary driven fluid progression considering the derived model approach. Subsequently, the utilization of the results for calculating the optimal impregnation velocity is discussed, using an approach based on the capillary number which intends to define a suitable balance between viscous and capillary forces.

The validation of the optimization approach for the impregnation process is covered in **chapter 6**. Based on an RTM test series with varying impregnation settings the void contents were determined and the correlation between the fluid velocity and the composite properties are discussed.

2 State of the art and Theoretical principles

This chapter presents the state of the art related to the research contents of this work. After an introduction of the specifications of plant-based fibers and reinforcing textiles, the model approaches related to the LCM processes are shown, considering the impregnation of the porous fabrics with a liquid polymer system. This includes the material-specific permeability characteristics which define the fluid flow inside a porous medium, as well as the dynamic fluid imbibition due to capillary forces inside the pore spaces. The final sections show the relevant characteristics of typical resin systems that are used for the composite manufacturing via LCM processes, as well as the underlying mechanisms for flow-induced void formation.

2.1 Properties of natural (plant-based) fiber reinforcements

The material group of natural fibers can be divided in organic and inorganic compounds. Organic fibers are from animal origin (e.g. wool, silk) or plants-based (e.g. cotton, flax, hemp, jute, sisal, ramie) while natural mineral fibers (e.g. asbestos, basalt) rank among the inorganic group. The most important renewable representatives, regarding their usage as reinforcing component in composite materials, are cellulose-based plant fibers. Cellulose is the main constituent in plants and the most recurrent natural, organic polymer which provides high specific strength and stiffness properties.

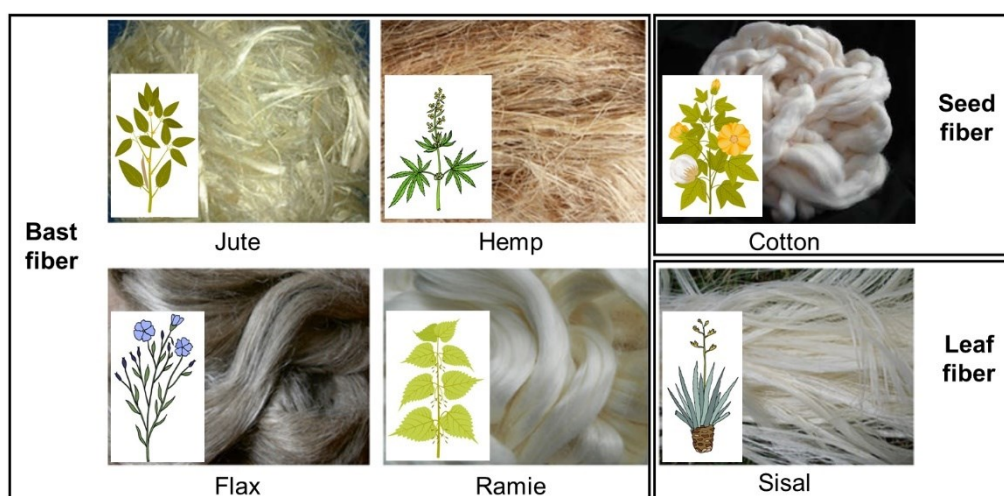


Figure 4: Selection of different plant fibers used for fiber reinforced plastic composites (Adapted from [7])

Plant-based fibers can be extracted typically from the bast, leaves or seeds [21]. Figure 4 depicts a selection of relevant plant fibers which are used as reinforcing constituents. The naturally grown fibers have a strictly hierarchical structure, which can be seen from Figure 5 exemplarily for the flax plant. The fibers which are extracted from the bast of the plant stems consists of multiple cell walls which in turn are composed of fibril strands. These fibril bundles can be broken down to the elementary fibril, which consist of crystalline structures of cellulose macromolecules. As can be seen from Figure 5 b) the fibril strands are arranged helically in the secondary cell walls with plant-specific characteristic twist angles. These angular shifts with respect to the fiber axis influences the resulting mechanical properties of the fiber [22], [23], which leads to the fact that certain fiber types provide better tension and stiffness characteristics than others, thus offer a higher performance as a reinforcement constituent in FRPs.

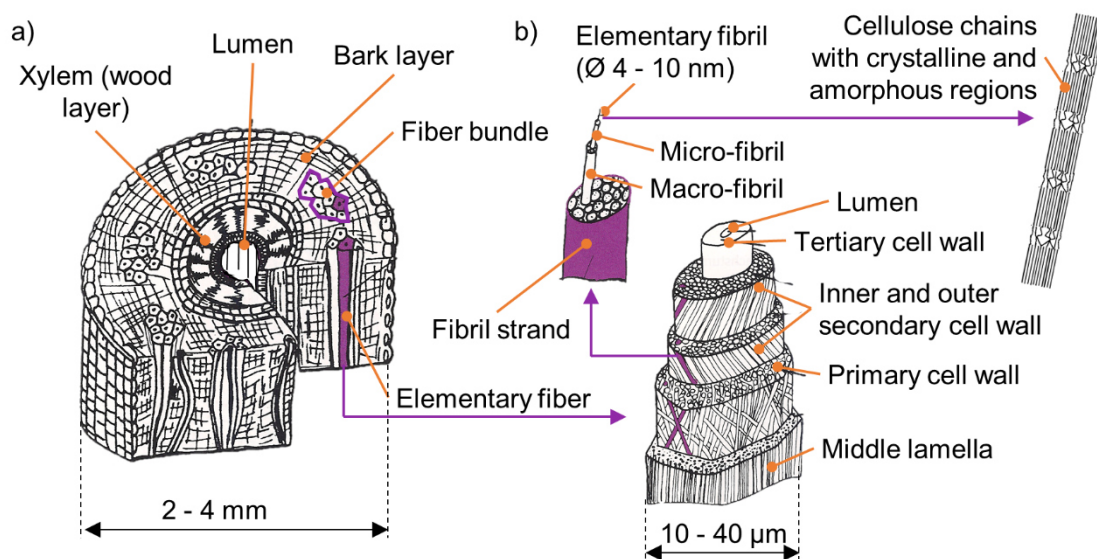


Figure 5: Hierarchical structure of the flax fiber: a) Cross section of the stem; b) Elementary fiber cross section model (Adapted from [24])

Another relevant factor is the chemical composition of the fiber which consists mainly of cellulose and additional components like lignin (the natural binder between the fibers), hemicellulose and pectin (both further polysaccharides besides cellulose), fats, waxes and moisture. In Table 2 the compositions for the selected fiber types are listed.

Table 2: Chemical composition of selected plant-based fibers [25]

Fiber	Cellulose [wt.-%]	Lignin [wt.-%]	Hemicellulose [wt.-%]	Pectin [wt.-%]	Fats & Waxes [wt.-%]	Moisture [wt.-%]
Flax	71	2.2	18.6-20.6	2.3	1.7	10.0
Hemp	70.2-74.4	3.5-5.7	17.9-22.4	0.9	0.8	10.8
Jute	61-71.5	12-13	13.6-20.4	0.2	0.5	12.6
Ramie	68.6-76.2	0.6-0.7	13.1-16.7	1.9	0.3	8.0
Sisal	67-78	8.1-11.0	10.0-14.2	10.0	2.0	11.0
Cotton	82.7	-	5.7	-	0.7	8.0

The chemical composition does not just affect the mechanical performance of the fiber but is also responsible for the surface properties in terms of their wettability with other fluids, which is of particular importance for the impregnation with liquid polymer systems. Several studies investigated the surface tension characteristics on flax fibers depending on their extraction method and further fiber treatments to specifically remove low surface energy constituents like fats and waxes [26]–[28].

A drawback related to plant fibers as reinforcing constituent is their hydrophilic nature due to hydroxyl groups of the cellulose. The moisture content may not just lead to unintended reactions with the matrix system, but also weakens the fiber-matrix interface and acts as a debonding agent. Further detrimental effects are related to the evaporation of water due to high temperatures and/or vacuum pressures during the processing which can cause voids inside the matrix. A preparatory fiber drying before further processing is therefore obligatory in most cases. Due to the intrinsic hygroscopicity, it is also important to know the behavior of the composites during their use in case of exposures to humid environments or in contact with water. Generally a rising moisture content lowers the mechanical properties which has to be considered in this context. [29], [30]

Table 3 shows the physical properties density, tensile strength, tensile modulus, and elongation at break of different fiber types based on various characterization results from literature and reviews. It is noticeable that the overall variance of the properties is significantly higher for the natural fibers compared to man-made reinforcing fibers

like glass, aramid, or carbon. While the properties of synthetic fibers can be adjusted very precisely and within tight tolerances, the ones of naturally grown fibers scatter due to variations of the used plant variety, growth condition, extraction method, test method and conditions, etc. The resulting challenges related to the assurance of consistent and reproducible properties is one of the major drawbacks for the increased usage of natural fibers in composites. This situation asks for suitable approaches like a reliable quality control and material grading systems [31]. In this context blending of various fiber batches resulted in an increase of consistency, thus supports the objective of reliable material data for the end-user [32].

Table 3: Physical properties of selected fiber types (mechanical properties: [7], [25], [30], [33]–[36], fiber length and diameter: [33], [35])

Fiber type	Density [g/cm ³]	Tensile strength [MPa]	Young's modulus [GPa]	Elongation at break [%]	Fiber length [mm]	Fiber diameter [μm]
<u>Plant-based:</u>						
Flax	1.38-1.50	343-1500	27.6-80	1.2-3.2	10-65	5-38
Hemp	1.35-1.48	550-1110	26-80	1.2-3	5-55	10-51
Jute	1.23-1.46	187-800	10-30	1.16-3.1	0.8-6	5-25
Ramie	1.44-1.50	400-938	44-128	1.2-4	40-250	18-80
Sisal	1.20-1.45	468-855	9.4-38	1.2-3.8	0.8-8	7-47
Cotton	1.21-1.6	287-800	5.5-12.6	2-10	12-35	12-35
<u>Man-made:</u>						
E-glass	2.5-2.6	2000-3500	70-73	3-4.5	∞	3-25
Aramid	1.4-1.5	3000-3600	83-186	2.0-4.0	∞	12
Carbon (HT)	1.8	3600-4000	230-240	1.4-1.8	∞	7

A further difference between natural and man-made fibers is the present fiber length. While the synthetic ones can be produced continuously, the length of the natural elementary fiber is within a characteristic range depending on the plant type. This specification affects the manufacturing of semi-finished products (reinforcing textiles and fabrics), which are used to design and manufacture the composite part. An overview of common types of reinforcements is given in the following section.

2.1.1 Fiber reinforcements and Textile architectures

Fiber reinforcements are generally used in form of semi-finished products. Their production base in most cases on common textile processing methods applied for the manufacturing of non-wovens, wovens, braids and knits, or are fixed by stitching. In Figure 6 two variations of possible processing routes are depicted which differs by the preparatory processing step of the fibers. The production of non-woven fabrics uses carded fibers, which are laid down and fixed to obtain an interconnection of the fibers and a stability of the fabric. The alternative route uses yarns which are processed to form a stabilizing intersection pattern of two or more thread systems (woven fabrics, braids) or which are fixed by a sewing thread (non-crimp fabric). A non-crimp fabric (NCF) typically consists of two (biaxial) to four (quadraxial) layers of parallel yarns with defined orientations. The unidirectional woven fabric follows the same principle of parallel aligned yarns in the textile plane by using a very thin weft thread instead of a stitched thread to stabilize the textile. To provide the best performance in terms of material stiffness, the reinforcing fiber orientation in the composite structure should be aligned with the load direction. Therefore, fabrics with defined fiber orientation provides better possibilities to design a load-optimized composite part than a random fiber mat.

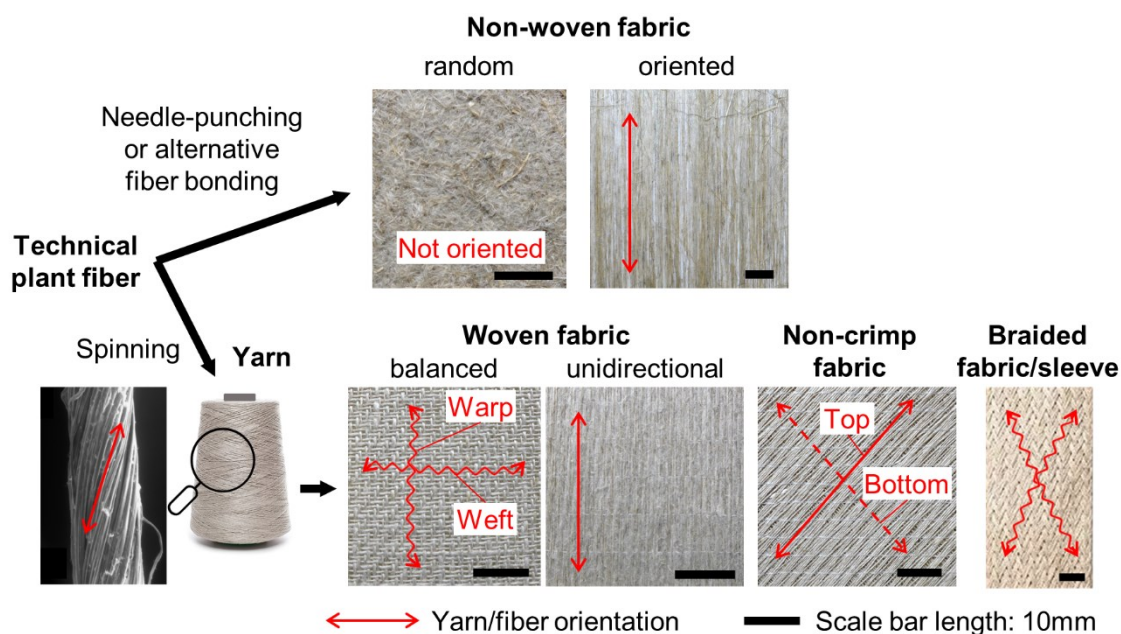


Figure 6: Different types of textile flax fiber reinforcements used as semifinished products for composites

In Figure 6 the orientations of the fibers and yarns are marked by red arrows which indicate occurring divergences between the load and the fiber direction inside the intended composite part. One effect comes from the fiber twist in the yarn which leads to a deviation of the fiber orientation from the yarn axis, thus a reduction of the mechanical potential of the reinforcement. Another factor is the undulation of the yarn in case of woven or braided fabrics which causes a deflection of the fiber orientation from the textile plane. Nevertheless, these fabric types belong to the most used reinforcements due to the established and adjustable manufacturing techniques and their easy handling. New developments on the architecture of flax fiber reinforcements from textile manufactures like Bcomp Ltd. (Switzerland), Lineo SAS (France) and EcoTechnilin SAS (France) increase their potential by using low-twist or no-twist yarns or by enabling the production of non-woven fiber tapes with unidirectional fiber orientation [13], [37]. Depending on the design and architecture of the fiber reinforcement, bast-fibers like hemp and flax show the potential to compete with classical engineering materials like glass fiber reinforced plastics and therefore are seen to be suitable for composites with comparable structural load cases [23], [38], [39].

The reinforcing fabrics considered in this work are typically two-dimensional. The three-dimensional shape of the composite part is generated by the stacking of several plies to the intended thickness and by deformation and draping of the plane laminate to the final geometry, which is defined by the LCM tooling, as shown in chapter 1.2. The most general parameter for the specification of such textile reinforcements is the fabric areal weight FAW [g/m^2]. Depending on the fabric type more specific information are provided by the weaving style, the weave density (threads per length) in case of woven fabrics or the yarn orientation angles and stitching specifications in case of NCFs. The yarn specifications are generally given by its fineness (weight per length) and optionally by further information related to its structure e.g., twist level, auxiliary fibers/constituents, or yarn thickness.

2.1.2 Surface characteristics of natural fibers

The surface characteristics of the reinforcing material generally plays an essential role for FRP composite since they define interface properties between the fiber and

the matrix phases. Regarding the impregnation with a liquid polymer system, a good bonding can only be obtained when the fiber provides a good wettability. The physical quantity for the characterization of the surface is the free surface energy γ . The interaction between a solid and a liquid in a gas or vapor phase can be described by Young's equation [40] which is defined as follows:

$$\gamma_s = \gamma_{sl} + \gamma_l \cdot \cos(\theta) \quad (1)$$

where γ_s , γ_{sl} and γ_l represent the surface energies of the solid-vapor, the solid-liquid and the liquid-vapor interface, respectively. The angle θ is the contact angle between the solid and the liquid phase at the triple point. The representation of Young's equation on a sessile drop on top of the solid surface is depicted in Figure 7. The wettability is higher the smaller the contact angle. A contact angle of 0° is related to a complete spreading of the liquid (full wetting), while contact angles above 90° indicate a poor wettability of the solid surface. Due to the low interaction the influence of the gas or vapor phase can be neglected in many cases. Young's equation show that a good wettability goes along with a high solid surface energy and a low liquid surface energy, which is also called the liquid surface tension. A substantive theory related to the characterization of the wettability of solid surfaces is the Zisman theory [41]. It considers a critical liquid surface energy which represents the minimum which is needed to reach a full wetting on the solid surface ($\theta = 0^\circ$).

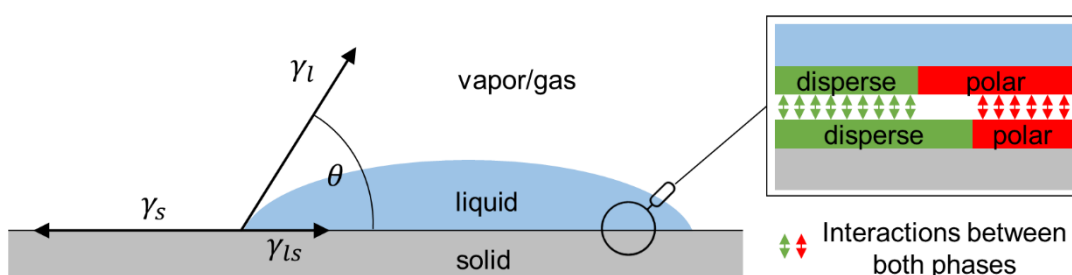


Figure 7: Surface energy components of Young's equation and a schematical representation of the interface with disperse and polar surface characteristics

Newer approaches, like the theories from Owens & Wendt [42] or Wu [43], consider the (non-)polar characteristics of the liquid and solid surfaces which affects the interface between both phases. This is done by separating the surface energy into

a disperse and polar component ($\gamma_s = \gamma_s^d + \gamma_s^p$). As it is schematically depicted in Figure 7, these approaches are capable to consider the compatibility of both phases in this context. Equal characteristics result in a high interaction which is related to a low interfacial energy between the solid and liquid, thus a better wetting potential, and vice versa.

The surface energy characterization of natural fibers commonly uses wetting techniques based on tensiometric or capillary measurements, or by alternative determination approaches e.g. based on inverse gas chromatography [44]. The measurement results on flax fibers, which is the focused fiber type in the present work, show surface energy characteristics as follows. In the studies from van Hazendonk [26] the surface energy of flax fibers resulting from different retting methods and different fiber treatments was determined based on a fiber floating approach with different test fluids. Based on Wu's harmonic mean approximation the surface energies with dispers (d) and polar (p) proportions for dew retted and warm-water retted flax fibers were 29.7 mN/m (d: 27.8 mN/m, p: 1.9 mN/m) and 34.2 mN/m (d: 31.3 mN/m, p: 2.9 mN/m), respectively. Subsequent fiber treatments which were intended to extract low energy constituents of the fiber revealed a significant effect on the measurement results. The removal of fats and waxes with ethanol and the extraction of pectins and hemicellulose with ammonium oxalate and sodium hydroxide, respectively, led to an increase of the surface tension up to 66.1 mN/m (d: 50.0 mN/m, p: 16.1 mN/m). Tensiometric measurements from Van de Velde [27] were conducted on flax fibers which were extracted from different reinforcing textiles. The surface energies are in a similar range between 33.27 mN/m (d: 32.14 mN/m, p: 1.13 mN/m) and 35.83 mN/m (d: 31.47 mN/m, p: 4.36 mN/m). These results reveal the characteristic surface energy range for flax fibers which is used for the selection of suitable test fluids in the course of the investigations on the capillary actions presented in chapter 5.

The various forms of fiber reinforcement architectures and wetting properties must be considered for the LCM processing since their properties significantly affects the process in terms of drapability, compaction and impregnation, thus defines the limits of the processing possibilities. Therefore, the specific characterization of the textiles

is necessary to develop an appropriate process design and to evaluate optimal process parameters. The following chapter covers the relevant characteristics and underlying models related to the compaction response, the permeability characteristics and the capillary effects.

2.2 Process-relevant characteristics of fibrous reinforcements

In this chapter the relevant properties of reinforcing fabrics with regard to their behavior in LCM processes are presented. This includes the preparatory compaction of the reinforcements as well as the fundamental models and theories related to the fluid flow through the porous structure during the impregnation.

2.2.1 Compaction properties

The dry fiber reinforcement structure (preform), which is generally assembled using semi-finished textile products as shown in chapter 2.1.1, is impregnated in a compacted state during the LCM manufacturing process. It is generally intended to achieve a high fiber content to get optimized mechanical properties of the resulting composite. For an accurate process and part design it is therefore necessary to know the response of the reinforcement during compaction. In case of the RTM process the final compaction of the dry preform to its intended thickness takes place inside the tool cavity. A schematic representation of this process step is depicted in Figure 8, which shows a stack of textile layers inside the closing mold cavity.

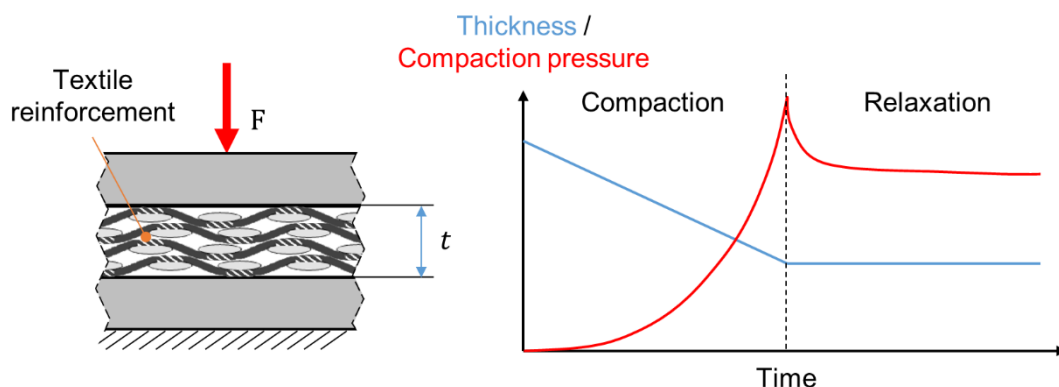


Figure 8: Schematics of the compaction on a dry textile reinforcement

The compaction pressure increases progressively with decreasing thickness. When the final position is reached the relaxation in the fibrous material leads to a time dependent stress reduction to a certain level. In this preparatory state the dry preform is subsequently impregnated with the liquid polymer system.

The characterization of the compaction state is usually done with respect to its fiber volume fraction or by the remaining porosity fraction. Considering the total volume V_{tot} , which represents the overall volume of the compacted preform with respect to its outer dimensions, as it is generally defined by the cavity dimensions, it consists of the following constituents:

$$V_{tot} = V_f + V_p (+ V_{aux}) \quad (2)$$

where V_f is the volume of the fibers, V_p the pore volume and V_{aux} the volume of auxiliary constituents like binder materials used for the preform fixation or thread yarns which are not considered as reinforcing component. The resulting fiber volume fraction φ is then:

$$\varphi = \frac{V_f}{V_{tot}} = \frac{\frac{m_f}{\rho_f}}{A_{tex} \cdot t} \quad (3)$$

where m_f is the fiber weight of the textile reinforcement, ρ_f is the fiber density, A_{tex} is the areal size of the preform and t its actual thickness. In the present work there are no auxiliary constituents considered since the stacking of several fabric plies was done without particular fixation. In this case the remaining porosity fraction ϕ depends on the fiber volume fraction φ as follows:

$$\phi = 1 - \varphi \quad (4)$$

The fiber volume fraction does not just influence the mechanical properties of the resulting composite material but also affects the processing design itself. This applies in particular the resin impregnation which strongly depends on the actual porosity state. While a too low compaction can cause a displacement of the fibrous material due to the fluid pressure during injection (fiber wash-out), an excessive compaction can lead to fiber damage which significantly reduces the composites mechanical performance [45]. Furthermore, the acting process forces and

pressures must be considered in terms of necessary clamping forces, tool stiffnesses, injection pressures and available impregnation times, which are limited by the cure reaction of the thermoset polymer. The compaction response strongly depends on the architecture of the reinforcement which is shown in Figure 9. The depicted progressions of the compaction curves for various fabric types reveal the differences. As can be seen from this selection, higher fiber volume fractions at a given pressure can be reached for the glass fiber woven fabric and for the unidirectional flax fiber textile which allow a denser arrangement of the fibers compared to the natural fiber woven and nonwoven fabrics, respectively.

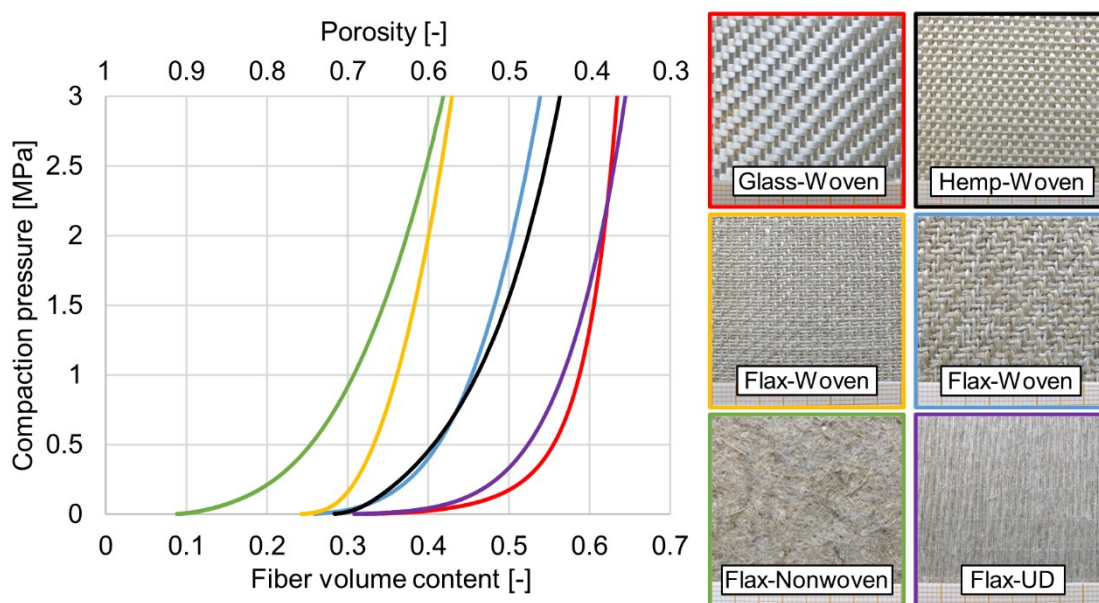


Figure 9: Compaction response of different reinforcing fabrics (Adapted from [46])

Therefore, the analysis of the acting mechanisms inside the fibrous structure and the resulting compaction response is of particular interest for a predictable process design and was subject in numerous studies. One approach is the analytical description of these effects, specified in consideration of underlying material models, the present geometry of the fibers and yarns and mechanical theories. The early studies from van Wyk [47] and further publications e.g. from Beil and Roberts [48], [49] and Chen *et al* [50]–[52] are noteworthy in this context. For typical textile architectures the analytical description of the compaction response is complex due to the presence of several influencing and interacting mechanisms like yarn deformation and flattening, yarn bending, condensation of the porous spaces, nesting effects between the textile layers and deformation/collapse of the fibers,

which summarizes the main factors according to the studies from Chen [52] and Shah [53].

The alternative approach for the description of the compaction behavior based on empirical models. Due to the complexity of the acting mechanisms this is often seen as the more expedient approach for an efficient modelling of the compaction response for complex architectures and varying fiber properties [39], [54]. Investigations on plant fiber reinforcements were conducted from Shah [53], Madsen [39] and Francucci [54]–[56]. In context with the present work an empirical model equation was developed which is capable to describe various types of natural fiber fabrics and test configurations with high accuracy [46].

2.2.2 Permeability characteristics

LCM processes have in common that a fiber reinforcement in an initial dry state is impregnated by a liquid polymer system. This process step is related with the fluid flow inside a porous material, where the air in the pore spaces is replaced by the matrix component. In this context, the permeability is a measure for the resistance against flow through the porous medium, which is a material-specific parameter depending on the properties of the reinforcement. The smaller the permeability, the higher the resistance against the fluid motion. The related characteristics are of particular importance for manufacturing techniques which require longer flow distances of the resin system inside the preform structure. This is typically the case in RTM or VARI processes, as presented in chapter 1.2. In terms of process reliability, including the preparatory process design phase and parameter settings, as well as an efficient design of the LCM tooling without time- and cost-intensive reworking, the preliminary computation of the fluid flow during the impregnation is of particular interest for industrial applications. Therefore, an accurate determination of the permeability characteristics for fiber reinforcements becomes relevant. The challenges related to this task based on the complexity of the porous fiber reinforcements, which are manifold due to the diversity of different fabric types, and the sensitive dependencies on the actual conditions like compaction state, dual or multi-scale pore sizes, orientation, shear, distortion, etc. Analytical models which describe the relationship between the permeability and the geometrical features

cannot offer the required accuracies for the present variety. Therefore, the most reliable way to determine the permeability properties of the reinforcements is still the empirical approach based on fluid flow experiments. [57]

For the intended applications in this work the two governing equations to describe the flow of a fluid inside a porous material are the continuity equation for incompressible fluids:

$$\nabla \cdot \mathbf{v} = 0 \quad (5)$$

and Darcy's law [58]:

$$\mathbf{v}_s = -\frac{\mathbf{k}}{\eta} \nabla p \quad (6)$$

Darcy's equation shows the relationship between the superficial fluid velocity \mathbf{v}_s , the pressure gradient ∇p , the dynamic fluid viscosity η , and the permeability characteristics of the porous material, expressed by the second order permeability tensor \mathbf{k} . This relationship was determined empirically by Henry Darcy in 1858. Whitaker verified analytically Darcy's law, which can be derived based on an volume averaged version of the Navier-Stokes equation [59]. The assumptions and conditions for this fluid flow model are as follows: [60]

- Steady state flow conditions
- Inertia effects are negligible
- The fluid is incompressible
- The fluid is Newtonian
- The fluid viscosity is constant
- Gravitational forces are negligible

The general permeability in three spatial dimensions is described by the permeability tensor \mathbf{k} with its nine components as follows:

$$\mathbf{k} = \begin{bmatrix} k_{xx} & k_{xy} & k_{xz} \\ k_{yx} & k_{yy} & k_{yz} \\ k_{zx} & k_{zy} & k_{zz} \end{bmatrix} \quad (7)$$

Based on this general form referred to an arbitrary coordinate system $[x, y, z]$, the assumption of an orthotropic characteristic for the textile reinforcements allows the

transformation of \mathbf{k} into the related principal coordinate system [1,2,3], which results in:

$$\mathbf{k} = \begin{bmatrix} k_1 & 0 & 0 \\ 0 & k_2 & 0 \\ 0 & 0 & k_3 \end{bmatrix} \quad (8)$$

In context with the permeability definition of the regarded porous materials, k_1 and k_2 usually represent the permeabilities along the major and the minor axis in the plane of the textile reinforcement (in-plane permeability) and k_3 represents the permeability perpendicular to the plane (through-thickness permeability). This approach based on the assumption that the perpendicular out-of-plane axis is one of the principal directions, which is given in case of common reinforcing fabrics regarding the geometric point symmetry of the preform structure (generally a stack of several textile layers) along the through-thickness direction. In Figure 10 an exemplary fluid propagation inside a porous material based on Darcy's law and the given assumptions is depicted. The pressure driven fluid is injected from the central inlet point and propagates with a half-ellipsoid shape which is defined by its extensions in the principal directions 1,2 and 3.

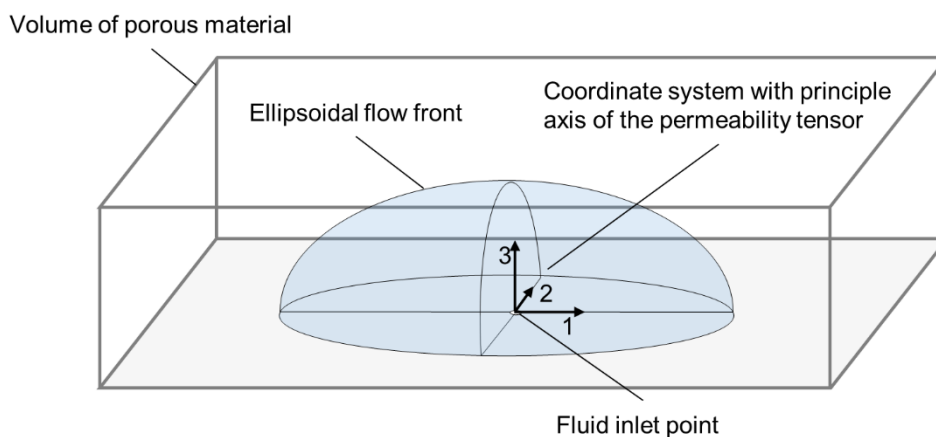


Figure 10: Schematic of the 3-dimensional fluid flow inside a porous material with orthotropic permeability characteristics

In-plane permeability characterization

From the experimental point of view the measurement of the three-dimensional fluid propagation is difficult to realize. Therefore, empirical approaches usually focus on the measurement of the in-plane permeability characteristics or the evaluation in the

through-thickness direction separately. The selection of necessary measurements for a sufficient material characterization depends on the flow situation in the process. In cases where the fluid flows within the textile plane, as it is present in many RTM processes and particularly for thin-walled composite parts, the through-thickness permeability is of minor interest [17]. In the present work the focus is on the determination of the in-plane permeability characteristics of the considered flax fiber reinforcements. In Figure 11 the schematic of a 2-dimensional in-plane permeability experiment is depicted. The tested porous material is prepared with a central hole aligned with the fluid inlet point which let the fluid spread quickly and without any resistance along the thickness to create a uniform flow within the plane. The central cut out additionally defines the initial boundary conditions for the fluid flow which propagates inside the material from the inside out.

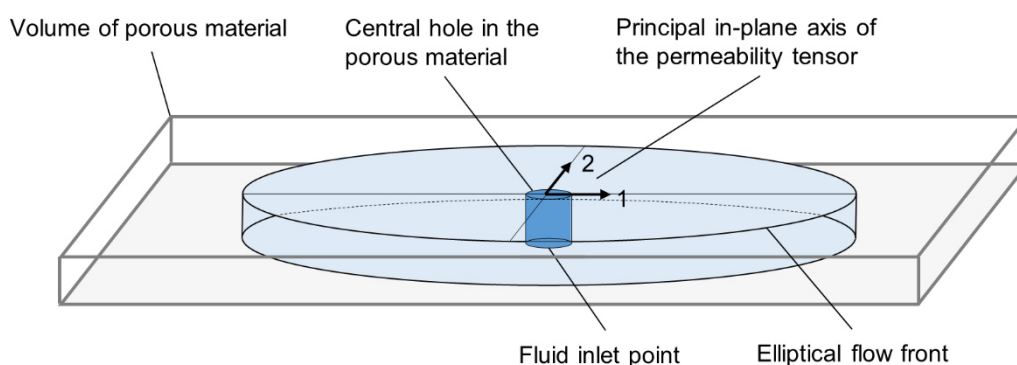


Figure 11: Schematic of the 2-dimensional (in-plane) permeability characterization

The transfer of the general description of the in-plane permeability and the properties of a typical reinforcing fabric can be seen in Figure 12. The schematic shows the plane of the textile reinforcement with the flow propagation that corresponds to the in-plane permeability measurement. A reference direction in the plane is generally defined by the machine or production direction of the fabric which corresponds to an orientation angle of 0° . Due to the orthotropic nature the flow front shape is usually in good approximation elliptical. The major and minor axis define the principal directions 1 and 2, which correlate with the permeability values k_1 and k_2 , respectively. The orientation of the principal coordinate system, which is defined by the angle ϑ , as depicted in Figure 12, is needed for a complete characterization

of the in-plane permeability. An exception is the special case of a real isotropic behavior in the plane which correlates with a circular flow front shape ($k_1 = k_2$).

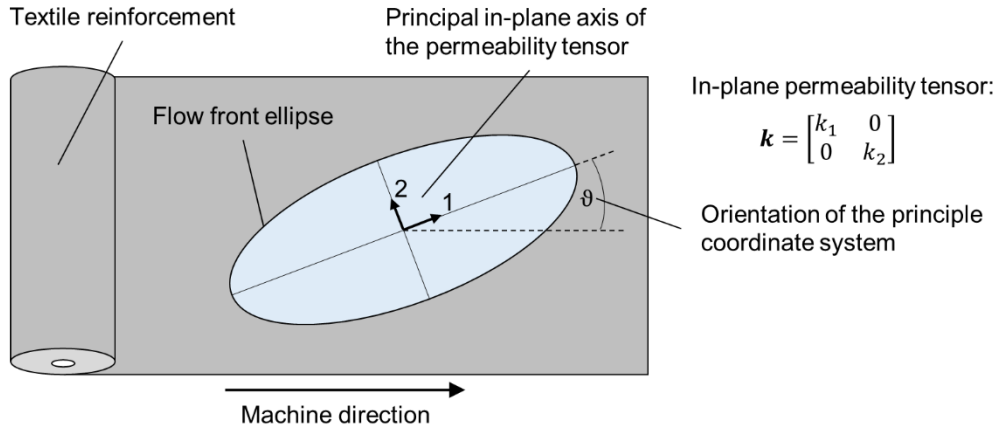


Figure 12: In-plane permeability characteristics of a textile reinforcement

A parameter to describe the directional differences of the in-plane permeability is the anisotropy factor which is defined as follows:

$$\alpha = \frac{k_2}{k_1} \quad (9)$$

The anisotropy factor α is within the range between 0 and 1, since the k_1 permeability is by definition larger than k_2 . A factor of 1 corresponds to the isotropic case ($k_1 = k_2$), while the degree of anisotropy increases with decreasing α .

The velocity vector on Darcy's law \mathbf{v}_s represents the fluid velocity in the absence of the porous media, which is called the Darcy, filter or superficial velocity [61]. Since most experimental approaches measure the flow front propagation inside the porous media during saturation, the following relationship is used to approximate the mean interstitial flow velocity \mathbf{v}_p considering the free pore volume of the porous medium [61]:

$$\mathbf{v}_p = \frac{\mathbf{v}_s}{\phi} \quad (10)$$

where the parameter ϕ is the pore content of the material. The pore velocity \mathbf{v}_p corresponds to the velocity of the moving flow front, which is generally tracked via a suitable sensor-based approach during the experiment.

Based on the measurements of the ellipse geometry over time, the porosity state and the information of the driving pressure and the fluid viscosity, the permeability values can be determined. Since there is no analytical solution for the 2-dimensional fluid flow through porous media described by Darcy's law (Eq. (6)) and the continuity equation (Eq. (5)), several approximation approaches has been developed for the evaluation of in-plane permeability experiments. The evaluation routine used in this work based on the algorithm from Adams & Rebenfeld [62], [63]. This is one of the most common approaches besides alternative solving methods for radial flow experiments, e.g. from Weizenböck *et al* [64], Chan & Hwang [65], Carter *et al* [66] or Fauster *et al* [67]. The approximation approach of Adams & Rebenfeld is based on the neglect of the pressure gradient perpendicular to the flow direction, which leads to a solvable expression of the regarded problem. It was shown that the related results are in good agreement with the values evaluated numerically [62]. For detailed information of this evaluation procedure the reader is referred to the associated publications: [62], [63], [68], [69].

The intense research and development related to the in-plane permeability characterization in terms of methodology and reliability indicates the importance of this topic for the LCM processing, which is also testified by several international in-plane permeability benchmarks and round robin studies throughout the past years [70]–[74].

One-dimensional fluid flow through porous media

Considerably easier is the description of the fluid flow in only one dimension, in the present case along the x-direction. According to Darcy's law (Eq. (6)) the relationship between the superficial fluid velocity $v_{s,x}$, the dynamic fluid viscosity η , the related permeability value k_x and the pressure gradient $\frac{dp}{dx}$ is as follows [75]:

$$v_{s,x} = -\frac{k_x}{\eta} \frac{dp}{dx} \quad (11)$$

The continuity equation for the one-dimensional, incompressible flow shows that the fluid velocity is constant over x. This results in a constant pressure gradient along the flow path since the permeability and the viscosity are considered to be constant.

Regarding the consequent pressure progression along x and the expression for the fluid flow velocity inside the porous material from Eq. (10), Eq. (11) can be written as:

$$v_{p,x} = -\frac{k_x}{\phi \cdot \eta} \frac{\Delta p}{\Delta x} \quad (12)$$

where Δp is the related pressure difference over a flow length Δx . A schematic representation of the flow situation is depicted in Figure 13 which shows the pressure progression over x for the displayed moment. The pressure level at the flow front and in the unsaturated area is set to zero, which is typically the atmospheric pressure since there is no additional pressure applied at the venting side. For the analysis of the one-dimensional flow two approaches are commonly used:

1. The fluid flow with constant pressure drop between inlet and outlet Δp which leads to a decrease of the fluid velocity with increasing flow path length Δx .
2. The forced fluid flow with constant flow rate, respectively constant flow velocity, which leads to an increase of the necessary inlet pressure p_{in} with increasing flow path length Δx , according to Eq (12).

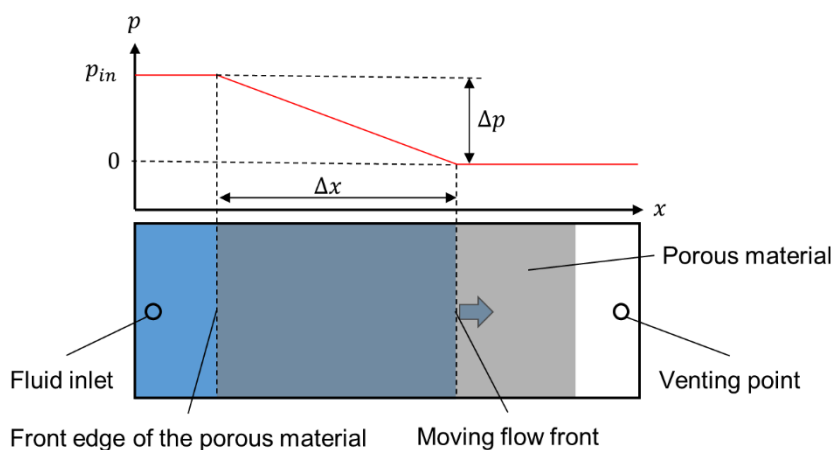


Figure 13: Schematic representation of a one-dimensional fluid flow through a porous medium

The permeability-porosity relationship

Based on the empirical permeability results, it is intended to find a suitable functional relationship which connects the measured value and the changing variable,

generally the porosity or the fiber volume content. A modified model which orients towards the Carman-Kozeny equation [61], [76], [77] revealed as a suitable approach to describe the permeability progression of various natural fiber fabrics dependent on the actual porosity state [78]–[80]. The model equation is given as:

$$k_{CKmod} = \frac{\phi^{N+1}}{C \cdot (1 - \phi)^N} \quad (13)$$

where k_{CKmod} is the modeled permeability, ϕ the porosity content and N and C two empirical regression parameters. Additionally, this equation fulfills the logical boundary conditions at $\phi = 0$ and at the upper limit $\phi \rightarrow 1$, where the permeability reaches values of zero and infinity, respectively.

An alternative model equation which has been found to be suitable to describe the empirical permeability data is the one proposed by Gauvin *et al* [81] which based on an exponential function of the following form:

$$k_{Exp}[m^2] = c_1 \cdot \exp(\phi \cdot c_2) + c_3 \quad (14)$$

In this case c_1 , c_2 and c_3 are three empirical model parameters which are determined by regression to fit the measurement results.

2.2.3 Capillary effects

The fibrous architecture of reinforcing textiles consists of interstitial pore spaces between the fibers. Depending on their size and the interaction properties between the fiber surface and the liquid polymer, the impregnation is affected by capillary forces. The models, which are used to describe the dynamic imbibition mechanisms of fluids due to capillary effects, are generally related to Washburn's model approach [82], [83]. Based on his results from 1921 and in context with the earlier works from Lucas [83] and Bell & Cameron [84], he described the dynamic flow process of fluid imbibition in porous materials by modelling the pores as a bundle of cylindrical tubes. The mathematical relationship can then be derived considering the Hagen-Poiseuille law and the Young-Laplace equation.

The Hagen-Poiseuille law

The Hagen-Poiseuille law describes the relationship between the volumetric fluid flow rate through a cylindrical tube of constant cross section and the pressure drop over the flow length considering an incompressible, Newtonian fluid and laminar flow conditions.

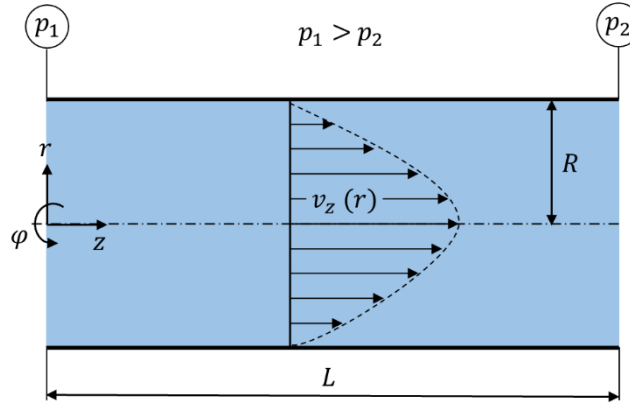


Figure 14: Schematics regarding the Hagen-Poiseuille equation

The velocity profile is depicted in Figure 14 which is characterized by a parabolic form according to the following equation:

$$v_z(r) = \frac{R^2 \Delta p}{4 \eta L} \left(1 - \frac{r^2}{R^2} \right) \quad (15)$$

where $\Delta p = p_1 - p_2$ is the driving pressure drop related to the flow inside the tube with the length L and the radius R while η is the dynamic viscosity of the fluid. The derivation of this function based on the Navier-Stokes equation and the continuity equation which is presented in appendix A.3. With the given velocity profile of Eq. (15) the volumetric flow rate \dot{V} is given as:

$$\dot{V} = \int_0^{2\pi} \int_0^R v(r) r dr d\phi = \frac{\pi R^4 \Delta p}{8 \eta L} \quad (16)$$

which is known as the Hagen-Poiseuille law. The corresponding mean velocity of the fluid in z -direction is then:

$$\bar{v}_z = \frac{\dot{V}}{A} = \frac{R^2 \Delta p}{8 \eta L} \quad (17)$$

The comparison of Eq. (17) with Eq. (15) shows that the mean velocity is half the maximum velocity at the tube axis:

$$\bar{v}_z = \frac{1}{2} \cdot v_z(r = 0) \quad (18)$$

The Young-Laplace equation

The Young-Laplace equation describes the relationship between the pressure difference on a (curved) fluid interface, its shape, and the interfacial surface tension. For an arbitrary surface area, which is characterized by its principal radii of curvature r_1 and r_2 , the equation is as follows:

$$\Delta p = p_{in} - p_{out} = \gamma \left(\frac{1}{r_1} + \frac{1}{r_2} \right) \quad (19)$$

where γ is the surface tension of the A-B interface and Δp is the pressure difference between medium A at the concave side and medium B at the convex side. A schematic representation of that curved interface is shown in Figure 15.

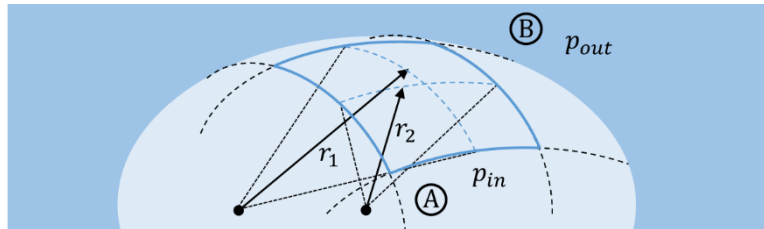


Figure 15: Schematics regarding the Young-Laplace equation

For a spherical interface with $r_1 = r_2 = r_s$, Eq (19) becomes to:

$$\Delta p = p_{in} - p_{out} = \frac{2\gamma}{r_s} \quad (20)$$

This relationship is used to derive the acting pressure in small capillaries since the meniscus can be approximated as a spherical surface in this case. Different scenarios of a fluid inside a capillary tube are depicted in Figure 16. In case of a full-wetting fluid, which is characterized by a contact angle of 0° between the fluid and the capillary wall, the radius of the approximated spherical interface r_s is equivalent

to the radius of the capillary r_c (Figure 16 a)). For contact angles above 0° the relation of the interface radius and radius of the capillary can be considered as shown in Figure 16 b) and c), respectively.

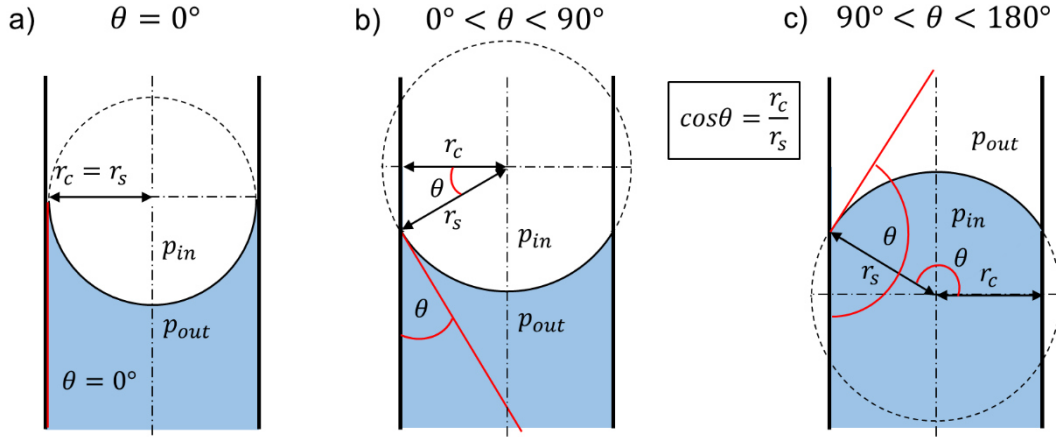


Figure 16: The Young-Laplace equation for capillary tubes

The related pressure difference in these scenarios, which is known as the capillary pressure Δp_c , depends on the capillary radius r_c and can be expressed as follows:

$$\Delta p_c = \frac{2\gamma \cos(\theta)}{r_c} \quad (21)$$

For wetting fluids ($\theta < 90^\circ$, Figure 16 a) and b)) the shape of the fluid-air interface is concave. Since the pressure p_{in} is in good approximation equivalent to the ambient pressure the pressure difference correlates with a negative pressure on the fluid side, which is the driving force for an ascending fluid flow inside the capillary. With increasing contact angles, the capillary pressure Δp_c decreases and becomes zero for $\theta = 90^\circ$, which correlates to a non-curved interface, thus no resulting pressure difference. A further increase ($\theta > 90^\circ$, Figure 16 c)) is present for non-wetting fluids. In this case the surface shape is convex with a related overpressure on the fluid side at the equilibrium state, which results in a flow downwards the capillary tube. This scenario is called capillary depression. In this work the focus is on wetting fluids since the corresponding fluid properties in contact with the fibrous reinforcement is essential with regard to a proper impregnation during the LCM processing. Therefore, it is assumed that in context of this work spontaneous imbibition of the fluid inside the capillaries takes place, thus $\theta < 90^\circ$.

Inserting the Young-Laplace relationship of Eq. (21) in Eq. (17) of the Hagen-Poiseuille law leads to the Lucas-Washburn equation, which describes the dynamics of the fluid flow inside capillary tubes. The fluid velocity can be expressed as follows:

$$\bar{v}_z = \frac{dz}{dt} = \frac{\gamma \cos(\theta) r_c}{4 \eta z} \quad (22)$$

Separation of the variables and subsequent integration lead to the following solution of this differential equation:

$$\int_{z_0}^z z dz = \int_{t_0}^t \frac{\gamma \cos(\theta) r_c}{4 \cdot \eta} dt \quad (23)$$

$$z(t)^2 - z_0^2 = \frac{\gamma \cos(\theta) r_c}{2 \eta} (t - t_0) \quad (24)$$

In case of $t_0 = 0$ s and an initial flow length of zero ($z_0 = 0$ m) the commonly used relationship between flow length and time, known as the Lucas-Washburn (L-W) equation, is given as follows:

$$z(t)^2 = \frac{\gamma \cos(\theta) r_c}{2 \eta} t \Leftrightarrow z(t) = \sqrt{\frac{\gamma \cos(\theta) r_c}{2 \eta} \cdot t^{0.5}} \quad (25)$$

This relationship is very popular due to its simplicity with only few material parameters required. It already demonstrated appropriate correlations for some use cases in context with the fluid flow inside porous media, although it is obviously an abstracted description compared to many real situations, due to the following assumptions:

- The pore geometry is a cylindrical tube without cross section changes.
- The influence of gravitational forces is neglected.
- The fluid flow is purely laminar and viscous without any inertia effects or turbulence.
- The fluid is incompressible and Newtonian.

In addition to these simplifications, Masoodi and Pillai pointed out the following discrepancies to the real wicking phenomenon inside porous media [85]:

- The model considers only a one-dimensional flow which cannot be extended to two- or three-dimensional wicking flows in complicated geometries.
- The real porous microstructure is often complex with interconnected pores which is not considered.
- A distribution of different pore sizes is not considered.
- The tortuosity of the flow path is not considered.

These missing or neglected effects led to various modifications of the L-W equation to derive a more accurate representation for the respective situation [85]. In this regard the development of a suitable relationship between the wicking rate and characteristics of the porous material is often challenging due to great variations of the present microstructure [86]. In context to the present work a closer look is taken on the influence of gravitational forces and a modified version of the L-W model is used which considers a peripheral fluid flow through the capillary tube wall. These adjustments were implemented based on the observations during capillary rise experiments and deviations from the L-W equation. The objective of this measure is to overcome the deficiencies related to the real pore morphology as listed above, while keeping the model as simple as possible.

Consideration of the gravitational force

The analysis of the influence due to gravitational forces can be relevant since common arrangements for imbibition or capillary rise tests lead to a fluid flow against gravity. In this case the rise of the fluid in height leads to a hydrostatic pressure, p_h , which can be considered in the pressure balance as follows:

$$\Delta p = \Delta p_c - p_h = \frac{2\gamma \cos(\theta)}{r_c} - \rho g h(t) \quad (26)$$

The driving pressure for the fluid flow depends on the gravitational constant g , the actual height $h(t)$ and the fluid density ρ . Inserting Eq. (26) in Eq. (17), where $\bar{v}_z \hat{=} dh/dt$, $R \hat{=} r_c$ and $L \hat{=} h$, leads to the following equation for the fluid rise velocity:

$$\frac{dh}{dt} = \frac{r_c^2}{8\eta} \left(\frac{2\gamma \cos(\theta)}{r_c h(t)} - \rho g \right) \quad (27)$$

Based on Eq. (27) the final fluid height can be derived considering a fluid end velocity of zero. The result for this equilibrium state, which is known as Jurin's law, is then as follows:

$$h_{eq} = \frac{2\gamma \cos(\theta)}{r_c \rho g} \quad (28)$$

For the differential equation in Eq. (27) the analytical solution is as follows:

$$h(t) = \frac{2\gamma \cos(\theta)}{r_c \rho g} \cdot \left[1 + W \left(-e^{\left(-t \frac{r_c^3 \rho^2 g^2}{16 \eta \gamma \cos(\theta)} \right) - 1} \right) \right] \quad (29)$$

where W is the Lambert W function. The influence of the gravity for different capillary radii and for an exemplary set of parameters is depicted in Figure 17. The graphs represent the h - t -relationship without considering the hydrostatic pressure according to Eq. (25) (dashed lines) and with gravitational influence according to Eq. (29) (solid lines), respectively. Capillaries with bigger cross-sections lead to a faster rise but are affected to greater extent by gravity. In contrast to the L-W equation, Eq. (29) converges asymptotically to the equilibrium heights which are 408, 204 and 81.5 mm for the capillary radii 10, 20 and 50 μm , respectively. In conclusion, the choice whether the gravitational forces should be considered or not is dependent on the respective characteristics of the porous material and the fluid, the considered evaluation height and the degree of deviation which is defined as acceptable regarding the accuracy requirements.

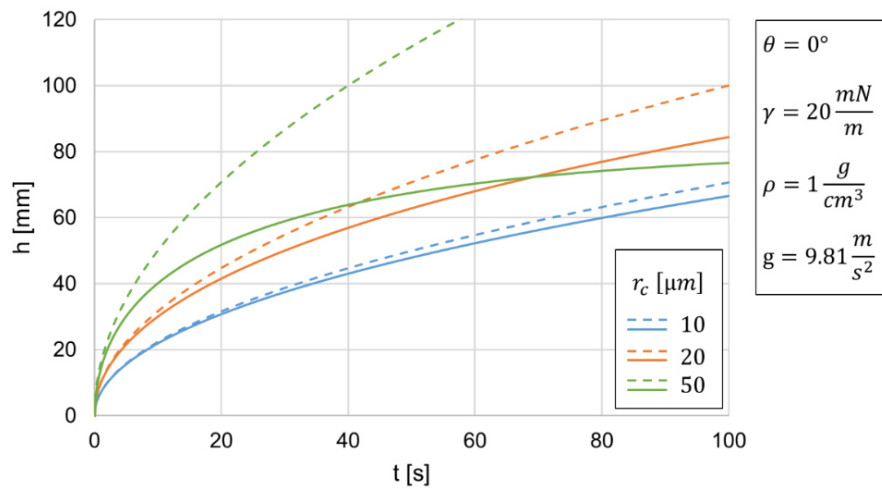


Figure 17: Capillary rise for different radii with (solid lines) and without (dashed lines) consideration of gravitational force

The porous tube model

Based on experimental results and evaluations, it was found that the Lucas-Washburn model is not capable to describe the imbibition process of fluids inside the porous structure of reinforcing textiles accurately. The corresponding function in Eq. (25) shows deviations from the empirical measurements especially with longer flow distances. This indicates that the assumptions and simplifications in this model are not sufficient for an adequate representation of the present fluid flow.

Due to the experimental observations of the capillary rise and the related fluid flow rate a modification of Washburn's approach is introduced, which includes a peripheral motion of the fluid besides the main flow inside the capillary pores. This effect is considered by a porous tube, which allows the fluid to flow across the capillary wall. A schematic presentation of this modified version of the pipe flow is depicted in Figure 18.

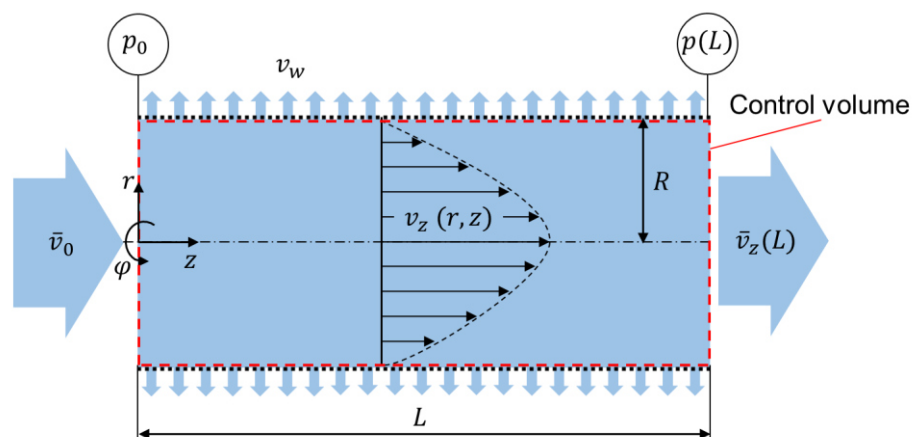


Figure 18: Schematics according to the porous capillary model

In comparison to the pipe flow with impermeable walls, the situation deviates from the unidirectional flow according to Poiseuille's requirements. Based on the assumption that the changes of the flow characteristics due to the transverse flow through the tube wall does not cause a critical presence of inertia or diverging viscous stresses, the lubrication approximation can be applied. The requirement for the considered deviations is that they appear as gradual that the flow state stays locally a Poiseuille flow. Further examples for the application of the lubrication approximation are slowly changing cross sections of tubes or gap heights in case of channel flows. [87]

Considering the simplifications due to the lubrication approximation, the Navier-Stokes equation for the z -component is as follows:

$$\frac{dp(z)}{dz} = \frac{\eta}{r} \frac{\partial}{\partial r} \left(r \frac{\partial v_z(r, z)}{\partial r} \right) \quad (30)$$

Analogous to the derivation of the flow velocity in the non-porous case (see appendix A.3), the pressure p is assumed as a variable only dependent on z . But since this time v_z depends on r and on z , the pressure gradient is not constant in the present case. The differential equation in Eq. (30) can be solved by integration analogous to the non-porous approach. Considering the no-slip boundary condition at the tube wall ($v_z(R, z) = 0$), which usually remains applicable at a porous surface, and regarding the restriction for the velocity to stay finite at the tube axis ($v_z(0, z) = \text{finite}$), the velocity distribution is as follows:

$$v_z(r, z) = -\frac{R^2}{4\eta} \frac{dp}{dz} \left(1 - \frac{r^2}{R^2} \right) = 2 \bar{v}_z(z) \left(1 - \frac{r^2}{R^2} \right) \quad (31)$$

The solution for v_z shows the same parabolic distribution as it was derived for the non-porous tube. Therefore, the mean velocity in z -direction \bar{v}_z is again half the maximum velocity at the tube axis (see Eq. (18)) which is:

$$\bar{v}_z(z) = \frac{dz}{dt} = -\frac{R^2}{8\eta} \frac{dp}{dz} \quad (32)$$

The relation between the mean velocity components at the inlet \bar{v}_0 , inside the tube at along the z -direction $\bar{v}_z(z)$ and the fluid velocity through the wall v_w is defined regarding the conservation of mass. The mass balance over a control volume as depicted in Figure 18, which represents a tube section of length L , is as follows:

$$\begin{aligned} \rho \bar{v}_0 R^2 \pi &= \rho \bar{v}_z(L) R^2 \pi + \rho 2\pi R \int_0^L v_w dz \\ \Leftrightarrow \bar{v}_0 &= \bar{v}_z(L) + \frac{2}{R} \int_0^L v_w dz \end{aligned} \quad (33)$$

In the following, v_w is defined to be constant along the tube wall, which leads to:

$$\bar{v}_z(z) = \bar{v}_0 - \frac{2 v_w z}{R} \quad (34)$$

Inserting Eq. (34) in Eq. (31) gives the equation for the pressure derivation, which can be integrated to find the local pressure difference along the tube:

$$\frac{dp}{dz} = -\frac{8 \eta}{R^2} \left(\bar{v}_0 - \frac{2 v_w z}{R} \right) \quad (35)$$

$$\int_{p_0}^p dp = \int_0^z -\frac{8 \eta}{R^2} \left(\bar{v}_0 - \frac{2 v_w z}{R} \right) dz \quad (36)$$

$$\Delta p = p_0 - p(z) = \frac{8 \eta \bar{v}_0 z}{R^2} \left(1 - \frac{v_w z}{\bar{v}_0 R} \right) \quad (37)$$

The use of Eq. (34) in Eq. (37) gives finally the following equation for the mean velocity over z , $\bar{v}_z(z)$:

$$\bar{v}_z(z) = \frac{R^2 \Delta p}{8 \eta z} - \frac{v_w z}{R} \quad (38)$$

As can be seen from Eq. (37) the peripheral fluid flow from the inside out ($v_w > 0$) leads to a reduction of the pressure drop over the tube length, which causes the following effects compared to a non-porous tube in context to the capillary rise:

- A present pressure drop, Δp , leads to a higher total fluid volume flow inside the porous tube.
- In a porous capillary with radius, r_c , the fluid velocity in tube direction is slower than in the non-porous case, which is evident by comparing Eq. (38) and Eq. (17).

According to the derivation from Deen [88] the two criteria for the application of the lubrication approximation on tubes with permeable walls are as follows:

$$Re_w = \frac{\rho |v_w| R}{\eta} \ll 1 \quad (39)$$

$$\frac{|v_w|}{\bar{v}_z} \ll 1 \quad (40)$$

The criterion in Eq. (39) is based on the Reynolds number for the peripheral fluid flow and ensures that inertial forces are negligible in relation to the present viscous

forces. The velocity ratio criteria in Eq. (40) proves the assumption that radial pressure variations can be ignored, thus the pressure gradient is only dominant in z -direction.

Analogous to the derivation of the L-W model, the pressure drop derived from the Young-Laplace equation (Eq. (21)) is considered as well as the gravitational influence on the pressure balance, as shown in Eq. (26). Inserting Eq. (26) in Eq. (38) gives the function for the ascend velocity of the fluid u inside the capillary:

$$u(h) = \frac{dh}{dt} = \frac{r_c^2}{8\eta h} \left(\frac{2\gamma \cos(\theta)}{r_c} - \rho g h \right) - \frac{v_w h}{r_c} \quad (41)$$

In this context the tube radius and the flow length are expressed using the capillary radius r_c and the fluid height h , respectively, as depicted in Figure 19.

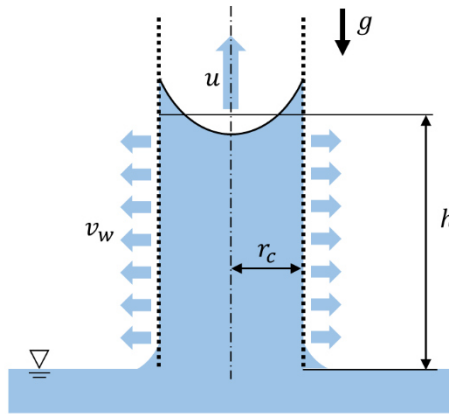


Figure 19: Schematics according to the fluid rise inside a capillary with porous tube walls

If Eq. (41) is rearranged as follows, the influences of the considered effects in this model approach become clear:

$$u(h) = \frac{r_c}{4h} \frac{\gamma \cos(\theta)}{\eta} - \frac{r_c^2}{8\eta} \rho g - \frac{v_w h}{r_c} = u_{LW}(h) - u_g - u_w(h) \quad (42)$$

The first term u_{LW} is equivalent to the fluid velocity inside the capillary tube proposed by the Ludwig-Washburn model according to Eq. (22). The second term u_g considers the effect of the gravity which acts against the vertical flow. The third term u_w represents the influence of the fluid flow through the porous tube wall and is

intended to compensate the deficiencies of the original L-W equation, as mentioned above.

The transition from inertial to viscous flow

The presented approaches and derivations to describe the dynamic flow inside capillaries disregard any inertial forces. This is in many cases a reasonable approximation if the time domain which is needed to reach a viscous dominated flow is very short. As can be seen from the equations for the fluid velocity so far, the neglect of inertial forces then leads to a singularity at the initial point ($h = 0$) since the corresponding velocity becomes infinite.

To check the influence of inertial forces at the very start of the fluid imbibition into the porous material and to provide detailed information according to the transition from inertial to viscous flow, different solutions for the different time domains are presented in the following. The linear balance of momentum, which correlates with the acting forces during the fluid flow inside a capillary is given as follows [89]:

$$\frac{2\gamma \cos(\theta)}{r_c} = \frac{d(\rho h\dot{h})}{dt} + \frac{8\eta}{r_c^2} h\dot{h} + \rho g h \quad (43)$$

The capillary pressure on the left side of Eq. (43) counteracts against and balances with the sum of inertial, viscous and hydrostatic forces, which are expressed by the terms on the right side, respectively. With the definition of the parameters a , b , and c as follows:

$$a = \frac{r_c \rho}{2\gamma \cos(\theta)} \quad (44)$$

$$b = \frac{4\eta}{r_c \gamma \cos(\theta)} = \frac{8\eta}{r_c^2 \rho} \cdot a \quad (45)$$

$$c = \frac{r_c \rho}{2\gamma \cos(\theta)} g = g \cdot a \quad (46)$$

Eq. (43) becomes:

$$\frac{1}{a} = \frac{d(h\dot{h})}{dt} + \frac{b}{a} h\dot{h} + \frac{c}{a} h \quad (47)$$

Inertial domain

For the case of a purely inertial flow Quere [90] obtains a solution by neglecting the viscous and the hydrostatic term. The differential equation is then as follows:

$$\frac{1}{a} = \frac{d(h\dot{h})}{dt} \quad (48)$$

with the corresponding solution for the capillary rise:

$$h(t) = \frac{1}{\sqrt{a}} t \quad (49)$$

Inertial-viscous domain

Bosanquet [91] considers both inertial and viscous forces, which accurately describes the transition between the purely inertial and purely viscous flow regime. He neglects the gravity term in Eq. (47) that gives:

$$\frac{1}{a} = \frac{d(h\dot{h})}{dt} + \frac{b}{a} h\dot{h} \quad (50)$$

and obtains the following analytical solution for the differential equation:

$$h(t) = \sqrt{\frac{2}{b} \cdot \left[t - \frac{a}{b} \left(1 - e^{-\frac{b}{a}t} \right) \right]} \quad (51)$$

Viscous domain

The purely viscous flow is represented by the Lucas-Washburn equation [82] which was derived before. The neglect of the inertia term and the absence of gravity influence leads to the differential equation:

$$\frac{1}{a} = \frac{b}{a} h\dot{h} \quad (52)$$

with the solution:

$$h(t) = \sqrt{\frac{2}{b} t} \quad (53)$$

which is equivalent to the previously derived function in Eq. (25).

The three functions of Eq. (49), (51) and (53) related to Quere's, Bosanquet's and Washburn's approach, respectively, are depicted in Figure 20 for an exemplary set of parameters.

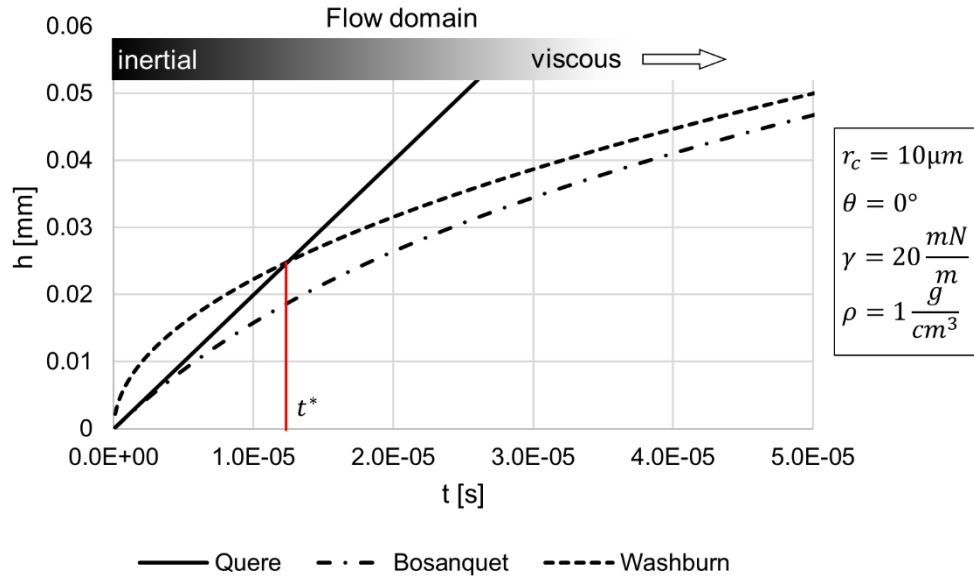


Figure 20: Transition from inertial to viscous flow inside a capillary

There are various criteria which can be applied to divide the sections into inertial dominant and viscous dominant domains, eventually with an additional inertial-viscous transition domain in between [92]. In the present work the intersection point between Quere's and Washburn's approach is used to analyze the critical time domain in which inertial forces are dominant. The corresponding time t^* results from equalizing Eq. (49) and Eq. (53) which becomes:

$$t^* = \frac{2a}{b} = \frac{r_c^2 \rho}{16\eta} \quad (54)$$

where a and b are variables as defined in Eq. (44) and Eq. (45), respectively. Therefore, the relevant parameters which define t^* are the capillary radius r_c , the fluid density ρ and the dynamic viscosity η .

2.3 Thermoset matrix systems

Thermoset polymers are characterized by irreversible cure reactions from viscous or liquid prepolymers to a solid state with a three-dimensional cross-linked molecular structure. They are used in LCM processes for the manufacturing of fiber reinforced composite parts since they are capable to fulfill the following requirements for that purpose [29]: (i) low viscosity for good fiber wetting and impregnation, (ii) high and controllable reactivity on curing, (iii) chemical control of cure without detrimental volatile formation, (iv) low shrinkage and (v) good mechanical and thermomechanical properties. In contrast to thermoplastic polymers, they cannot be melted and reshaped once hardened but offer generally better mechanical properties, temperature and chemical resistance and a lower viscosity in the non-cured state.

There are various thermoset polymer systems available based on different chemical precursors and different polymerization reactions. Each type has its own characteristics profile, which can be found in the pertinent literature [35], [93]. The most relevant thermoset types for the use as matrix component in fiber reinforced parts are unsaturated polyester, vinyl ester, epoxy and phenolic resins [29], [35]. Their usage in combination with natural fiber reinforcements is subject of various studies [9], [12], [94]–[98]. In recent years great effort was also made in the development of thermosets which based on renewable resources with the overall objective to enhance the ecological benefits of NFRPs [14], [99]–[102].

In the following, the reaction-specific basics and properties exemplarily for epoxy resins are presented since this type was considered in the course of the present work. Epoxy thermosets are characterized by high mechanical and thermal properties, high water resistance and low cure shrinkage [36]. A drawback is their higher costs compared to polyester or vinyl ester resins, which is one critical factor for their widespread use [31]. The most common types of epoxy resins based on the prepolymer diglycidyl ether of bisphenol A (DGEBA) which provides two functional epoxy groups [93]. For their polymerization reaction by addition the epoxy group needs a hardener component which provides an 'active' hydrogen atom (e.g. alcohols, acids, amides or amines). Hardener agents based on polyamines constitute the largest group of epoxy curing agents [93]. The structural chemical

formula of DGEBA and a diamine are depicted in Figure 21 a). Each amine group provides two hydrogen atoms which can react with the epoxy group as a primary (R-NH₂) and secondary amine (R-NH-R), respectively. The corresponding addition reaction is depicted in Figure 21 b). The right stoichiometric ratio between the resin and the hardener component plays an essential role in case of epoxy thermosets to minimize the amount of unreacted groups and to achieve best mechanical properties.

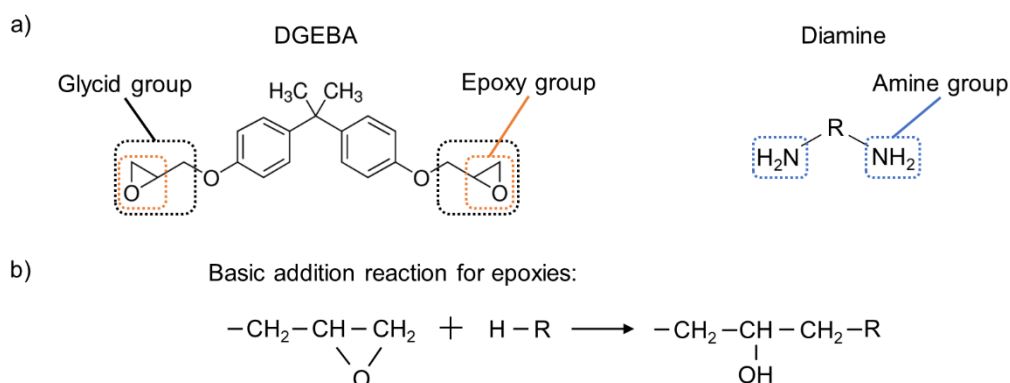


Figure 21: Epoxy chemistry: a) Structural chemical formula of bisphenol A diglycidyl ether (DGEBA) and diamine; b) Basic addition reaction [103]

A schematic representation of the curing process which describes the transfer from an initially viscous fluid to a glassy solid is depicted in Figure 22. The polymerization by addition and cross-linking leads to an increase of the molecular weight which is related to an increase of the viscosity of the liquid resin-hardener mixture. The gelation point marks the state where the polymer loses its capability to flow and correlates with the development of the molecular network to a macroscopic extent. With further conversion the polymer behaves like a solid and the cross-linking of the remaining reactive groups continues until the final degree of cure and the corresponding mechanical and thermal properties are reached.

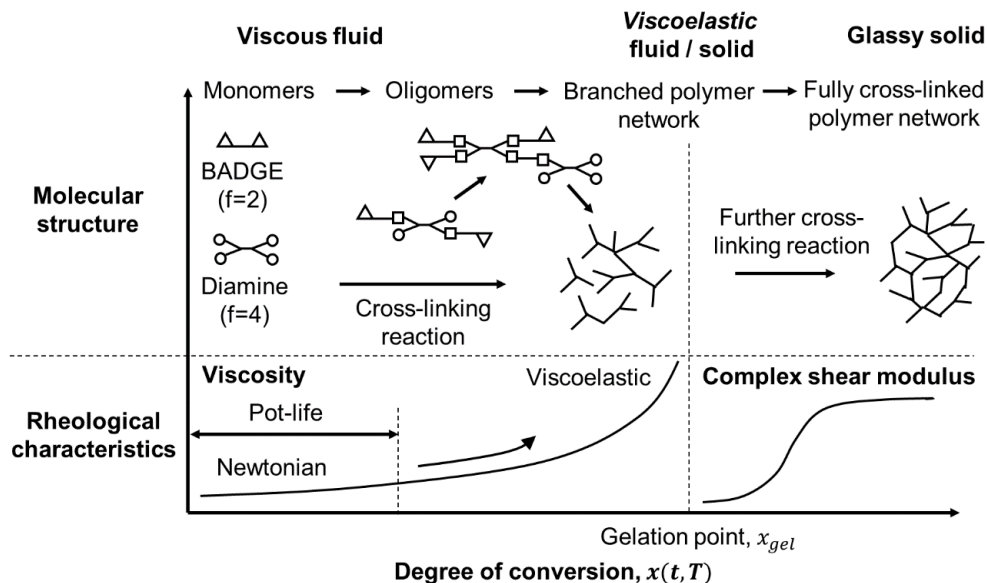


Figure 22: Reaction schematics of an epoxy-diamine thermoset system (adapted from [104])

The knowledge of the property changes during the reaction is a key factor for LCM processes. The impregnation mechanisms significantly depend on the viscosity of the fluid as shown in the previous chapters. The increase with progressing cure conversion limits the available processing time for the impregnation step which is related to the so-called pot-life, which specifies the duration until a predefined viscosity limit is reached. Furthermore, the reaction rate is strongly affected by the processing temperature which must be considered. Therefore, the design of LCM processes generally requires a compromise related to the polymer system which must provide a suitable amount of time for the impregnation in a low viscous state but cures fast enough to ensure economically reasonable production times.

2.4 Flow-induced void formation in liquid composite molding processes

During the impregnation, the liquid polymer system is injected or infused into the mold cavity to fill the porous spaces of the prepared fibrous reinforcement. This step is a crucial key factor during the LCM processing since it must be ensured that the porous volume inside the cavity is filled completely before the reactive resin system reaches a viscosity state that prohibits a further flow progression. Furthermore, the fluid flow through the complex pore structure of the fibrous reinforcement is driven

by different mechanisms which are related to the local pore sizes. While in larger pore channels the flow is dominated by viscous forces rather than capillary forces, the situation is vice versa in smaller spaces. This situation of competing forces becomes apparent especially for reinforcing fabrics with a dual-scale pore characteristic. This is generally the case when the textile architecture consists of yarns or fiber bundles, as shown in chapter 2.1.1. The pore sizes are classified as microscopic pores and macroscopic pores which are located inside and between the yarns, respectively. The presence of various pore sizes is prone to generate flow-induced voids. Figure 23 a) depicts the formation mechanisms of voids during the saturation process schematically.

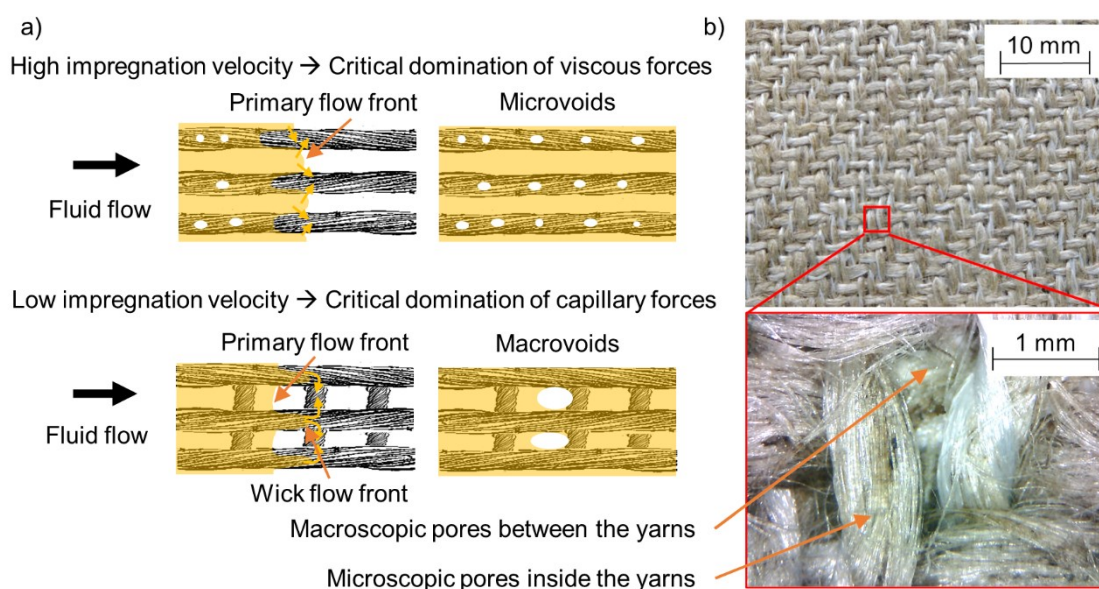


Figure 23: Dual scale pore size distribution of reinforcing textiles. a) Schematic formation of flow-induced voids, b) Pore structure in a woven flax fiber textile

In case of dominating viscous forces the impregnation of the microscopic pores lags which leads to inclusions of microvoids inside the fiber bundles. Macrovoids on the other hand result from a faster wicking flow front inside the smaller pore spaces due to dominating capillary forces. The woven flax fiber fabric depicted in Figure 23 b) illustrates the dual-scale pore size distribution and the complex interconnected network of flow channels inside the reinforcing structure.

The investigation of underlying mechanisms for void formation was subject of several previous studies with the objective to find optimal process settings for the

textile impregnation. In the studies from Patel & Lee [105]–[107] and Mahale [108] the influence of the impregnation velocity on the resulting void content and void types were investigated for various glass fiber reinforcements via optical detection approaches. Based on their results they found a logarithmic relationship between the void content and the fluid velocity for micro- and macrovoids, respectively, as it is illustrated in Figure 24. This principle states that an optimal impregnation velocity can be derived, which leads to a minimal amount of flow-induced voids inside the composite part.

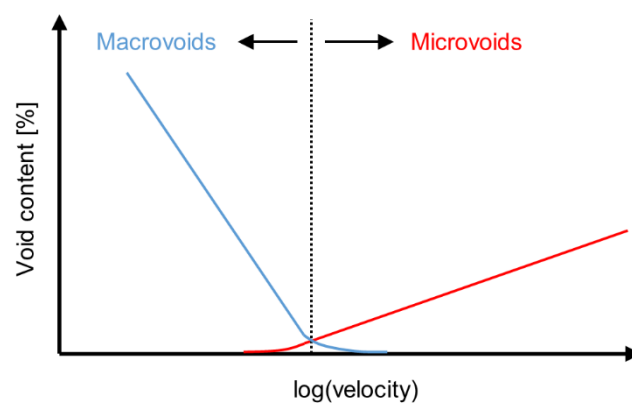


Figure 24: Theoretical void content inside the composite as a function of the impregnation velocity (Adapted from [109])

Since this phenomenon is significantly affected by the fluid properties a more general expression is used which based on the capillary number. The capillary number Ca is a dimensionless quantity representing the relation between viscous forces and the liquid surface tension, which is defined as follows:

$$Ca = \frac{\eta U}{\gamma} \quad (55)$$

where η is the dynamic viscosity, U a characteristic velocity value and γ the surface tension of the liquid. Patel also proposed a modified capillary number, which shows a better consistency when using different fluids with varying wetting properties [109]. The modified capillary number Ca^* considers the advancing contact angle θ of the fluid-fiber interface and is defined as:

$$Ca^* = \frac{\eta U}{\gamma \cdot \cos(\theta)} \quad (56)$$

In the pertinent studies the characteristic velocity U is generally defined as the pore velocity v_p . The modified capillary number which is therefore related to the optimum impregnation velocity is a key parameter for injection or infusion processes in terms of void minimization.

In addition to the studies mentioned above this approach was also used by Ruiz [110], Labat [111] and Leclerc [112] to optimize the injection flow rate in RTM processes. For a unidirectional stitched fiber glass mat an optimal capillary number was derived and the flow dependent void formation was also applied in filling simulations for flow rate optimization [110], [111]. Moreover, void measurements and mechanical tests on composite plates made of two types of glass fiber textiles (woven fabric, multiaxial NCF), respectively, and with varying impregnation settings indicated optimal impregnation velocities for a vinylester and an epoxy resin systems used in the related research work [112]. The studies from Chen *et al* on the wetting of different glass fiber fabrics confirm the principles of void formation resulting from a present dual-level porosity scale [113], [114]. In addition to the experimental observations, the consideration of viscous and capillary forces during the unsaturated flow is also the basis of various model approaches to simulate void formation and the mobilization of voids due to the fluid flow [105], [106], [114]–[117].

The optimization approach based on the capillary number considers the right balance between the viscous and the capillary flow during the impregnation. While the viscous flow can be controlled by the process parameters for the fluid injection via an applied pressure difference or predefined flow rate, the capillary driven flow is defined by the pore structure of the reinforcement. Strategies to determine optimal impregnation velocities therefore focus on the characterization of the capillary action inside the fabrics, as it was already applied by capillary rise experiments in previous studies. LeBel presented in his studies an experimental approach for the capillary rise measurement in glass fiber fabrics using a monitoring technique with a luminous fluorescent dye in the test fluid [118], [119]. In these experiments an upright textile sample is dipped in a wetting test fluid which imbibes into the porous structure due to capillary forces as schematically depicted in Figure 25 a).

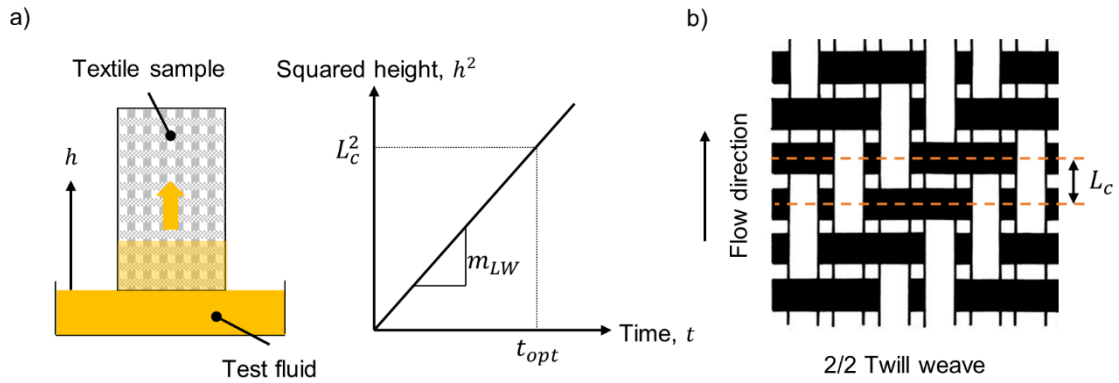


Figure 25: a) Schematics of the capillary rise experiment and the Ludwig-Washburn (L-W) model; b) Characteristic mesoscopic length of a woven fabric

The capillary rise over time is generally detected via optical methods and/or by measuring the weight progression of the wicking fluid. The evaluation of the resulting fluid progression based on the Lucas-Washburn (L-W) model as presented in chapter 2.2.3. In accordance with the L-W equation (Eq. (25)), the linear relationship between the squared imbibition height h^2 and the time t is defined by its slope m_{LW} as follows:

$$h^2 = m_{LW} \cdot t \quad \text{where} \quad m_{LW} = \frac{\gamma \cos(\theta)}{2\eta} \cdot r_c \quad (57)$$

For the derivation of the optimal impregnation velocity, it was hypothesized that it corresponds with the imbibition time which is needed to reach a height equivalent to the so called 'characteristic mesoscopic distance' L_c of the reinforcing fabric. L_c orients towards the repeating pattern (unit-cell) of the fabric. For the biaxial glass fiber NCF, LeBel used in his studies, L_c was defined as the distance between two rovings oriented perpendicular to the flow direction. A similar approach to predict void formation by considering the yarn distance of a woven fabric was also applied by Parnas [120]. The corresponding mesoscopic distance for a 2/2 twill weave fabric is depicted in Figure 25 b). Figure 25 a) illustrates the L-W model and the time t_{opt} which corresponds to the capillary flow distance L_c . According to Eq. (57), the flow time t_c is then:

$$t_c = \frac{L_c^2}{m_{LW}} \quad (58)$$

Considering the hypothesized criterion and Eq. (58), the optimal impregnation velocity is as follows:

$$v_{p,opt} = \frac{L_c}{t_c} = \frac{m_{LW}}{L_c} \quad (59)$$

This definition was also used by Ravey [121], [122] and Causse [123] who analyzed the capillary rise inside glass and carbon fiber fabrics by infrared thermography and investigated to void contents in RTM made composite test plates, respectively. Their results confirm the applicability of this approach for the determination of optimal impregnation velocities.

Regarding the velocity progression of the capillary rise as it is defined by the L-W model, the ascendt velocity according to Eq. (22) is:

$$u(h) = \frac{m_{LW}}{2h} \quad (60)$$

The comparison of Eq. (60) and Eq. (59) shows that the optimal impregnation velocity can therefore be interpreted as the velocity which is reached at a height h of $L_c/2$ during the capillary rise experiment.

$$v_{p,opt} = \frac{m_{LW}}{L_c} = u\left(\frac{L_c}{2}\right) \quad (61)$$

This is seen as a clearer expression since it describes the modeled distance of the wicking flow front ahead of the primary flow front in a scenario with continuous flow front propagation in accordance with the flow schematics depicted in Figure 23 a).

While the investigations on this topic is almost entirely done on man-made fiber fabrics based on glass and carbon fiber bundles, the application of this approach on natural fiber fabrics was rarely considered yet. Therefore, the analysis of the capillary action in flax fiber fabrics based on capillary rise experiments was intended as a focus topic in the present work, which is covered in chapter 5.

3 Materials

In this chapter the composite constituents which were considered in this work are presented with a focus on the flax fiber reinforcements and their characteristics. These textiles were used for the characterization of the fluid flow inside the reinforcement in the further course. The relevant properties of the epoxy system used for the composite manufacturing and subsequent analysis are included in this chapter, while auxiliary test fluids used for the characterizations are presented in the respective chapters related to the permeability (chapter 4) and the capillarity (chapter 5) characteristics.

3.1 Flax fiber reinforcements

The selection of the textile fabrics was done with the intention to cover a wide variety of different fibrous architectures. Moreover, it was chosen to focus on flax fibers to maintain a comparability of the textile's behavior without the influence of the fiber type itself. Flax fibers belong to the most performant plant-based fiber types in terms of mechanical strength and stiffness. Furthermore, the availability of this fiber is high in the European region. The popularity of flax fibers for the intended usage in NFRP composites can be seen from the latest developments to optimize the textile manufacturing methods and the structure of reinforcing fabrics for that purpose, as mentioned in chapter 2.1.1.

For the investigations in this work a non-woven flax fiber fabric type, two different woven textiles and a fabric with unidirectional yarn orientation were considered. The specifications of each fabric type can be seen in the following Table 4 to Table 7. In this context it shall be mentioned that some information from the technical data sheets varied significantly compared to the own measurement results. This applies in particular the fabric areal weight FAW of the non-woven fabrics 'Fibrimat F300 and F450' (Table 4) and the unidirectional textile 'AmpliTex® Art.No. 5009' (Table 7). The determination of the weave densities of the warp and weft yarn systems in the two woven textiles 'Biotex Flax 200g/m² and 400g/m²' reveals some divergences from an intended balanced weave style. Especially the heavier 400 g/m² woven fabric (Table 6) shows a significant difference between the warp and weft direction with mean weave densities of 6.6 yarns/cm and 8.7 yarns/cm, respectively.

Table 4: Specifications for the non-woven fabrics: Fibrimat F300 and F450

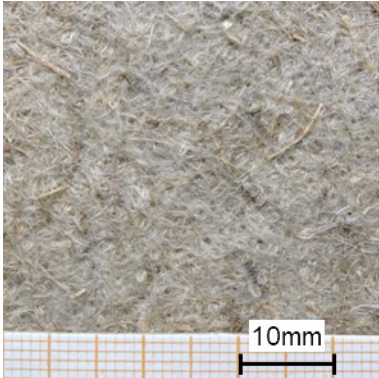
Fibrimat F300 and F450 Abbreviation: NW300 and NW450		
		
Specifications:		
Manufacturer	Eco-Technilin SAS (Valliquerville, France)	
Fiber type	Flax	
FAW	300 ($\pm 10\%$) g/m ² *)	450 ($\pm 10\%$) g/m ² *)
	257 \pm 14 g/m ² **)	428 \pm 29 g/m ² **)
Preferential fiber direction:	Roll axis *)	
*) according to Datasheet [124], [125]; **) based on own measurements		

Table 5: Specifications for the woven fabric: Biotex Flax 200g/m² 2x2 Twill

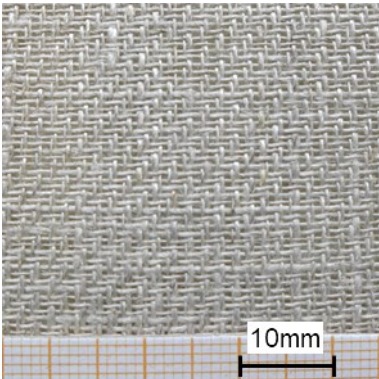
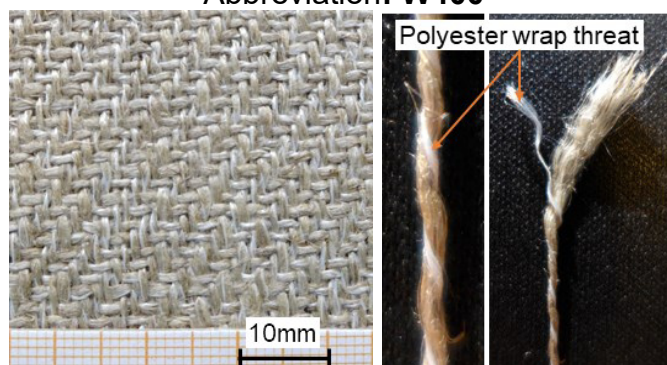
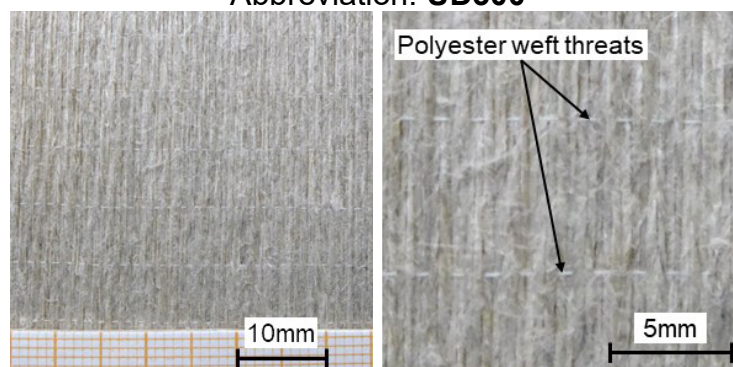
Biotex Flax 200g/m² 2x2 Twill Abbreviation: W200		
		
Specifications:		
Manufacturer	Composites Evolution Ltd. (Chesterfield, UK)	
Fiber type	Flax	
Yarn	Low-twist technology	
Weave Style	2x2 Twill	
FAW	200 g/m ² *)	201 \pm 2 g/m ² **)
Weave density	Warp: 11.9 \pm 0.2 cm ⁻¹ **)	Weft: 12.6 \pm 0.2 cm ⁻¹ **)
*) according to Datasheet [126]; **) based on own measurements		

Table 6: Specifications for the woven fabric: Biotex Flax 400g/m² 2x2 Twill**Biotex Flax 400g/m² 2x2 Twill**Abbreviation: **W400**

Specifications:

Manufacturer	Composites Evolution Ltd. (Chesterfield, UK)	
Fiber type	Flax	
Yarn	Twistless technology: Flax fiber strand wrapped by polyester thread	
Weave Style	2x2 Twill	
FAW	400 g/m ² *)	405 ± 3 g/m ² **)
Weave density	Warp: 8.7 ± 0.2 cm ⁻¹ **)	Weft: 6.6 ± 0.2 cm ⁻¹ **)

*) according to Datasheet [127]; **) based on own measurements

Table 7: Specifications for the unidirectional fabric: AmpliTex[®] Art. No. 5009**AmpliTex[®] Art. No. 5009**Abbreviation: **UD300**

Specifications:

Manufacturer	Bcomp Ltd. (Fribourg, Switzerland)	
Fiber type	Flax	
Yarn	Warp: 106 tex*), Weft: textured polyester	
Weave Style	2x2 Twill	
FAW	300 (±5%) g/m ² *)	261 ± 5 g/m ² **)
Weave density	Warp: 26.7 ± 0.3 cm ⁻¹ **)	Weft: 1 cm ⁻¹ *)

*) according to Datasheet [128]; **) based on own measurements

3.2 Epoxy resin system

The thermoset system which was used in the course of this work is an epoxy infusion resin provided by bto-epoxy GmbH (Austria). The epoxy system consists of a resin component (Epinal LR80-A2.01) and an amine-based hardener component (Epinal LH80-B2.00) with a resin-hardener mixing ratio of 100:25 by weight. The recommended temperature range for the processing and curing is from room temperature up to 90°C [129].

For further characterization of this epoxy system the viscosity progression for isothermal cure between 50°C and 70°C was determined using a Physica MCR 501 rheometer from Anton Paar GmbH (Austria) with a parallel-plate measuring system (PP 50). The results of the dynamic viscosity over time within the first 30 minutes are depicted in Figure 26 a).

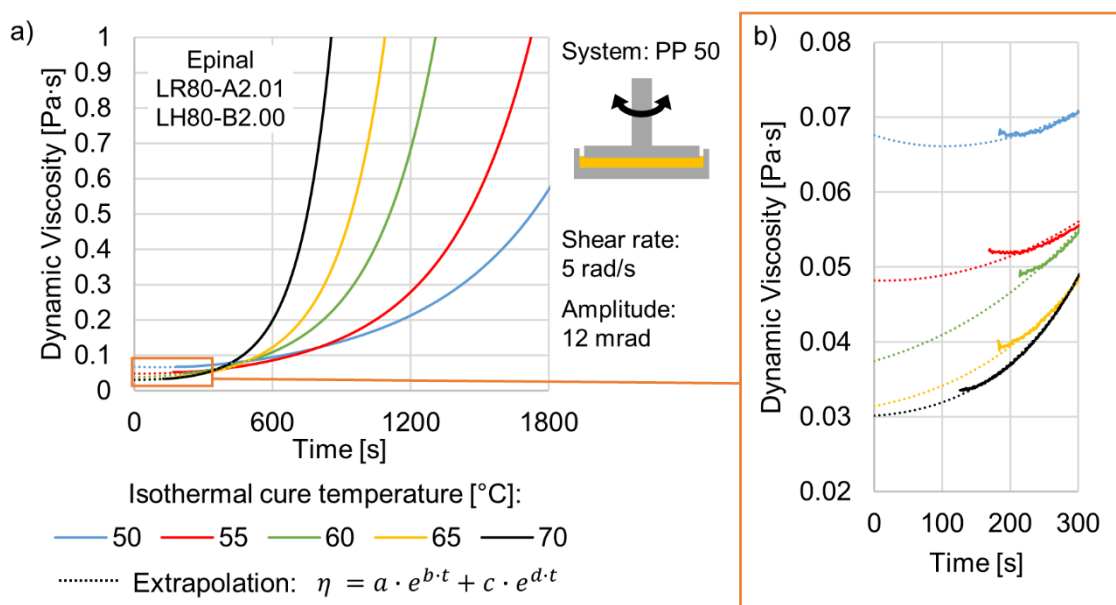


Figure 26: Viscosity measurements on the epoxy system:
Epinal LR80-A2.01/LH80-B2.00

As discussed in chapter 2.3, the reaction speed increases with increasing temperature which causes lower initial viscosity values but a faster progression over time. Due to the rheometric measurement procedure including the mixing, pouring and the starting process, the viscosity values of the reactive system were not available from the very start of the polymerization. Therefore, the initial viscosity values were extrapolated subsequently, considering the duration between the

pouring of the mixture into the preheated measuring system and the start of the data acquisition. A two-term exponential fit function was found to be capable to accurately fit the viscosity data in the first phase up to 0.2 Pa·s, as shown in Figure 26. Based on the measurement results the dynamic viscosity is known in the time ranges which are of interest for the impregnation step in LCM processes. The initial values of the epoxy system based on the extrapolated data can be seen in the diagram of Figure 26 b). Within the regarded temperature range (50 - 70°C) the initial dynamic viscosity is between 30 and 70 mPa·s with a decreasing trend at higher temperatures.

4 Characterization of the in-plane permeability

The preform permeability, as introduced in chapter 2.2.2, is a relevant material parameter of the fibrous reinforcement used in LCM processes. The accurate characterization allows the calculation and prediction of the resin flow through the porous structure inside the mold cavity depending on the preform characteristics, fluid properties and process parameters. These preliminary simulations can be used for a proper design of the RTM tooling with an optimized injection strategy, but also to determine necessary injection pressures and filling times. This affects the structural design of the tools and clamping systems as well as the applicable resin systems in terms of their viscosity and reactivity properties. Consequently, the permeability characterization contributes to a more predictable and reliable production planning for LCM processes. [17], [57]

Since the permeability characteristics are influenced very specifically by the structural features of the textile fabric, like the actual porosity content, the architecture of the fiber reinforcement and the yarn construction, theoretical approaches of general validity are impeded due to the overall complexity. Therefore, the empirical determination via fluid flow experiments is seen as the most reliable way to measure the relevant preform permeabilities for the specific cases. [57]

In the following, the experimental setup is presented which was used for the in-plane permeability test series. Subsequently, the resulting permeability values of the three considered fabric types (non-woven: NW450, woven: W400 and unidirectional: UD300) are shown and discussed.

4.1 Experimental setup

The preferential test stand for the permeability characterization in this work is a measuring system with capacitive line sensors embedded inside a rigid RTM plate mold. The capacitive sensor approach is used for the online fluid flow front detection, which was developed and constructed by PMB Präzisionsmaschinenbau Bobertag GmbH (Germany). The schematic of the experimental setup as well as the test mold installed inside the mold carrier are depicted in Figure 27 a) and b), respectively. The test stand consists of a fluid tank which is connected to the compressed air

supply. A control valve is used to adjust to pressure inside the fluid tank. The textile sample stack (preform) is placed inside the test mold cavity on top of the radially arranged capacitive sensors and is subsequently compacted to the intended thickness, which is defined by the dimension of the changeable cavity frame. A round cut-out in the center of the preform with a diameter of 13 mm, positioned beneath the fluid inlet hole of the upper mold, ensures the necessary boundary conditions for the in-plane permeability characterization, as shown in chapter 2.2.2. The injection starts with the opening of the check valve, to let the test fluid flow inside the test mold and inside the porous textile reinforcement. A tool mounted pressure sensor at the fluid inlet measures the actual injection pressure. A control computer acquires the data from the eight capacitive sensors and the pressure sensor during the experiment.

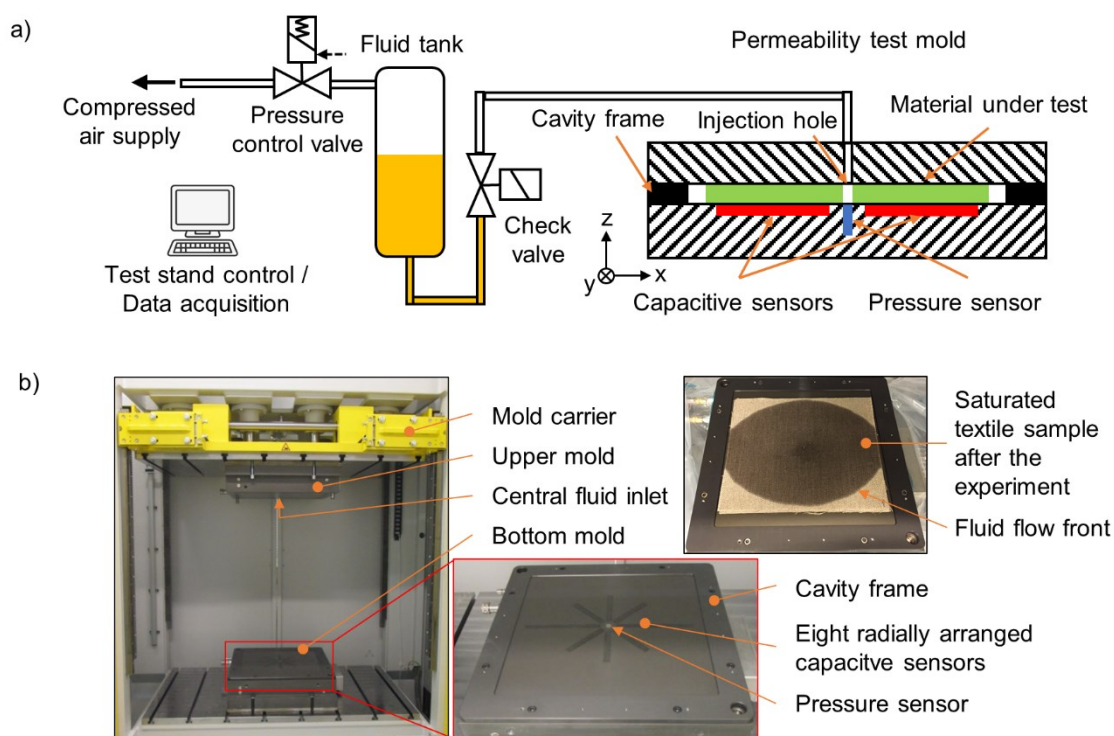


Figure 27: Capacitive permeability test stand: a) Schematic test setup, b) Installed permeability test mold

The principle of the capacitive measurement approach for the flow front detection in the present setup is related to the functionality of a plate capacitor, which consists of the linear sensor itself and the upper steel mold as counterpart on the opposite side. The material in between defines the permittivity, thus the capacity of the

capacitor. Therefore, the fluid flow inside the porous textile along the capacitive sensor causes a change in capacity, which is expressed in the present setup via a proportional capacitive equivalent. Based on the signal changes and the flow direction monotonously from the inside out, the actual flow front position along the linear sensor can be determined. [130]

A typical progression of the capacitive equivalent of one of the eight sensors is depicted in Figure 28 a). The initial signal plateau corresponds to the sensor capacity with the compacted, completely dry textile sample. As soon as the fluid reaches the sensing area the permittivity rises, due to the exchange of air in the porous volume by the fluid. After the porous material above the sensor is completely saturated, the capacitive equivalent remains constant. Six sensors have a length of 105 mm while two sensors at opposing sides (west and east direction) offer a longer measurable range of 185 mm. A schematic representation of the test mold cavity with the positions of the eight capacitive sensors and the calculated flow front positions at one point during the experiment is shown in Figure 28 b).

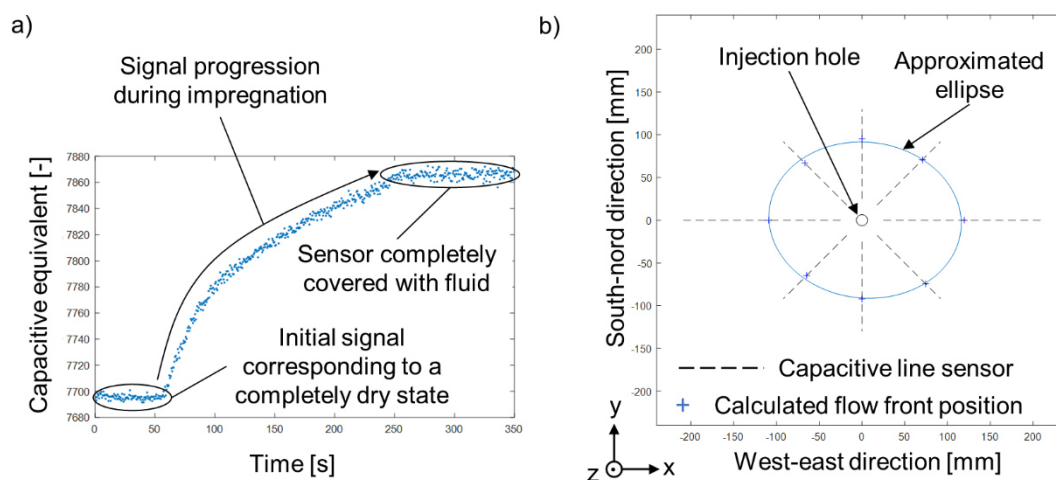


Figure 28: Evaluation of the capacitive sensor data: a) Typical signal progression of one sensor during test, b) Approximation of the elliptical flow front progression

The approximation of the elliptic flow front progression was done following the strategy described by Fauster *et al* [131], which based on the fitting principles published by O'Leary *et al* [132], [133] and Harker *et al* [134]. Based on this algorithm the ellipse in the observed plane which has five degrees of freedom is characterized by its midpoint, the angular orientation, and the major and minor axis

lengths. The geometric information of the length progression of the major and minor half-axis is used to calculate the permeability in the principle directions according to the method from Adams *et al* [62]. Preliminary evaluations which use alternative ellipse fitting approaches, namely the method from Bookstein [135] and the method from Pilu, Fitzgibbon and Fisher [136], [137], did not show any significant influences on the resulting permeability characteristics. This indicates that the intended even distribution of the eight evaluated points of the flow front offers good conditions for a robust and clear ellipse approximation independent of the underlying fitting algorithm.

Besides the geometrical information of the fluid progression inside the porous materials, the pressure data and the fluid viscosity play a decisive role for the permeability determination.

The fluid pressure was measured with the pressure sensor at the central inlet position, as depicted in Figure 27. The injection pressure was kept constant during the impregnation and represents the pressure state at the inlet boundary of the porous material, which is defined by the round cut-out in the center of the preform. At the position of the moving fluid front the pressure is assumed to correspond with the atmospheric pressure, thus any capillary pressures are neglected.

The test fluid used for the permeability characterization is a plant oil based on sunflower and rapeseed oil (Bona Feinstes Pflanzenöl, VFI GmbH, Austria), which shows a suitable viscosity at room temperature in the range of typical polymer resin systems used for LCM processes. The fluid viscosity for relevant temperatures was measured on a Physica MCR 501 rheometer from Anton Paar GmbH (Austria) using a double gap cylinder system DG26.7 and a constant shear rate of 5 s^{-1} . The temperature dependent viscosity was determined in the range between 12 °C and 35 °C with a temperature rate of 1 °C/min . The results are depicted in the diagram of Figure 29. A difference between the heating and the cooling cycle can be observed which is most likely due to a delayed temperature progression inside the test fluid itself. Thus, for the definition of the actual dynamic viscosity at a given temperature the mean regression curve based on an exponential function is used, as shown in Figure 29. The actual fluid temperature during the conduct of the permeability experiments was measured using a Voltcraft PL-120 T1 (Conrad

Electronic SE, Germany) temperature-measuring device with a type K thermocouple which was in the range between 21.0°C and 21.9°C throughout all test series.

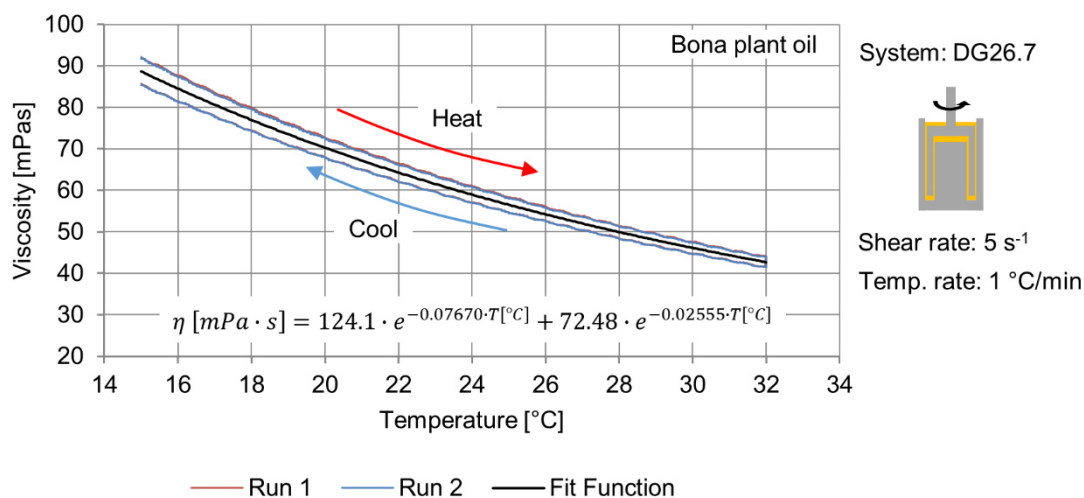
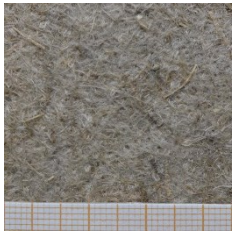
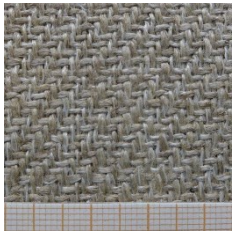
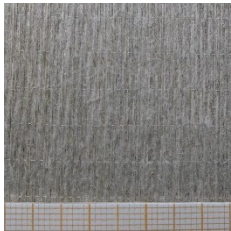


Figure 29: Viscosity measurement on the plant oil test fluid

Table 8 gives an overview of the test configurations considered in this work, which are specified by the fabric type and the combination of cavity height and number of textile layers, which defines the resulting fiber volume and porosity content according to Eq. (3) and Eq. (4), respectively. An additional variation of the set fluid pressure and the corresponding infiltration velocity was considered to check the dependence of this parameter on the resulting permeability values. To extend the considered porosity range for the subsequent model derivation two test series were included, which were conducted on a second in-plane permeability test stand with a transparent upper mold and optical, camera-based flow front detection. This optical test setup was previously presented and analyzed by Grössing [138]. The disadvantage of the related test setup is its vulnerability for mold deflection which leads to an increasing unreliability and error of the evaluated results with higher compaction and injection pressures. This effect was revealed by Grössing [138], who compared the permeability results of carbon fiber fabrics determined with the optical and the capacitive test stand, respectively. Based on the considerable and pressure dependent discrepancies, the mold deflection was found to be a significant error source for the in-plane permeability characterization. These detrimental effects can be confirmed in context with the present natural fiber characterization and based on preparatory test series on the optical test setup with different flax fiber fabrics

and varying fiber volume contents. It was found that the deflection affects not just the resulting absolute permeability values but also the anisotropy characteristics due to the bended mold shape and an accompanying uneven sample height inside the cavity. Therefore, only the test series with the lowest fiber volume content and low injection pressures were considered for the permeability characterization in the present work. This increases the considered porosity range for the W400 and UD300 fabric while minimizing the risk of measurement inaccuracies.

Table 8: Test configurations specified by fabric type, cavity height, number of layers, injection pressure and test stand

	Fabric type		
	NW450	W400	UD300
			
Capacitive	4mm/3L/2bar	4mm/6L/2bar	2mm/6L/2bar
Test stand	4mm/3L/6bar	4mm/6L/6bar	2mm/6L/6bar
	4mm/4L/2bar 4mm/4L/6bar	4mm/7L/6bar	2mm/7L/6bar
Optical		4mm/5L/2bar	3mm/6L/2bar
Test stand			

4.2 Test results and discussion

In the following, the results from the in-plane permeability measurements for the non-woven fabric NW450, the 2/2 twill woven fabric W400 and the unidirectional textile UD300 are depicted in the diagrams of Figure 30, Figure 31 and Figure 32, respectively. The results contain the permeability values in the principal directions k_1 and k_2 , the related anisotropy factor α and the angular orientation of the corresponding ellipse ϑ with respect to the textile direction.

The comparison of the three considered flax fiber fabrics reveals the differences of the corresponding anisotropy characteristics. While the non-woven fabric NW450 shows the lowest anisotropy, correlating with a high anisotropic factor α in the range between 0.61 and 0.86, the anisotropy in the UD300 textile is considerable higher indicated by α values closer to zero. In case of the NW450 fabric the orientation of the main permeability axis (1-direction) is in 90° to the textile direction. This could be related to the distribution of the orientation of the fibers in the material, which results from the cross-lapping and process settings during the production of the non-woven textile. The preferential fiber direction in roll axis (90° direction) is mentioned in the technical data sheet but without any further details [125]. A higher fiber orientation in 90° leads to a porous structure with higher proportion of flow channels in this direction, thus a smaller resistance for the fluid flow. The permeability study on two flax fiber non-woven fabrics with different fiber orientation distribution from Xue *et al* [139] supports this observation. Their results show that for the anisotropic fabric type the preferential flow direction follows the principal fiber orientation. Furthermore, the test results in the present work indicate that this effect become more effective for higher compaction states since the anisotropy factor shows a decreasing trend with lower porosity contents, respectively higher fiber volume contents.

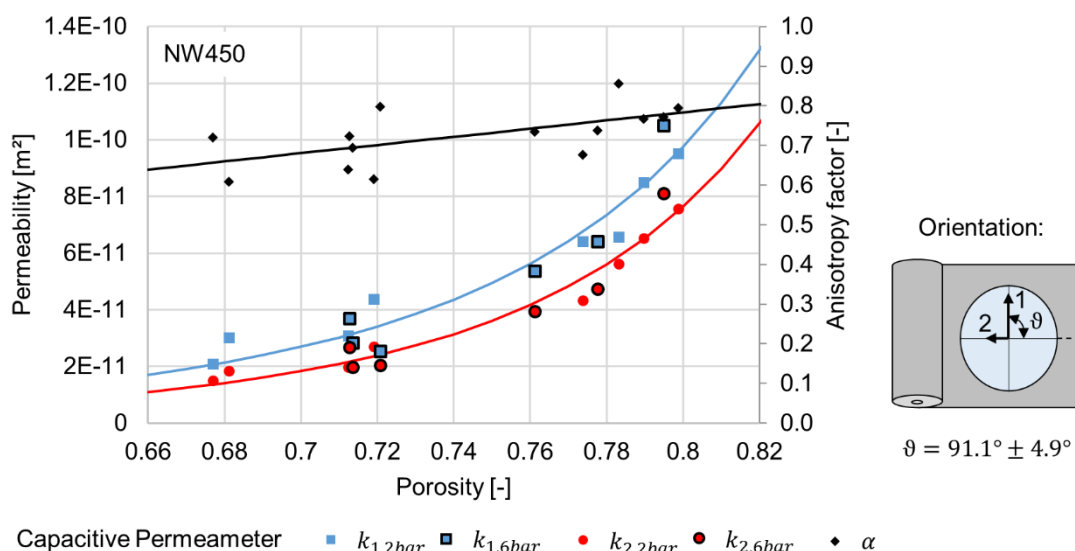


Figure 30: In-plane permeability characteristics of the NW450 fabric

The anisotropic characteristic of the woven fabric W400 is in between the unidirectional and the non-woven textile architecture within a range between 0.51 and 0.55, which can be seen from Figure 31. The main principal direction is close to 90° which corresponds to the differences related to the weave densities in warp and weft direction of the fabric, as presented in chapter 3.1. The smaller yarn density in weft direction (weft: 6.7 cm⁻¹ vs. warp: 8.7 cm⁻¹) offers wider macroscopic pore channels and therefore a more pronounced fluid flow in the 90° direction. This contrasts with the effect observed for the non-woven fabric, where the porous morphology is defined on fiber level. As mentioned before a higher fiber distribution in one direction causes a pronounced flow on micro level inside the non-woven material, while the lower fiber/yarn proportion in the woven textile leads to larger flow channels on macro level which defines in this case the preferential flow direction. The relationship between the main flow direction and the deviations from the balanced fabric construction was also present in the study on sheared woven flax fiber textiles from Liotier *et al* [140], but also for woven glass fiber textiles, which can be seen from the permeability benchmark study from May *et al* [70]. The sensitivity of the permeability characteristics on the actual yarn or roving architecture inside the fabric illustrates the importance of accurate and efficient permeability measurements.

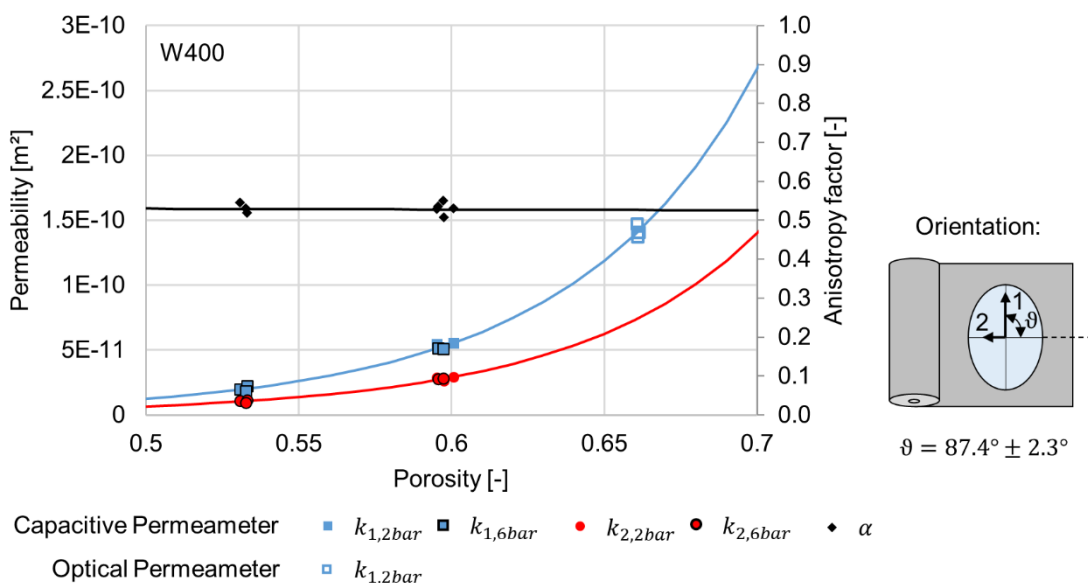


Figure 31: In-plane permeability characteristics of the W400 fabric

Considering the pore morphology inside the UD300 fabric, which is defined by the parallel and unidirectional yarn orientation, the pronounced fluid flow in the 0° direction meets the expectations. The resulting flow channels between the yarns along their orientation lead to a strong interaction between the actual porosity content and the resulting permeability. This can be seen from the fast increase of the k_1 permeability with increasing porosity in Figure 32.

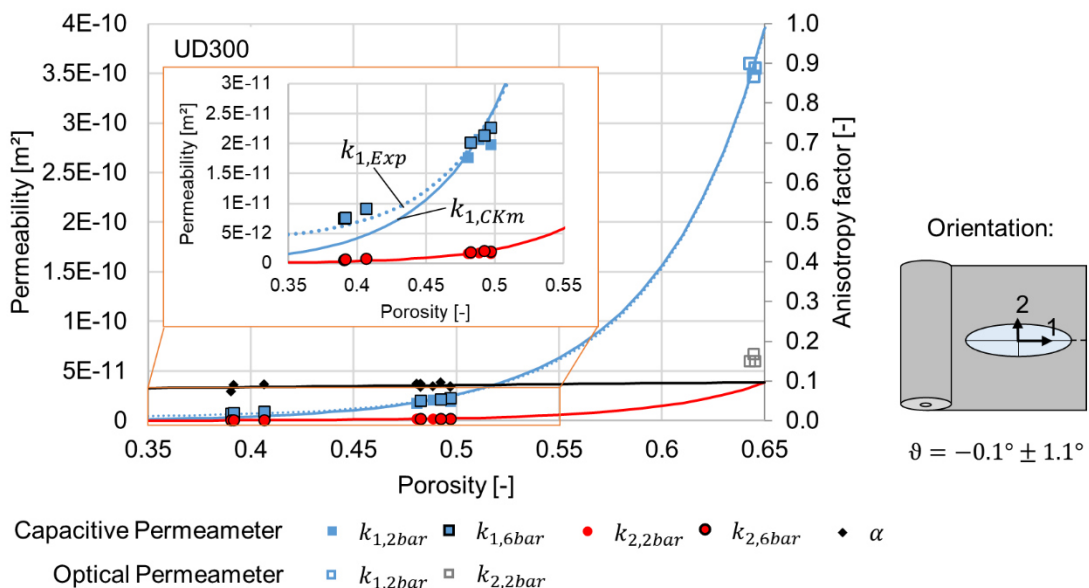


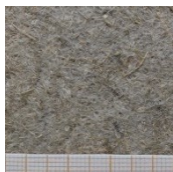


Figure 32: In-plane permeability characteristics of the UD300 fabric

Regarding the included variations of the injection pressure there are no significant influences on the permeability values detectable. This is in accordance with the results of previous studies for the permeability characterization [73], [141]. But in contrast to the present observations there are also studies that showed a significant dependence between fluid pressure and resulting permeability which is justified due the neglect of capillary pressures [142], [143]. This indicates that the influence of capillary forces on the permeability results strongly depends on the actual test conditions. Therefore, the influence of capillary forces on the permeability determination is discussed in the course of the investigations of the capillary action in chapter 5.4.2.

The modeling of the permeability characteristics was done based on the modified Carman-Kozeny model (Eq. (13)) presented in chapter 2.2.2. The corresponding function was applied to the measured k_1 values. For the UD300 fabric the

exponential model approach was considered, too, since this three-parameter approach (Eq. (14)) showed a higher accuracy in the lower porosity range, as can be seen in Figure 32. In case of the W400 and UD300 fabric the principal permeabilities in 1-direction from the test series on the optical test stand were included, while the corresponding k_2 values remained unconsidered due to the uncertainties based on the before-mentioned mold deflection. The resulting anisotropy characteristics from the test series at the capacitive test stand were used for a complete description of the in-plane permeability. The corresponding values for the anisotropic factor α were fitted using a straight-line function. While the NW450 textile shows the beforementioned dependence on the compaction state, an almost constant anisotropy factor was assumed for the W400 and the UD300 within the considered porosity range and based on the capacitive results. The permeability in the minor principal direction k_2 is then defined by k_1 and α according to Eq. (9). The resulting model parameters are listed in Table 9.

Table 9: Resulting model parameters for the in-plane permeability characterization

		NW450	Fabric type W400	UD300
				
Mod. Carman-Kozeny equation:	N	2.139	3.224	3.976
	C	$159.5 \cdot 10^9$	$40.37 \cdot 10^9$	$19.25 \cdot 10^9$
$k_{1,CKm}[m^2] = \frac{\phi^{N+1}}{C \cdot (1 - \phi)^N}$				c_1 $3.511 \cdot 10^{-3}$
Exponential model equation:				c_2 $1.608 \cdot 10^{-6}$
$k_{1,Exp}[m^2] = c_1 \cdot \exp(\phi \cdot c_2) + c_3$				c_3 19.07
Straight line fit:	A	1.03	-0.02	0.05
$\alpha = A \cdot \phi + B$	B	-0.0406	0.5396	0.0644

The following comparison clearly demonstrates the dependencies of the reinforcing architecture on the resulting permeability. Figure 33 depicts the evaluated major and minor principal permeabilities for the three fabric types, respectively. The analysis of the porosity contents which corresponds to a certain permeability (in this example:

$k = 4 \cdot 10^{-11} \text{ m}^2$), reveals the differences between the yarn-based fabrics UD300 and W400 on the one hand and the random fiber non-woven textile NW450 on the other hand. The necessary fiber volume fraction, which corresponds to the regarded permeability, is significantly lower for the non-woven fabric, due to the evenly distributed smaller pore spaces in the material, compared to the macro channels in the yarn-based textiles. This demonstrates how macroscopic pore spaces reduce the resistance against the fluid flow inside the woven and unidirectional architectures, respectively. It also highlights the dual scale pore size character in those fabrics, since the remaining volume which is not occupied by macro pores consists of the fiber volume with micro pores in between. The investigation of the acting mechanisms and the analytical description of the saturation process in such dual scale porous reinforcements has been subjected in various studies [118], [119], [144]–[147]. Motivation for this research is the improvement of the prediction accuracy for filling simulations and the avoidance of flow-induced voids and dry spots during the impregnation, which enhances the reliability for the LCM processes and the resulting quality of the composite part.

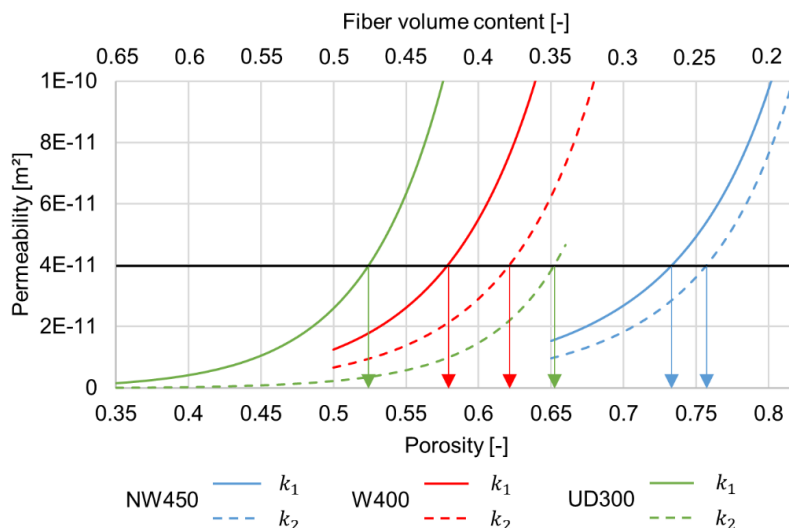


Figure 33: Comparison of the textile dependent in-plane permeability

In the following chapter, the capillary mechanisms that take place during the impregnation are investigated based on capillary rise experiments. Existing studies show the potential for the improvement of the resin injection process by defining an optimal impregnation velocity which based on the capillary properties of the textile reinforcement [110], [119], [121], [148].

5 Investigations on the capillary action

This chapter covers the analysis of the spontaneous imbibition of fluids into a textile reinforcement due to capillary forces. The aim is to gain an enhanced understanding of the impregnation mechanisms in fabric structures, which is subsequently used to optimize the LCM process. Figure 34 schematically depicts this approach which can be classified besides further applicable techniques to characterize the liquid and solid constituents and its interactions on the one hand, and the permeability properties of the textile reinforcement on the other hand. The former is exemplarily represented by a force tensiometer for measuring the wettability of single fibers, as used in previous studies [27], [149]–[151], but also covers the viscosity determination and alternative approaches for the analysis of interfacial properties. The measurement of the permeability characteristics, as presented in the previous chapter, considers the properties of the textile architecture and describes the resistance against the pressure driven fluid flow inside the porous material.

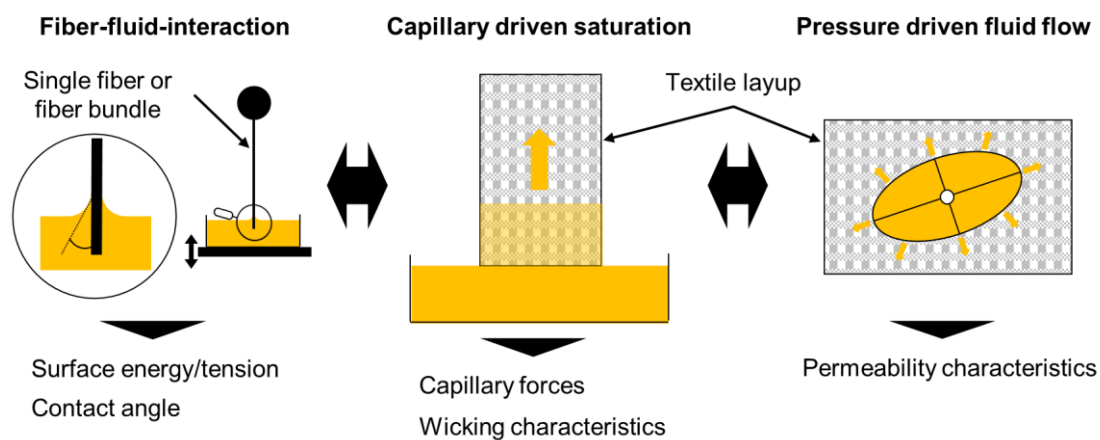


Figure 34: Schematic classification of the capillary analysis besides other characterization approaches related to the saturation of fibrous materials

The capillary analysis in the present work also takes place on textile level to represent a geometric state similar to the real LCM process. As a complement to the permeability characterization the investigations focus on the saturation effects right next to the fluid flow front. The experimental approach for the test series, the evaluation and model applications are presented in the following. The intended aim is the appropriate consideration of the capillary saturation for a model-based

description, as well as the analysis how to utilize the characterization results for the improvement of the impregnation in LCM processes.

5.1 Experimental setup

In Figure 35 the main components inside the experimental chamber of the capillary rise test stand are depicted. The textile sample is inserted and compacted to a predefined height inside the sample holder. This component complies with a plane rectangular cavity with an open edge on the bottom side. To run the experiment, a container filled with test fluid is moved vertically by a motorized z-stage (8MVT100-25-1 from Standa Ltd., Lithuania) which brings the fluid in contact with the open edge of the textile sample. From the moment of contact the imbibition of the test fluid inside the porous structure of the fibrous reinforcement progresses.

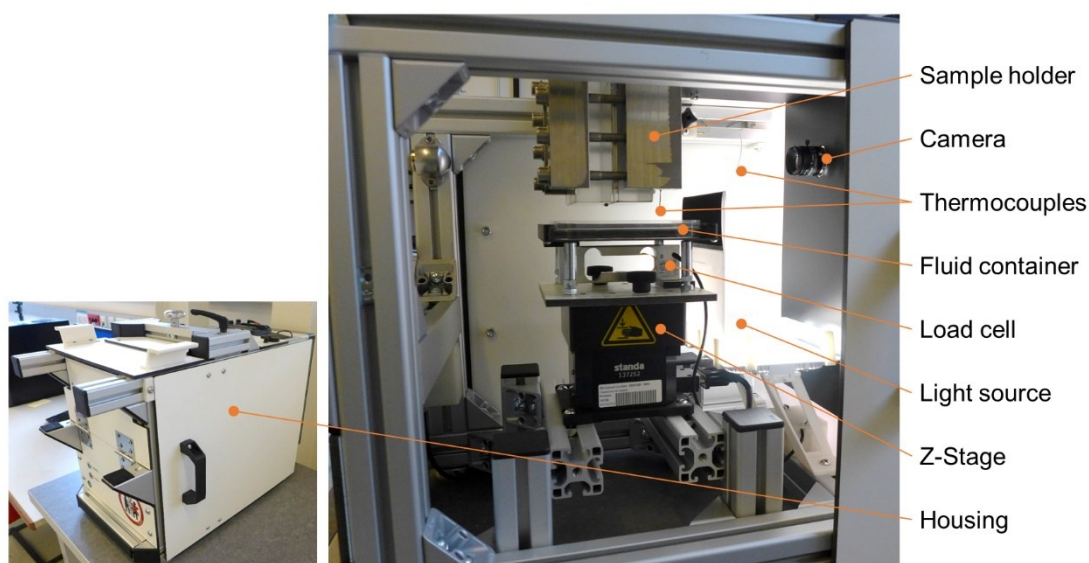


Figure 35: Components in the experimental chamber of the capillary rise test stand

The capillary rise and the change of the fluid weight is recorded by sequential image acquisition using an area scan monochrome camera (Genie™ Nano-M1920 from Teledyne Dalsa Inc, Canada, Camera lens: Tamron M112FM16), and by recording the data of a platform load cell (Model 1004 from Soemer Messtechnik GmbH, Germany / Accuracy class: C3 / Nominal load: 300 g). A diffuse light source and the housing of the test rig provides stable and proper light conditions during the test

duration. The room and fluid temperature are measured using type K thermocouples in combination with a temperature data logger (Pico USB TC-08, Pico Technology Ltd., United Kingdom). The test stand control is done by an application software programmed in Matlab® (MathWorks Inc., MA, USA), which allows the definition of experiment settings and the hardware control. Matlab® is also used as the software environment for the data evaluation afterwards.

5.1.1 Camera image and Load-cell calibration

The camera sensor (Sony Pregius IMX249 2.3M) provides an active resolution of 1920 x 1200 px, which is used to monitor an observation field of approximately 100 mm x 70 mm. For the calculation of distances from the image data, the pixel to length ratio $R_{px/l}$ was defined based on calibration tests using a checkerboard calibration pattern with a defined grid size, as it is depicted in Figure 36 a).

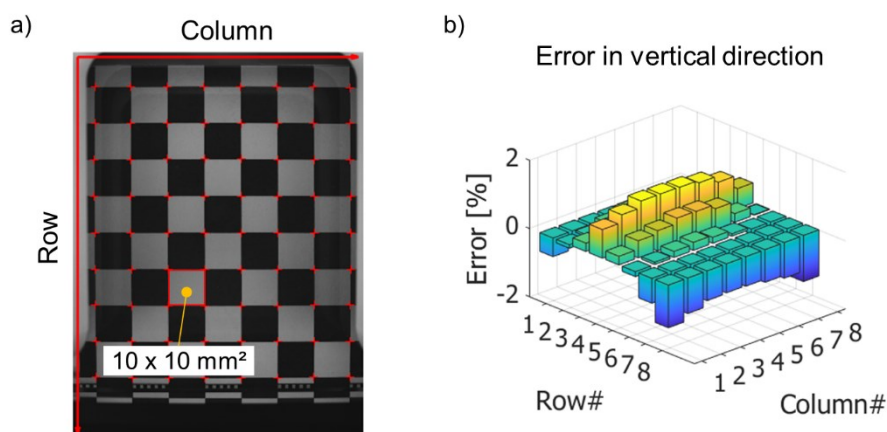


Figure 36: a) Camera image with calibration pattern to evaluate the pixel to length ratio, b) Error analysis for the distance measurements

Based on the detected intersection points across the pattern the derived mean $R_{px/l}$ value is 15.02 px/mm, which corresponds to an image resolution of 66.6 $\mu\text{m}/\text{px}$. The evaluation of the errors resulting from point-to-point measurements of the calibration pattern in vertical direction with a spacing of 10 mm is shown in the bar chart of Figure 36 b). The results reveal a slight barrel distortion, where the real distance is underestimated in the corners and overestimated in the middle of the image. The maximum error is smaller $\pm 1.5\%$ which corresponds to $\pm 150 \mu\text{m}$ for a 10 mm linear

measure. Considering that i) the error is in the magnitude of the measurement resolution and ii) the scatter of the measurements in the experiment is predictably higher than the error, the accuracy of the present accuracy is reasonable and meets the requirements for the present purpose.

The load cell signal was recorded using a load cell amplifier based on the A/D converter HX711 IC in combination with an Arduino® Uno R3 board (Arduino AG, Switzerland). The calibration was done using 50 g, 100 g and 200 g calibration weights (OIML class E2 from Kern & Sohn GmbH, Germany) to define the linear relationship between the load cell output and the physical weight in a range between 0 g and 250 g.

5.1.2 Test fluid properties

Particular attention was put on the selection of the test fluids used for the capillary experiments. The objective is the usage of fluids which ensure proper and accurate input data for the evaluation and the subsequent model derivation. One possibly critical parameter is the contact angle θ between the fluid and the fiber surfaces. A common approach to minimize unfavorable effects due to the complex mechanisms related to the contact angle is to ensure a full wetting interface between the fluid and fiber surface. A widely accepted and used definition of surface energy and theory to describe the interaction of fluids on a solid surface was presented from Fox and Zisman [41], [152]. In this theory there is a linear relationship between the surface tension of a liquid γ and the cosine of the contact angle θ on (low energy) solid surfaces. Based on their observations a critical surface tension exists which defines the limit for a full-wetting characteristic with a contact angle of 0° . This relationship is depicted in Figure 37. The Zisman method is very accurate and most suitable in case of non-polar surfaces in combination with non-polar liquids (e.g. the homologous group of n-Alkanes). But in the presence of polar proportions in the surface tension the method shows inaccuracies and higher scatter, since differences in the interactions between the fluid and the solid surface, based on their polar and dispersive character, are not considered [153]. The separation of polar and dispersive interactions was taken into account e.g. in the well regarded

approaches from Owens and Wendt [42] or Wu [43]. Nevertheless, Zisman's theory is considered to be suitable for the selection of test fluids in the present case meeting the criterium of a full wetting of flax fibers.

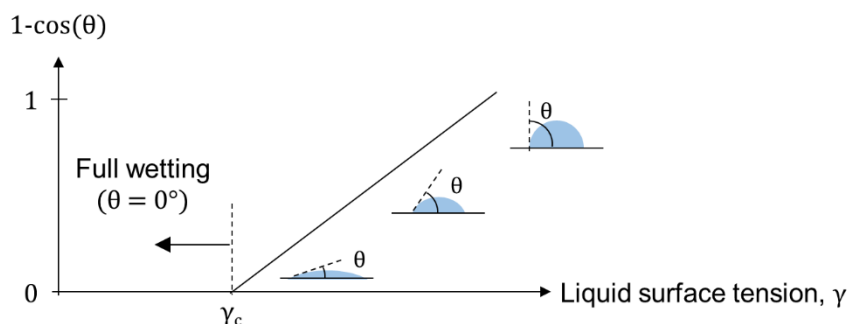


Figure 37: Zisman plot for describing the relationship between the liquid surface tension and the static contact angle on a solid surface

Measurements of the critical surface tension of liquids for a full wetting of flax fiber surfaces were done by van Hazendonk *et al.* [26]. In this study they considered the dependence of polar and completely non-polar fluids by using water-methanol mixtures and 1-methylnaphthalene - octane mixtures, respectively. The measurements on dew retted flax fibers revealed a critical surface tension of 23.7 mN/m and 27.8 mN/m for the polar and non-polar fluid, respectively. For warm-water retted flax fibers the surface tensions were 26.2 mN/m (polar fluid) and 31.3 mN/m (non-polar fluid). Subsequent extraction methods to remove low energy constituents like fats and waxes, pectines and hemicelluloses led to a further increase of the critical liquid surface tension, which correlates with the expected tendency, as presented in chapter 2.1.

The differences depending on the polar character of the fluid confirm the presence of interactions between the fluid and the solid constituent which are not considered in Zisman's approach. However, the empirical results from literature are suitable to define an upper limit for the surface tension of liquids that correlate with a full wetting of flax fibers, by considering the lowest values from the literature data.

Table 10 shows the surface tension characteristics of the three test fluids selected for the present investigations, which are:

- n-Decane (for synthesis, 99% from Carl Roth GmbH & Co. KG, Germany)

- 2-Propanol (technical grade, 99.7% from Otto Fischar GmbH & Co. KG, Germany)

and

- Polydimethylsiloxane fluid (Xiameter® PMX-200 Silicone Fluid from Dow Corning Inc., MI, USA)

Table 10: Test fluids and their surface tension components at room temperature

Fluid	Surface tension [mN/m]			Polarity $x^p = \gamma^p / \gamma$	Source
	Polar γ^p	Dispersive γ^d	Total γ		
n-Decane (DEC)	0	23.8	23.8	0	[153]
2-Propanol (IPA)	3.5	19.5	23.0	0.15	[154]
Polydimethylsiloxane (PDMS)	0.9	20.5	21.4	0.04	[155]

The test fluid with the highest fluid tension in this selection is n-Decane, a non-polar fluid from the group of n-Alkanes. The fluid with the highest polarity is 2-Propanol, which is due to its electronegative hydroxyl group, but also with a lower total surface tension than n-Decane. The Polydimethylsiloxane silicone oil was chosen due to its low surface tension but a comparably high viscosity which enhances the bandwidth of fluid penetrativities considered in this work. All three test fluids meet the criterium for a full wetting of flax fibers with respect to the critical surface tensions and polarity characteristics from literature.

To ensure accurate input values for the relevant fluid properties, the temperature dependent behavior of the dynamic viscosity, the surface tension and the density are considered. For 2-Propanol and n-Decane values were taken from pertinent literature [156], material data bank [157] and published data [158], [159]. Appropriate regression curves were fitted based on polynomial functions. In case of the Silicone fluid (PDMS) the dynamic viscosity was determined via rheometer (MCR 302 from Anton Paar GmbH, Austria) using a cone-plate measurement system (CP25-1-SN25340). The surface tension and density values at 25°C were taken from the technical data sheet [160]. A linear temperature dependence for the surface tension was considered based on the results on silicone oil from Dai *et al.*

[161], while the density was used as a constant within the temperature range during the tests series.

The temperature dependent properties of the test fluids are depicted in diagrams a), b) and c) of Figure 38. The corresponding regression functions can be found in appendix A.4. The experiments were conducted at room temperature since there is no option for temperature control inside the test stand. The measured fluid temperature was in a range between 24°C and 29°C throughout the test series.

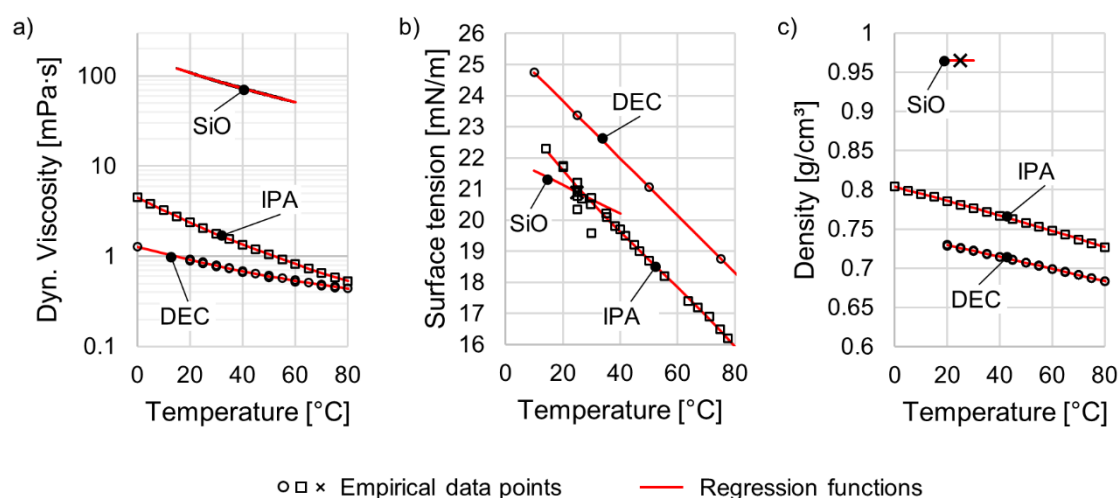


Figure 38: Test fluid properties over temperature: a) Dynamic viscosity, b) Surface tension, c) Density

A further criterion for the choice of appropriate test fluids considers the tendency of natural fibers for liquid absorption and swelling. This change of the fiber diameter directly influences the morphology of the porous space which is the driving factor for the capillary action inside the material. For a proper investigation of the capillary effects such interfering phenomena must be considered. Therefore, the interaction between single flax fibers and fluids (n-Decane, 2-Propanol and distilled water) was analyzed using an optical microscope with the associated measurement software. The flax fibers were fixed on top of a slide and covered with a cover slip. In the gap between the two glass plates a fluid drop was instilled which leads to the wetting of the fiber. After refocusing the microscope (approx. 30 seconds) the wet state of the fiber was captured. Figure 39 shows exemplary images of flax fibers in dry and wet state during the tests with n-Decane and distilled water with several width measurements along the fiber length.

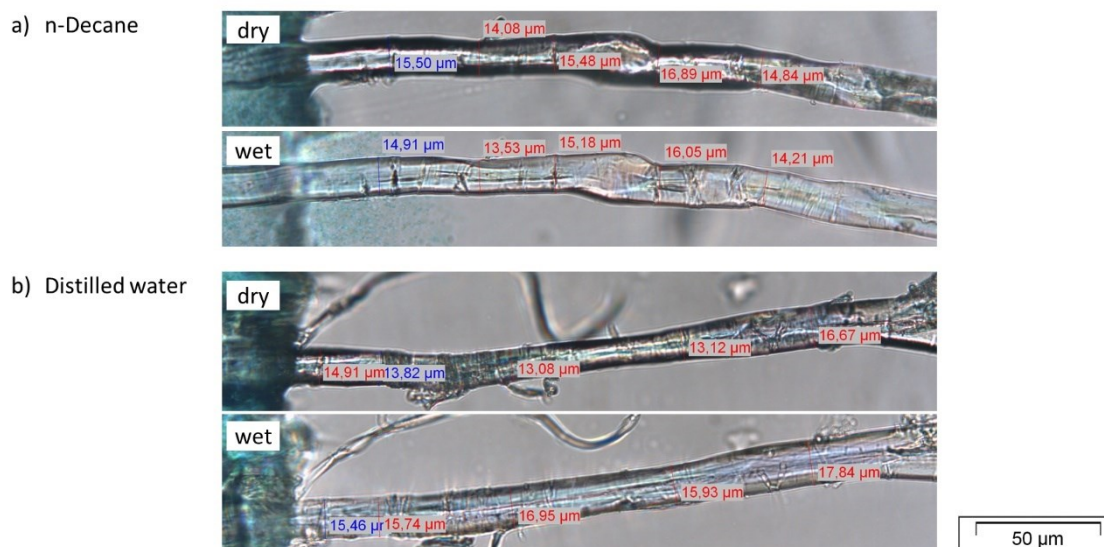


Figure 39: Microscopic analysis of the swelling behavior of flax fibers in contact with different fluids: a) n-Decane, b) Distilled water

Based on the measurements the swelling ratio R_{sw} was calculated as follows:

$$R_{sw} = \frac{D_{f,wet}}{D_{f,dry}} \quad (62)$$

Where $D_{f,dry}$ and $D_{f,wet}$ are the fiber diameters in the dry and wet state, respectively. The test series gives resulting R_{sw} values of 0.99 ± 0.02 for 2-Propanol, 0.98 ± 0.04 for n-Decane and 1.22 ± 0.07 for distilled water. The values close to one in case of n-Decane and 2-Propanol indicate that the interactions with the flax fiber does not lead to significant swelling effects compared to the strong increase of the fiber diameter when using distilled water. Therefore, water was not considered as an appropriate test fluid for the characterization of plant fiber reinforcements since this requires a detailed understanding in the dynamics of the fiber swelling effects. Nevertheless, the result with water is in good agreement with the findings from Pucci [162] who did similar studies on the swelling behavior of flax fibers using optical measurements. The reported mean swelling ratio of untreated flax fibers in water was 1.27 ± 0.13 , which confirms the own measurement approach. Polydimethylsiloxane fluid was not considered in this test series, but due to its non-polar surface characteristics and the high viscosity, which impedes the absorption by the flax fiber, a strong swelling effect is not to be expected.

5.1.3 Experiment procedure and Test configurations

The preparation of the material samples starts with the cutting of the textile layers with defined size and orientation using a Zünd G3 cutter (Zünd Systemtechnik AG, Switzerland). The chosen standard width and length of the cuttings are 60mm x 65mm. Dependent on the test configuration the intended number of textile layers is stacked and weighed using a precision scale (Kern KB360 from Kern & Sohn GmbH, Germany). Subsequently, the stacked sample is placed in the sample holder between two 30 mm thick glass blocks with the bottom side flush to the open cavity edge, as depicted in Figure 40. Via screw clamping the specimen is compacted to the intended thickness which is defined by a metal distance frame between the glass blocks. For all experiments in this study the cavity height was kept constant using a cavity frame with a thickness dimension of 4 mm. The homogeneity of the cavity height between the glass blocks was analyzed using a two-component epoxy clay (Toolcraft Kaltmetall Stick from Conrad Electronics SE, Germany), which was placed and flattened on different positions inside the cavity. The resulting thicknesses of the cured epoxy platelets were measured using a micrometer screw which were in a narrow range between 3.96 mm and 3.98 mm. Considering the accuracy of this measurement approach and a possible shrinkage of the epoxy clay during cure it is therefore reasonable to calculate with a homogenous sample thickness of the intended 4 mm.

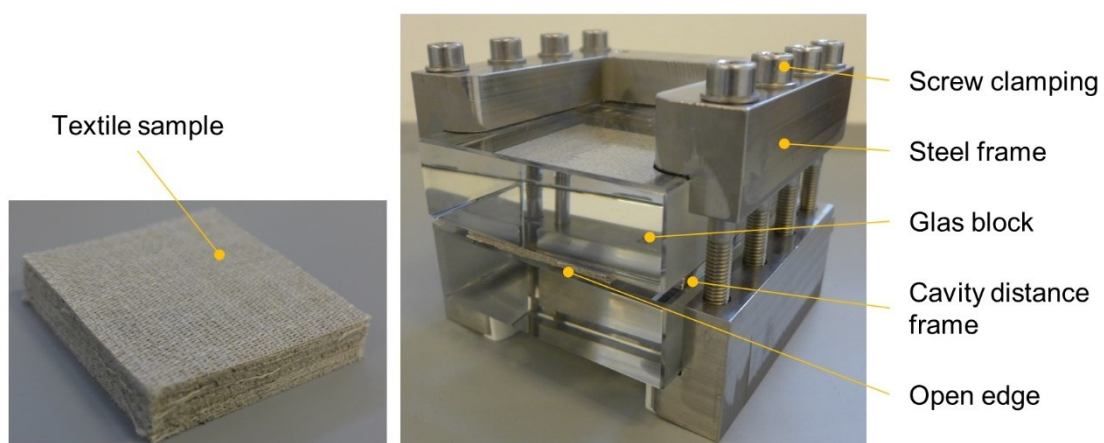


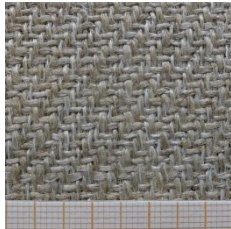
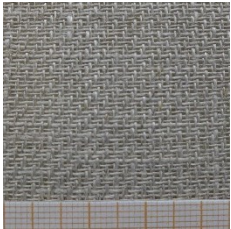
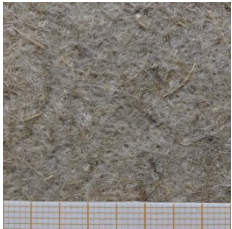

Figure 40: Components and assembly of the sample holder

With the prepared specimen setup, the experiment preparation concludes by filling the test fluid in the fluid container up to a defined level followed by the installation of

the sample holder inside the test stand. The settings for the image capture, the load cell and thermocouples are defined in the control program. At the start of the experiment, the initial fluid weight is measured followed by the command for the z-stage to move upwards to the intended position which leads to the immersion of the open cavity edge, thus to the imbibition of the test fluid inside the fibrous sample. The termination of the experiment moves the z-stage to its initial position and completes with an extended weight measurement to determine the total fluid mass change. During the experiment, the camera captures the first 200 images at a rate of 20 images per second to ensure a high measurement resolution in the first phase and continues with one image per second. The data acquisition of the load-cell is done with 80 Hz and the temperature of the fluid is recorded every four seconds.

An overview of the test configurations considered in this study is given in Table 11, which considers the selected flax fiber textiles, a variation of the number of layers, the textile orientation and different test fluids.

Table 11: Test configurations specified by fabric type, test fluid, textile orientation and number of layers

Fabric type			
W400	W200	NW300	UD300
			
DEC 0°: 5L / 6L / 7L 45°: 5L / 6L / 7L 90°: 5L / 6L / 7L	DEC 0°: 9L / 10L / 11L 45°: 9L / 10L / 11L	DEC 0°: 4L / 5L / 6L / 7L	DEC 0°: 8L / 10L / 12L
IPA 0°: 5L / 6L / 7L			
PDMS 0°: 5L / 6L / 7L			
EPOXY 0°: 5L / 6L			

The test series were planned with two intended priorities: i) the comparison of the properties of the different fabric types using n-Decane as common test fluid and ii) the analysis of the dependencies on the fluid and textile properties, respectively, using the test fluids presented above in combination with the W400 woven fabric.

5.2 Data evaluation

The following section points out different aspects for the evaluation of the acquired data. The two main data evaluation tasks relate to i) the detection of the fluid height during the capillary rise and ii) the evaluation of the imbibed fluid mass. The diagram in Figure 41 shows an exemplary output for the recorded weight progression and the capillary rise, respectively.

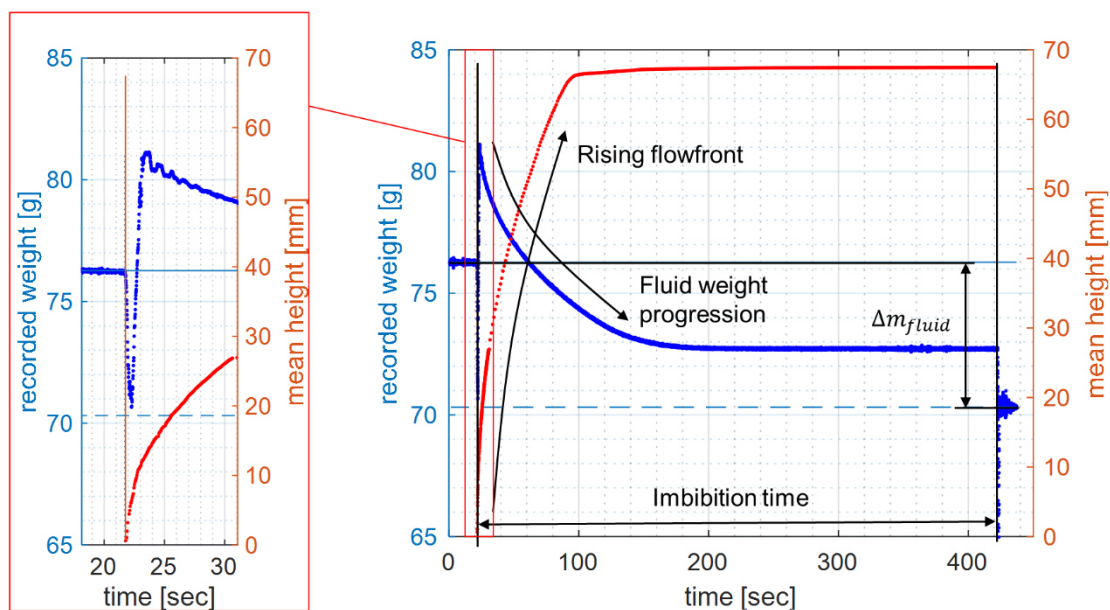


Figure 41: Overview of fluid weight data and the detected fluid height during an imbibition experiment

The enlarged detail section depicts the starting point of the fluid imbibition. At this point the recorded weight shows a sudden drop, which is due to the wetting of the glass block bottom sides and the fast wicking inside the porous spaces of the specimen while the z-stage is still moving upwards. The immersion of the glass blocks leads to a rise of the weight progression due to buoyancy forces until the end position is reached. Subsequently, the continuing fluid imbibition goes along with a

decreasing weight progression until a steady state is reached. At the end of the experiment the z-stage moves downwards to its initial position. The weight difference between the start and the end value gives a measure of the total fluid weight imbibed into the textile sample. Practically, the mean total weight based on two determined values: the mentioned load cell result and additionally the measured weight difference of the dry and the saturated specimen on a precision scale. This is intended to compensate the error due to remaining residues of fluid on the glass block surfaces. The capillary fluid rise shows from the imbibition start a degressive progression in height over time until the upper edge of the specimen is reached as can be seen in Figure 41.

5.2.1 Fluid height detection

The digital image processing for the flow front detection during the capillary rise, based on the evaluation of greyscale values using difference images from a reference image (complete dry specimen) and the actual state (partly to fully saturated specimen). The wetting of the fiber leads to a decrease of the relative refractive index compared to its dry state and increases the probability of total light reflection inside the surrounding fluid layer which decreases the albedo of the fiber surface. Therefore, wet fibers appear darker than in dry state [163]. By utilizing this change in brightness and by defining a suitable threshold value which defines the separation of the dry and the wet state, the progression of the fluid inside the textile reinforcement is determined. The image in Figure 42 shows a partly saturated sample at a certain time during the capillary experiment. The red dots mark the point of each pixel column which corresponds to the detected fluid flow front. Considering the scatter, several approaches can be applied to define the actual representative height, like a minimum or maximum criterion the mean value or, as used in this work, based on the empirical cumulative density function (ECDF). The reason for this decision is discussed in the following.

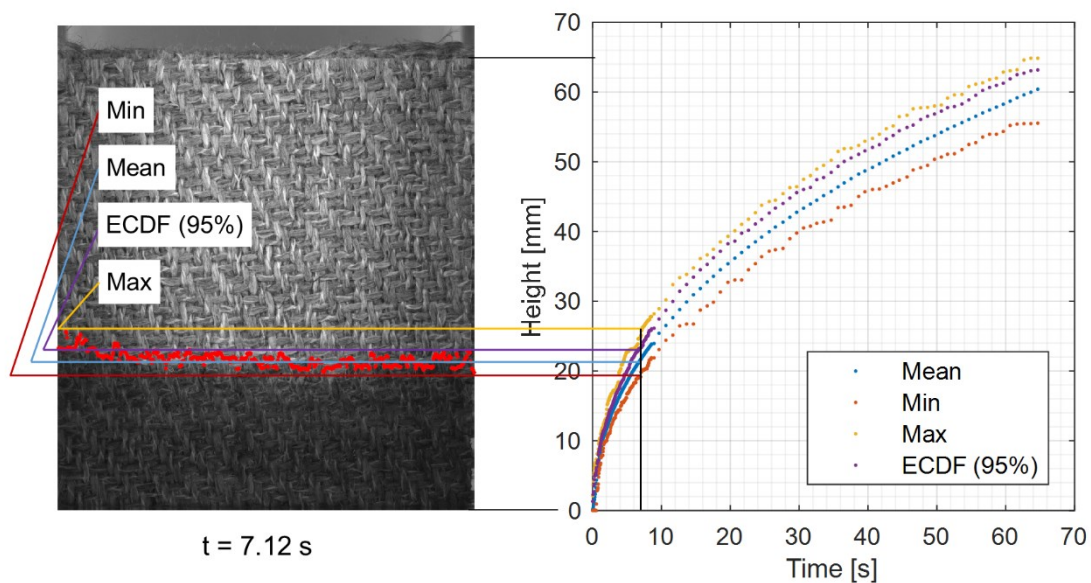


Figure 42: Detection of the fluid height with different approaches for the height definition

During the experimental series two effects were recognized and considered for the image based capillary rise detection. In Figure 43 a) two partly saturated samples of the woven (W400) and the unidirectional fabric (UD300) are depicted which show the tendency for a faster ascend velocity near the left and right edges of both specimens. This can be explained by a lower degree of compaction in these areas due to the free textile edges. This results in areas with wider pore spaces in which the fluid rises faster. For the unidirectional fabric (UD300) this effect is most pronounced due to the relatively loose yarns at both sides which leads to larger capillary channels than in the representative middle region of the specimen. This effect is considered for the flow front detection by defining an appropriate width of the image section in which the flow front moves equally. For the experiments with the unidirectional fabric the width was set to 10 mm and to 30 mm for all other fabrics (woven and non-woven).

Figure 43 b) points out another aspect on a closer level. Especially in case of the woven fabrics it can be observed that the wetting of yarns perpendicular to the flow direction occurs with a lag. The actual progression of the flow front is in this situation hidden by the visible and dry cross yarn areas. Therefore, the ECDF function is used to determine the actual fluid height at the upper end of the visible flow front data distribution. A level of 95% as predefined limit of the cumulative distribution was

found to be suitable to effectively neglect any outliers above which provides the reliability for the tracking algorithm.

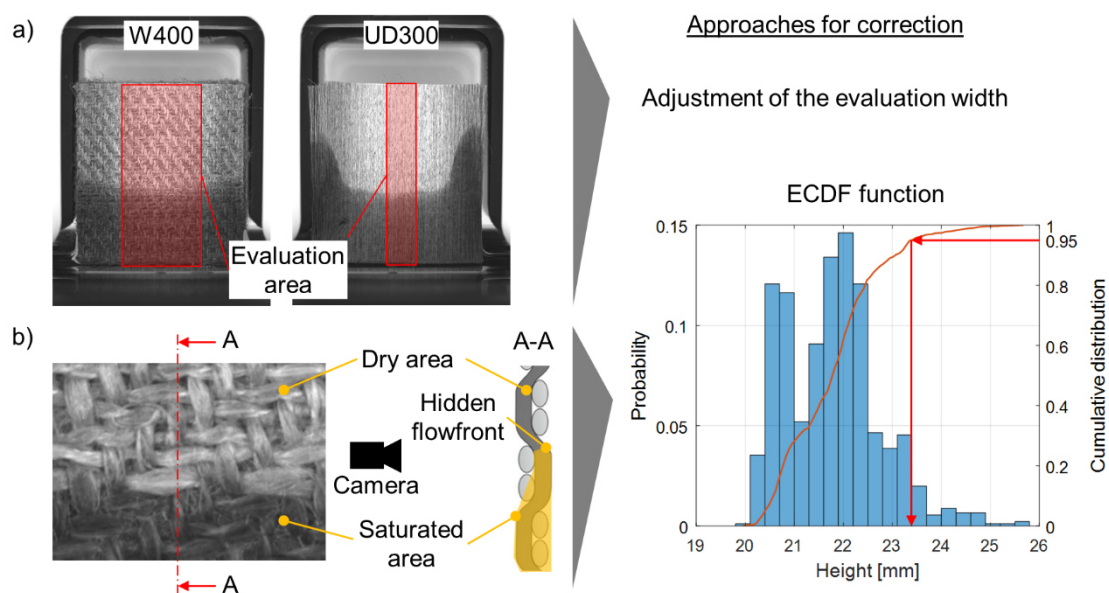


Figure 43: Consideration of different effects for the fluid height detection: a) Faster fluid velocities at the sample edges, b) Hidden flow front due to a delayed saturation of the cross yarns

5.2.2 Fluid mass intake

The fluid mass which imbibes into the porous structure of the fibrous specimen is calculated based on the recorded weight, as it is depicted in Figure 41. In this step the decreasing buoyancy force of the immersed glass blocks due to the falling fluid level in the fluid container is considered. A measurable evaporation rate, which leads to a continuous weight reduction, was detectable only for 2-Propanol which was evaluated in initial experiments to 0.094 ± 0.004 g/min.

In the following, the progressions of the fluid mass intake are compared with the optical detection of the capillary rise. The diagram in Figure 44 shows both curves exemplarily for the woven W400 textile with varying specimen heights of 35, 50 and 65 mm, respectively. It can be observed that the fluid imbibition continues after the fluid reaches the upper specimen edge until a steady value is reached.

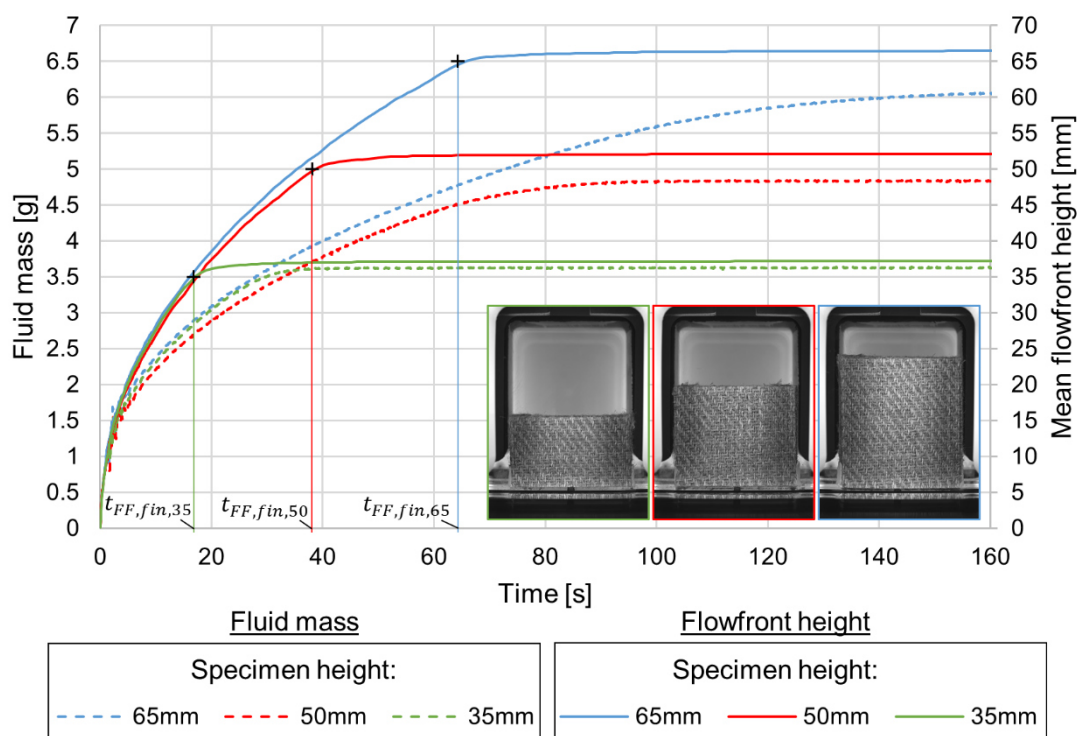


Figure 44: Progressions of the fluid height and the imbibed fluid mass over time for different specimen heights

The observation of a continuing fluid flow is present for all tested fabric types and fluids during the capillary test. An overview is given by the diagram in Figure 45 which shows the remaining porosity contents inside the specimens at the time when the visible flow front reaches the upper sample edge and at the final state of the experiment, respectively. The differences between both states indicate that a significant amount of fluid flow takes places behind the visible flow front. The smallest changes can be found for the UD300 fabric with the lowest preform porosity of ca. 45%, thus highest fiber volume content. With decreasing fiber volume content, the saturation effects behind the flow front increase. The woven fabrics W400 and W200 show similar contents of remaining porosities when the flow front reaches the upper edge. The subsequent saturation after that point is higher in case of the W400 textile, which is indicated by a larger porosity shift until the final state is reached. Interestingly, the non-woven fiber mat NW300 show a similar behavior as the yarn-based textiles. This indicates that even without a pronounced dual scale fiber architecture, the present distribution of pore sizes between the fibers leads to an unevenness of the capillary driven saturation.

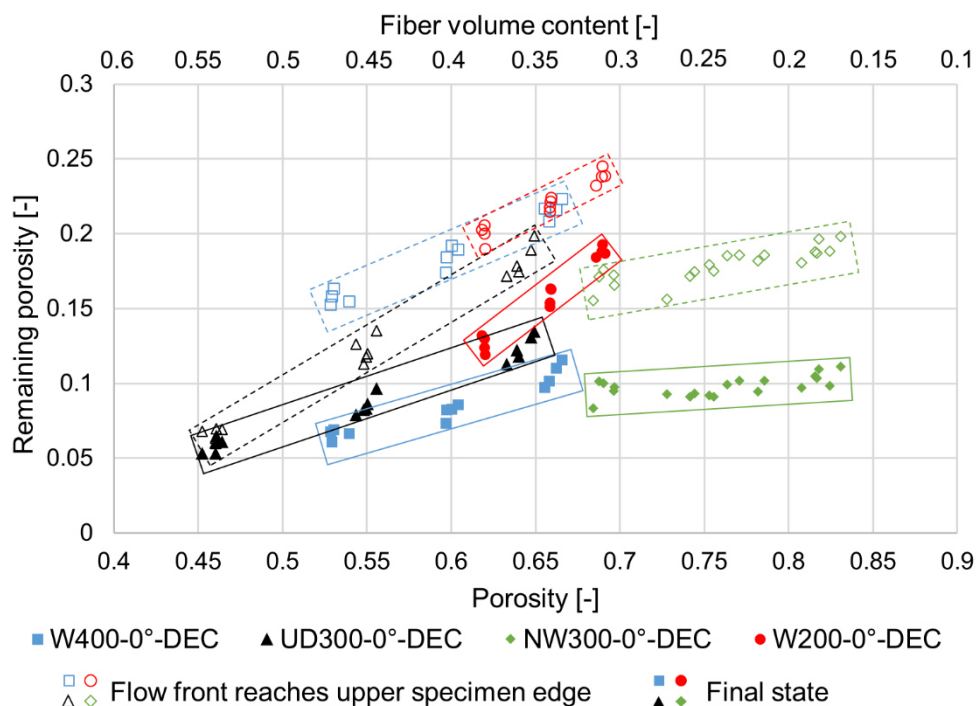


Figure 45: Remaining porosity contents inside the textile samples when the flow front reached the upper specimen edge and at the final saturation state

The results give insights how the interconnected network of porous spaces in fibrous reinforcements are filled by capillary action. Behind the primary visible flow front a peripheral fluid flow takes place which fills remaining pore spaces in partly saturated areas. For woven fabrics, the textile architecture defined by the warp and weft yarn system may lead to such a fluid flow behavior since the delayed saturation of the cross yarns was already pointed out in the previous section (see Figure 43). The evaluations for the non-woven fabric as well as for the UD fabric indicate that similar phenomena also take place without two intersecting yarn systems. The unidirectional UD300 fabric at high fiber volume fractions shows the most even capillary rise, probably due to the tightly packed parallel fibers with resulting pore channels of similar size and aligned in vertical orientation. In this condition the preform does not offer a significant amount of peripheral spaces which are filled with a pronounced lag.

5.2.3 Application of the Capillary rise model

In the following section, the model equations for the dynamic capillary flow, as introduced in chapter 2.2.3, are analyzed. Due to the observable deviations between the measurements and the capillary rise predicted by the Lucas-Washburn (L-W) model, the approach was modified by considering a peripheral fluid flow behind the visible flow front. This is done by the application of a permeable capillary tube wall which allows the fluid to pass. The aim is to find an accurate model approach which is capable to characterize the capillary action equally for different types of fiber reinforcements.

Deviations from the Lucas-Washburn equation

The application of the classical L-W model generally makes use of a linear relationship between the squared capillary rise h^2 and the time t . Since the capillary radius r_c is assumed to be constant as well as the fluid properties (dynamic viscosity η , surface tension γ and contact angle θ), the L-W equation can be written as:

$$h^2 = m_{LW} \cdot t \quad \text{with} \quad m_{LW} = \frac{\gamma \cos(\theta)}{2 \eta} \cdot r_c \quad (63)$$

where m_{LW} represents the slope of the linear h^2 - t progression. The application of the corresponding regression line to the empirical data is depicted in Figure 46 a) exemplarily for the W400 fabric with n-Decane and three different fiber volume contents. This simple approach seems to describe the capillary action inside the fibrous reinforcement fairly good in the first instance, which justifies the application of the L-W equation. But on closer examination, the differences between the measured capillary rise progression and the straight line shows significant deviations, especially during the initial phase of the wicking, which is depicted in the enlarged sections of Figure 46. It is also evident that the resulting value for m_{LW} depends on the range of the considered data points which is defined by the specimen height in the present case. The straight line fit with less data points would result in a steeper slope, due to the degressive h^2 - t curve progression, which is for the purpose of a material characterization obviously not ideal. The diagrams in Figure 46 b) show the corresponding h - t curves for comparison. It can be observed that the capillary rise inside the tested materials does not adequately fit to the

proposed square root function between the fluid height h and the imbibition time t . Similar deviations from the L-W approach were found by LeBel [118], [119] who studied the capillary flow inside a glass fiber NCF, and also by Masoodi *et al* [164], [165] and Fries [89] for further wicking scenarios inside porous media.

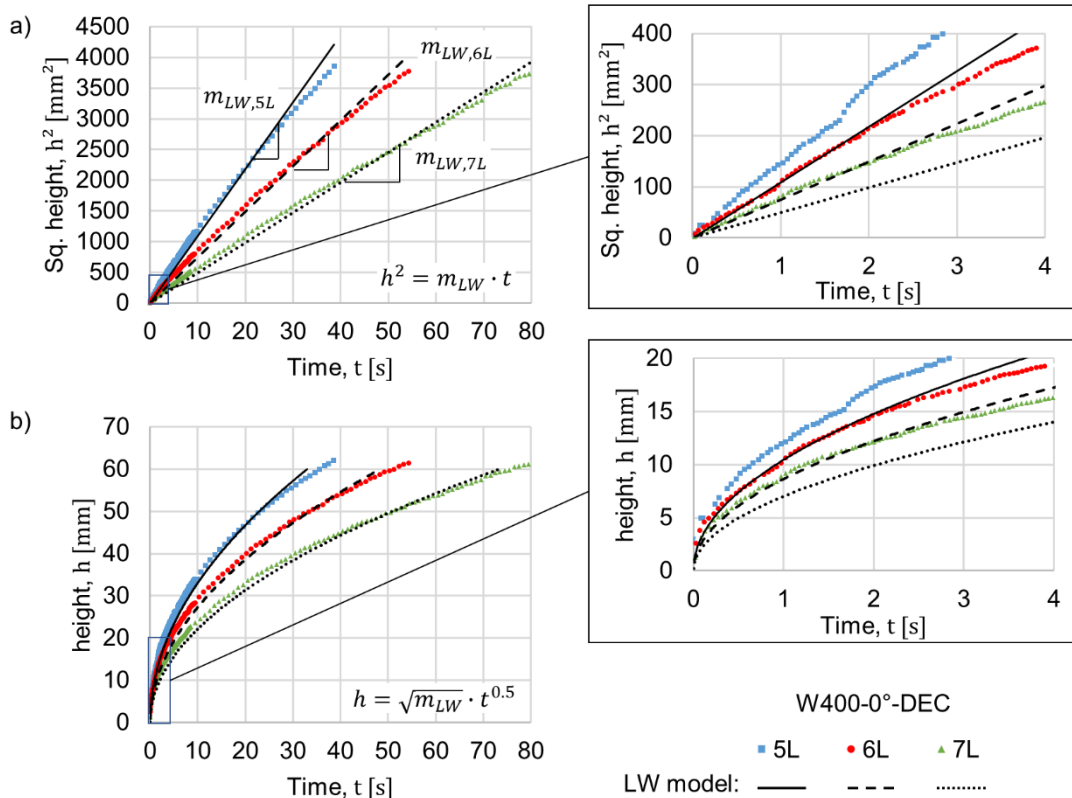


Figure 46: Application of the classical Lucas-Washburn model. a) Squared height over time and b) height over time capillary rise progression

To achieve a higher precision in the most relevant initial phase of the wicking experiment the L-W approach is therefore applied to a limited range at the start. It is assumed that within a defined initial section the capillary flow regime is represented by the L-W equation with good precision which deviates in the further course due to the influence of unconsidered flow mechanisms.

For the definition of the initial data range the following aspects were considered:

- i) The range should be as small as possible and as large as necessary to minimize the error due to the observed deviations from the L-W model.
- ii) The considered height should be of an extent capable to represent the general material properties. This is of particular importance for yarn

based, heterogeneous fibrous architectures like woven fabrics. Therefore, the considered range should be of an extent to contain a suitable number of unit cells of the fabric pattern.

- iii) The measured data tends to higher inaccuracy and scatter in the very start of the wicking, due to irregularities at the bottom edge of the textile stack and the time required to develop an even flow front progression after the first fluid contact. Regarding the given measurement resolution and accuracy, a stable progression should be reached to provide good reproducibility.
- iv) The definition should be valid for different fluids whose properties strongly affect the ascend velocity during wicking. Therefore, a height limit is seen to be more suitable than a time limit.

Regarding these points, the consideration of experiment data up to a capillary rise of 10 mm revealed to be appropriate to define the range for the application of the L-W approach for the present evaluation of the considered test series. As part of the data evaluation strategy the discrete data points were fitted using the potential function of the following form:

$$h = A \cdot t^B + C \quad (64)$$

where A, B and C are model parameters which are determined via curve regression.

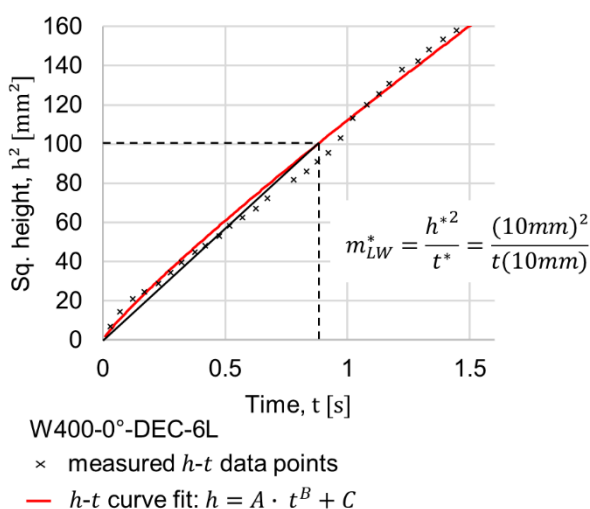


Figure 47: Approximation of the initial phase of capillary rise based on the Lucas-Washburn equation

The fit function in Eq. (64) is capable to represent accurately the measured $h-t$ data of all test configurations. Based on this continuous expression the L-W slope within the predefined range m_{LW}^* is then evaluated, as depicted in Figure 47.

According to Eq. (63) the value for the capillary radius is given as follows:

$$r_c = \frac{m_{LW}^* \cdot 2 \eta}{\gamma \cos(\theta)} \quad (65)$$

The capillary radius r_c is used as a material-specific parameter which characterizes the pore morphology of the fiber reinforcement. The further $h-t$ progression according to the L-W equation with the initial slope m_{LW}^* overestimates the measured capillary rise, as illustrated in Figure 48. This behavior meets the expectations regarding the deviations shown before. To examine the influence of gravitational forces, which were neglected so far, the capillary rise progression according to Eq. (29) is depicted in Figure 48, too. The still high deviations from the empirical data indicate that the disregarded gravity influence in the L-W equation is not the main reason for the observed discrepancies.

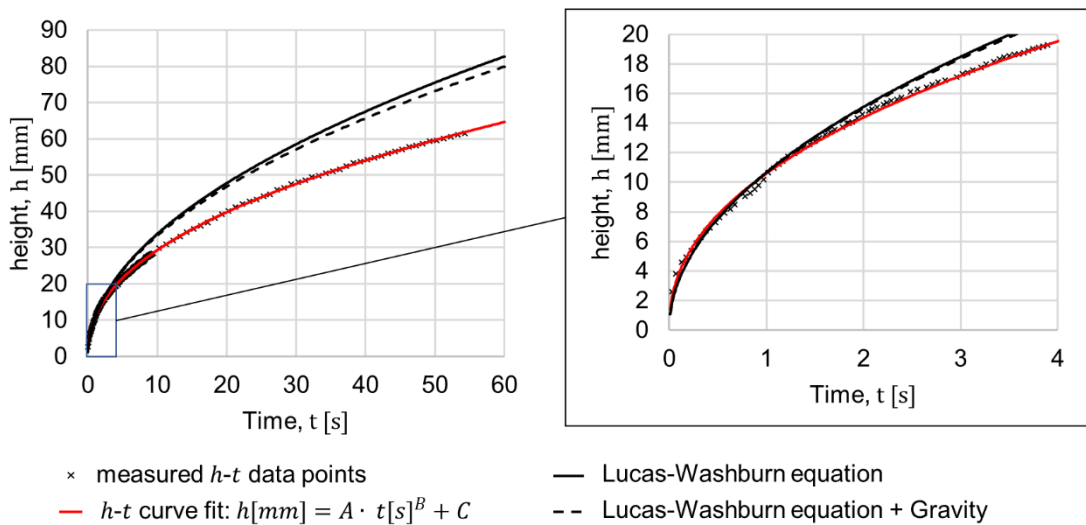


Figure 48: Comparison of the measured capillary height progression and the Lucas-Washburn model with and without consideration of gravity forces

Therefore, the porous tube approach, as derived in chapter 2.2.3, is applied, which additionally enables the consideration of a modeled fluid flow through the capillary wall. This is seen as an enhanced representation for the capillary actions inside the

irregular, interconnected pore structures of fibrous materials based on the experimental observations.

Application of the porous tube approach

The observation of an extended fluid flow behind the flow front and the deviations from the classical L-W model leads to the presented theoretical approach considering a porous capillary wall with a peripheral flow from the inside out. As illustrated in section 5.2.2, this peripheral flow correlates with a decrease of the ascend velocity which is measured using the visible flow front progression in vertical direction. The porous tube model is evaluated in the following based on the experimental results.

To analyze the peripheral fluid velocity v_w the rearrangement of Eq. (41) gives:

$$\begin{aligned} v_w(h) &= \frac{r_c^3}{8 \eta h^2} \left(\frac{2\gamma \cos(\theta)}{r_c} - \rho g h \right) - \frac{r_c}{h} u(h) \\ &= u_{LW}(h) - u_g - \frac{r_c}{h} u(h) \end{aligned} \quad (66)$$

with the ascend velocity of the fluid u over height h and the value for the capillary radius r_c which is evaluated using the L-W approach, as described in the previous section. The ascend velocity u is calculated based on the derivation of the used fit function of Eq. (64) which gives:

$$u = \frac{dh}{dt} = A \cdot B \cdot t^{B-1} \quad (67)$$

This allows the continuous calculation of v_w according to Eq. (66), which is depicted exemplarily for an experiment on the W400 fabric in Figure 49 a). The corresponding curve shows a fast increase with a maximum value at a height around 10 mm. Subsequently, v_w decreases continuously with progressive capillary rise. A detailed look at the initial phase under 10 mm reveals that the negative v_w values are due to the predefined L-W approach to assess the size of the capillary radius. Within this initial phase of the experiment the measured data, respectively the fitted potential function, correlate with a faster capillary rise than the L-W model prediction. This causes a theoretical peripheral fluid flow from the outside inwards the porous tube to fit the porous tube model with the measured data. Furthermore, it must be

considered that the sensitivity for the calculation of v_w is particularly high at the very start due the high velocity values u_{LW} and u and low fluid heights. The compensation of a velocity differences of both models is in this case associated with comparably high values for v_w . The scatter of the v_w values based on the discrete data points, as depicted in Figure 49 a), confirms the sensitivity and increasing uncertainty at the very start. The drop of the data scatter around 30 mm is due to the change to a smaller image acquisition rate from 20 hz to 1 hz. The uncertainty of the v_w calculation in the initial phase leads to the assumption that the fitted curve is not representative in this initial phase. Therefore, the progression of the peripheral fluid velocity v_w was considered based on the steady progression starting from the respective maximum in the range around 10 mm.

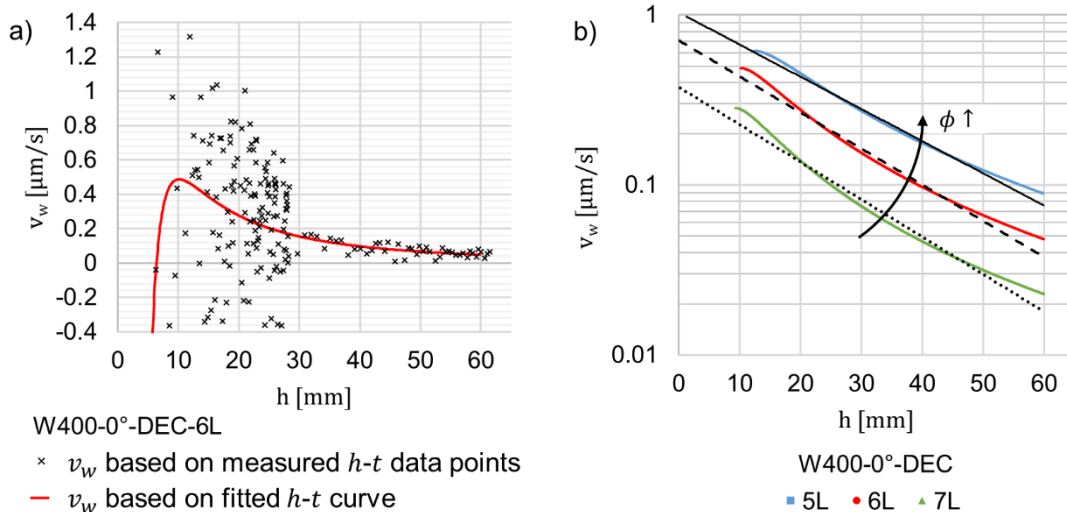


Figure 49: Characteristics of the peripheral fluid velocity v_w over height h . a) Exemplary calculation of the v_w progression, b) Overview of v_w curves with varying porosity content

The diagram in Figure 49 b) illustrates the considered sections of the v_w curve for different porosity contents. Based on this evaluation the progressions of v_w over h are in good correlation with an exponential function of the following form:

$$v_w(h) = a \cdot e^{b \cdot h} \quad (68)$$

where a and b are used as empirical model parameters for the curve regression. It is assumed that the curves can be extrapolated over the initial section which was excluded before. In this context parameter a characterizes the initial intensity which

represents the modeled v_w value at $h = 0$, while parameter b defines the proportional decrease of the peripheral fluid velocity with progressing capillary rise, since b is smaller than zero. The curves in Figure 49 b) show a shift to smaller values and slightly steeper slopes with increasing fiber volume content.

The same tendencies, illustrated for the presented W400 example in Figure 49, can also be observed for all other configurations considered in the test series of this work, which are discussed in the following chapter.

5.3 Test results

In this chapter the results of the conducted capillary test series and the evaluated model parameters are presented. The current investigations focus on two aspects:

- i) The derivation of functional relationships dependent on the actual porosity content ϕ , which is the relevant variable for the process and composite design.
- ii) The separation of the fluid-specific and textile-specific influences on the model parameters, since the experimental approach intends the accurate characterization of the fibrous reinforcement.

In the first part the focus is on the analysis of the capillary action dependent on the textile architecture and includes the analysis of the influence of the yarn orientation in the woven fabrics W200 and W400. The model parameters for the application of the porous tube model are evaluated and the resulting accuracies of the capillary rise prediction for the different fabric types are discussed.

The second part focuses on the influence of the fluid properties on the model parameters. Therefore, the experimental test series on the W400 fabric with varying test fluids are analyzed. Within the scope of the considered test configurations, it can be shown that the peripheral fluid velocity v_w can be separated in fluid and textile dependent parameters, respectively. This allows the prediction of the capillary action in the fabric for different fluids. A further evaluation, which is based on two test configurations on the W400 woven fabric in combination with the epoxy

resin/hardener system, reveals unconsidered effects which are discussed in this context.

5.3.1 Dependence on the fabric architecture

Analysis of the anisotropy in woven textiles

To analyze the dependencies of the yarn orientation in the woven fabrics on the measurable capillary action, the test series include configurations with different orientation angles of the textile cuttings. Therefore, the capillary rise inside the W400 fabric was measured in 0° , 45° and 90° to the textile direction, respectively. For the W200 fabric the differences of the capillary rise between a 0° and 45° orientation were investigated.

The test results for the W400 fabric are shown in Figure 50. Diagram a) contains the evaluated capillary radii dependent on the number of layers and the textile orientation, respectively. It can be observed that the capillary radii increase with decreasing number of layers. This behavior is as expected, since a less compacted preform correlates with a higher porosity, thus larger capillary channels. The comparison of the results from the 0° and the 45° configuration reveals smaller radii in case of the 45° orientation. This is in good correlation with the overall progression of the capillary rise as can be seen in Figure 50 b). The progressions which belong to the 45° test configurations are slightly slower than the ones in 0° direction. This indicates that the orientation of the yarns does have some influence on the capillary action. Based on the results of the 90° configurations the significance of the influence of the yarn orientation shall be classified. The capillary radii of the 90° configurations show the highest values for high porosity contents but also reach the values of the 45° configuration with decreasing porosity. Therefore, a general trend which is related to the yarn angle is not present in this case. The results indicate that the porous structure inside the woven fabric and the resulting anisotropy of the capillary action is not mainly driven by the orientation of the yarns but is also affected by other factors like the weave densities and obviously the compaction state. This is interesting in the sense that tortuosity effects related to an extension of the flow path inside the yarns, as it is the case for the 45° configuration, seems not to significantly reduce the capillary rise inside the woven fabric.

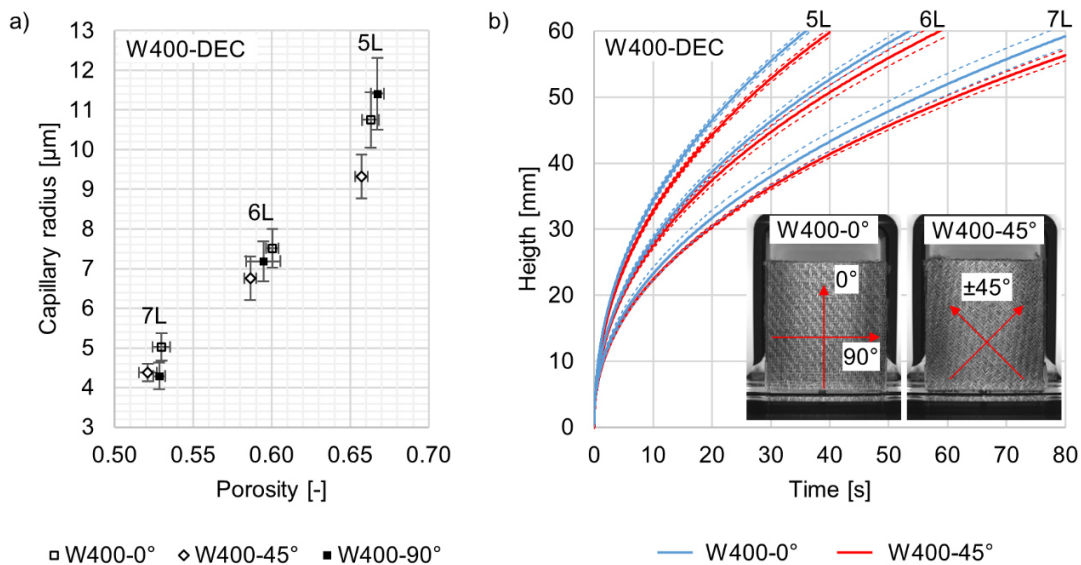


Figure 50: Dependence on the textile orientation: a) Capillary radius and b) Capillary rise for the tested configurations on the W400 fabric with n-Decane

An analog observation can be made based on the results of the W200 fabric. These are depicted in Figure 51. In this case a significant difference between the 0° and the 45° configuration cannot be identified, neither for the evaluated capillary radii nor for the flow front progression, as shown in diagram a) and b), respectively. The divergences between the two configurations show no clear trends and are within the respective standard deviations.

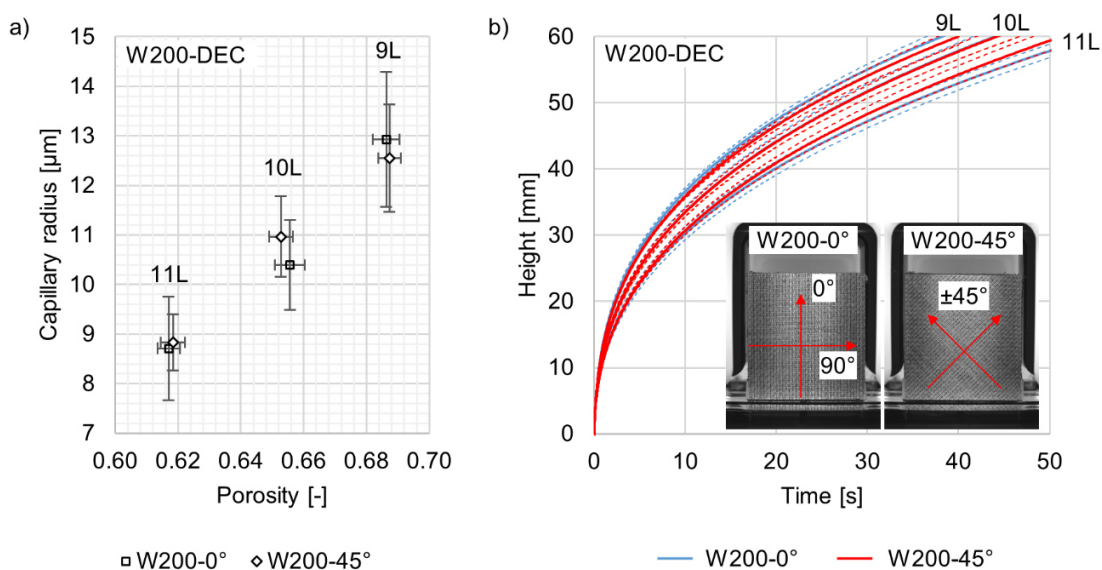


Figure 51: Dependence on the textile orientation: a) Capillary radius and b) Capillary rise for the tested configurations on the W200 fabric with n-Decane

In conclusion it can be stated that for the woven flax fiber fabrics the capillary rise is not mainly influenced by an anisotropic characteristic, thus a deviation of the yarn orientation from the flow direction. In this context the capillary fluid flow inside and along the yarn is obviously not the main mechanism of the capillary action in the fabrics. Indeed, the available and more open pore structure around and between the yarns inside the compacted preform is seen as the determinant factor for the capillary flow velocity.

Comparison of different fabric types

In the following, the results of the applied porous tube model on the tested fabrics are presented. The evaluated capillary radii for the different test series are depicted in Figure 52.

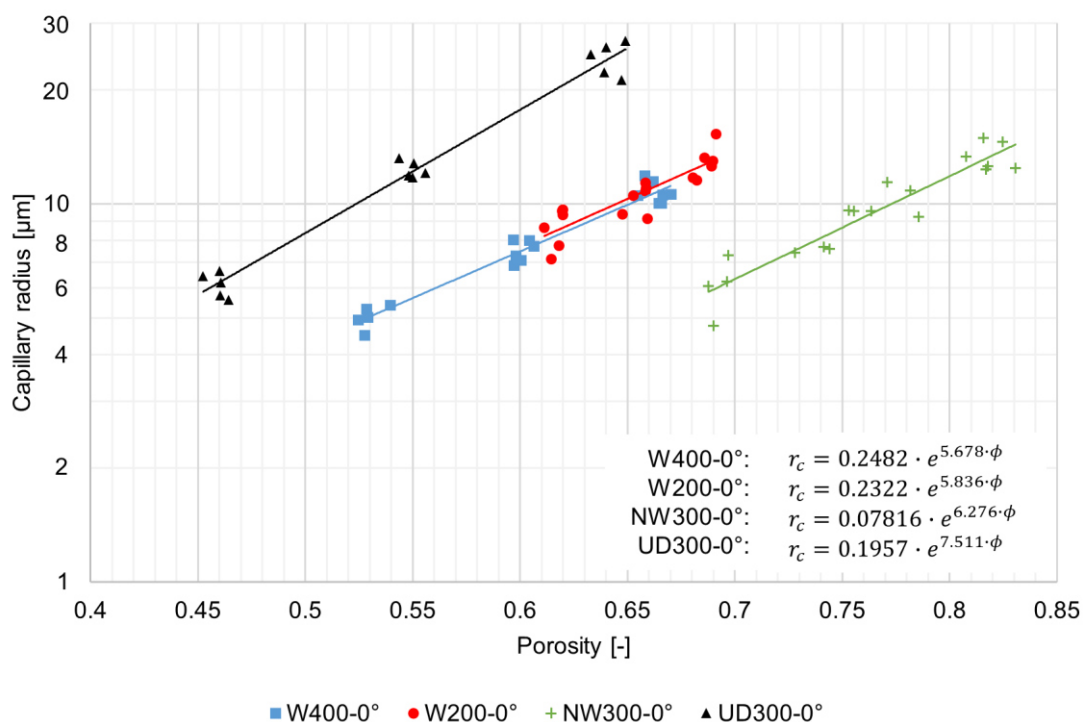


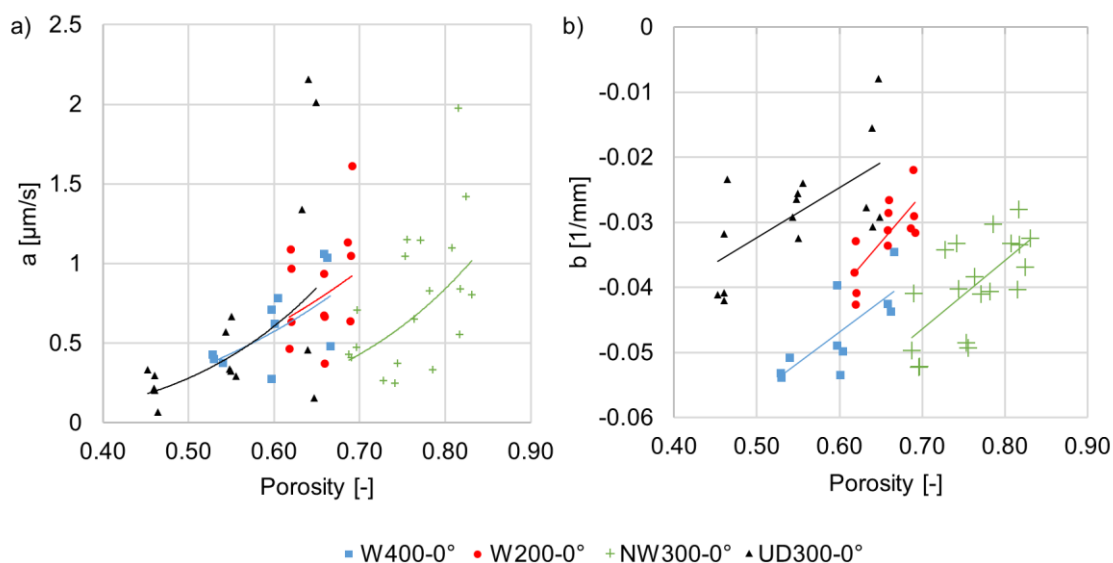
Figure 52: Results for the capillary radii for all considered fabric types tested in 0°-direction with n-Decane

It can be observed that the values are in good agreement with an exponential progression within their respective porosity range. Therefore, it is reasonable to describe the capillary radius over the porosity content by an exponential function of the following form:

$$r_c = c_1 \cdot e^{c_2 \cdot \phi} \quad (69)$$

where c_1 and c_2 are empirical model parameters. Since the capillary radius is a geometric parameter which is intended to characterize the pore morphology of the tested materials, it should ideally be independent of any fluid-specific properties. This characteristic is verified in chapter 5.1.2 based on the results with further test fluids (IPA, PDMS).

The following results show the evaluation of the specific term for the porous tube approach considering a fluid flow across the permeable capillary wall. As described in the previous chapter 5.2.3, this peripheral fluid velocity v_w over the flow front height h is fitted using an exponential function with the model parameters a and b according to Eq. (68). The diagrams a) and b) in Figure 53 show the results for both parameter for all tested fabrics, respectively.



Fit functions

W400-0°:	$a = 2.885 \cdot \phi^{3.161}$	$b = 0.09514 \cdot \phi - 0.1039$
W200-0°:	$a = 2.728 \cdot \phi^{2.933}$	$b = 0.1490 \cdot \phi - 0.1299$
NW300-0°:	$a = 2.575 \cdot \phi^{5.012}$	$b = 0.1053 \cdot \phi - 0.1201$
UD300-0°:	$a = 5.235 \cdot \phi^{4.222}$	$b = 0.07671 \cdot \phi - 0.07074$

Figure 53: Results for the model parameters a and b related to the peripheral fluid velocity v_w

Compared to the results for the capillary radii the two parameters a and b are subject to a noticeable higher scatter. This indicates that the variances of the

measured capillary rise, primary due to inhomogeneities of the natural fiber textiles, sensitively effects the evaluation of the peripheral fluid velocity v_w . Furthermore, according to Eq. (66) the calculated v_w progression is strongly influenced by the evaluated value of the capillary radius. This interaction between the different model parameters also contributes to the resulting scatter of a and b since the deviations in the evaluation of r_c interacts and enhances the variances of the parameters a and b , respectively. Despite of the observed sensitivity, the respective progressions over the porosity content ϕ are described with the intention to represent the mean velocity characteristics using a potential function of the following form for a :

$$a = m_1 \cdot \phi^{m_2} \quad (70)$$

with the empirical model parameters m_1 and m_2 . And a linear progression for parameter b which is as follows:

$$b = n_1 \cdot \phi + n_2 \quad (71)$$

with n_1 and n_2 used as fit parameters. These functional approaches fit to the evaluated data of each material but are distinctively affected by uncertainties due to the high scatter.

Based on the derived functional relationships for the capillary radius r_c , the peripheral fluid velocity $v_w(a, b)$ and the known test fluid properties (dynamic viscosity η , surface tension γ and fiber-liquid contact angle θ) the capillary rise velocity in the porous tube model is calculated according to Eq. (41) which gives:

$$u(h) = \frac{r_c^2}{8 \eta h} \left(\frac{2\gamma \cos(\theta)}{r_c} - \rho g h \right) - \frac{h}{r_c} a \cdot e^{b \cdot h} \quad (72)$$

For the presentation of the results in a clear manner, the corresponding progressions of the flow front height h over time t is used which was calculated numerically based on the velocity progression. The usage of the rectangle rule for this approximation with a height increment of 0.1 mm was found to be adequate to calculate the corresponding time with suitable precision, viz. the error is within the general measurement accuracy and does not affect the following evaluation of the model accuracy.

The diagram in Figure 54 depicts the results for the capillary rise for the W400 configurations within a porosity range between 0.50 and 0.70. Regarding the fluid properties the mean values were considered for the model derivation. The mean fluid temperature and standard deviation is $26.48 \pm 0.99^\circ\text{C}$. Considering the temperature dependencies for the dynamic viscosity η , the surface tension γ and the density ρ , the mean values are $0.83 \pm 0.01 \text{ mPa}\cdot\text{s}$, $23.23 \pm 0.09 \text{ mN/m}$ and $0.72 \pm 0.001 \text{ g/cm}^3$, respectively. With the given fluid properties and the evaluated regression functions for the capillary radius r_c and the peripheral fluid velocity v_w , the model results were compared with the experimental results of each measurement and the accuracy was quantified based on the coefficient of determination R^2 . For each tested configuration, which are specified by the number of layers of the test samples, the results are given in Figure 54.

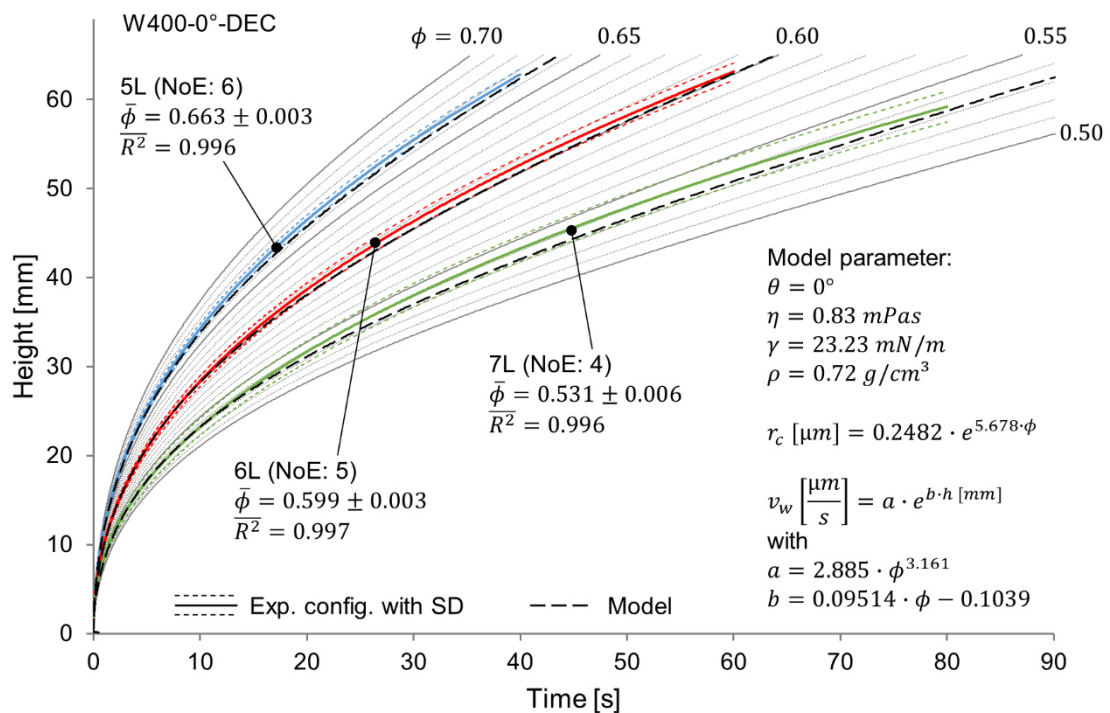


Figure 54: Resulting porous tube model and comparison with the empirical data for the W400-0° configuration with n-Decane

The measured capillary rise for each test configuration is represented by the mean curve of the individual measurements, including the standard deviation which is represented by the respective upper and lower auxiliary lines. The black dashed lines illustrate the modeled progression for each configuration based on the

respective mean porosity content. As can be seen from Figure 54 the modeled progressions accurately fit the empirical data since the deviations from the mean curves stay within the standard deviations of the respective test configuration.

Analogous to the model derivation on the W400 fabric the results for the W200, NW200 und UD300 textiles are illustrated in Figure 55, Figure 56 and Figure 57, respectively. In case of the W200 fabric the lower R^2 values indicate slightly higher deviations between the modeled progressions and the empirical data compared to the results on the previous W400 woven fabric. From the progression curves in Figure 55 it can be observed that the measured capillary rise is slightly underestimated. In this context the high scatter of the parameters a and b in combination with the narrow porosity range for the W200 textile is seen as a critical issue for the derivation of accurate regression functions. The uncertainties in the determination of parameter a and b influence the resulting model divergences, particularly with further wicking progressions.

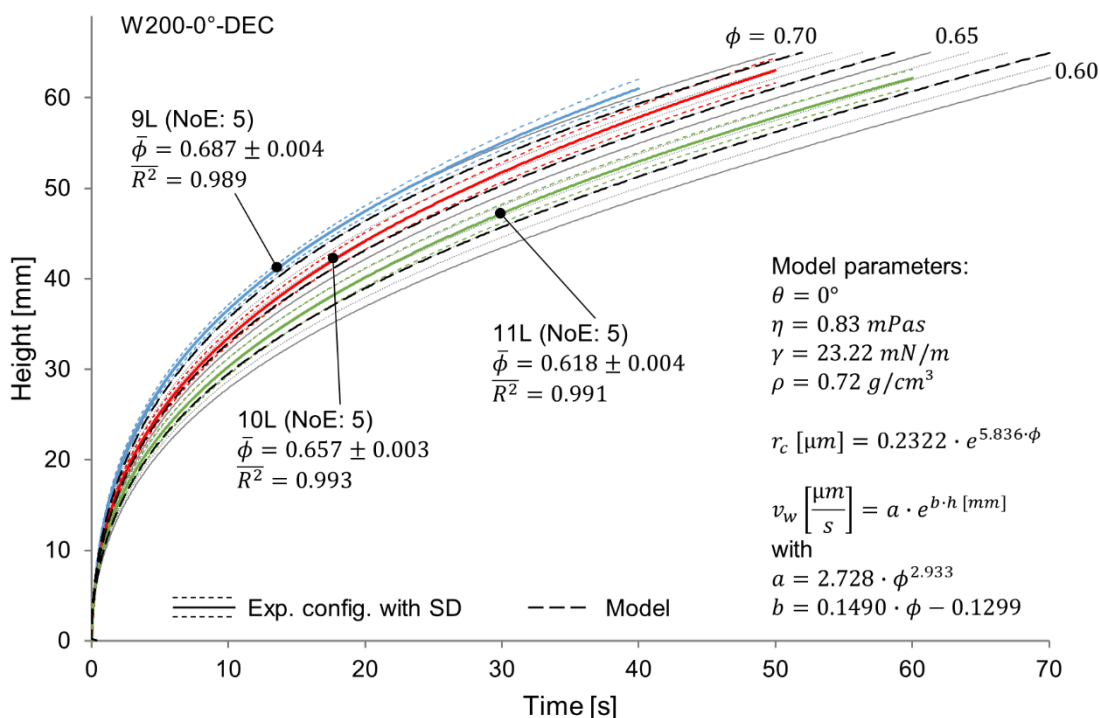


Figure 55: Resulting porous tube model and comparison with the empirical data for the W200-0° configuration with n-Decane

In case of the non-woven fabric NW300 the individual measurements within a test configuration show the highest deviations. This is due to a comparably high scatter of the actual specimen weights, thus the resulting porosity contents, which affect the capillary fluid progression. Despite of the scatter of the textile properties, the applied model is capable to represent the capillary rise over the tested porosity range with decent accuracy, as can be seen from the results illustrated in Figure 56.

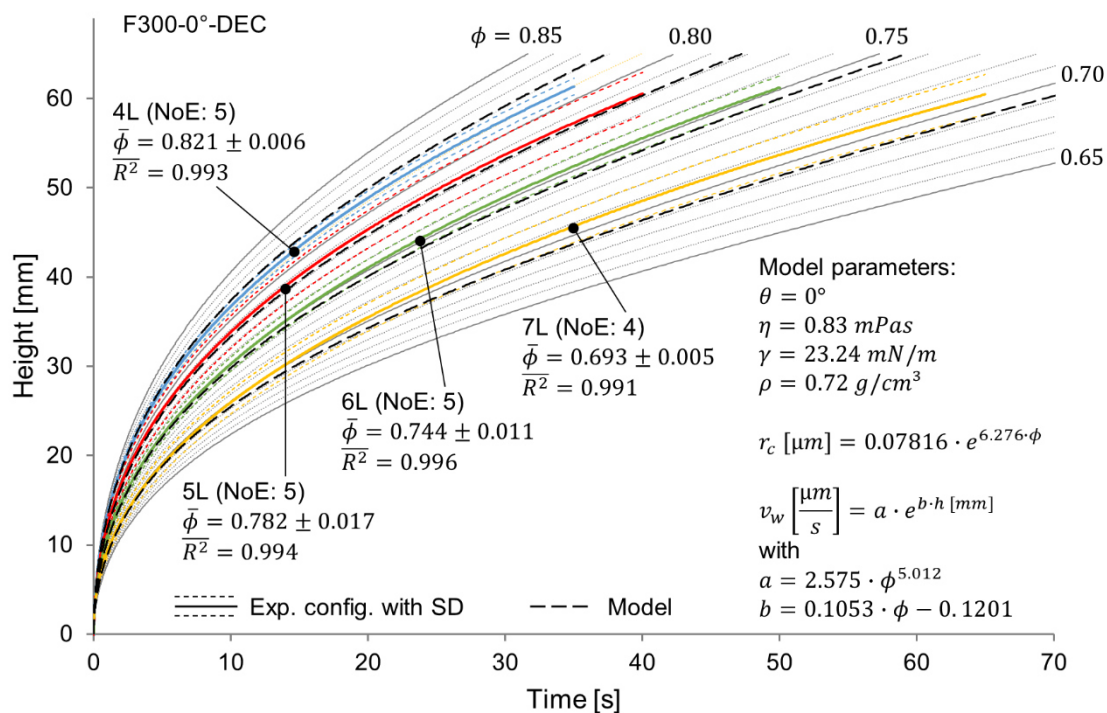


Figure 56: Resulting porous tube model and comparison with the empirical data for the NW300-0° configuration with n-Decane

The high model accuracy continues for the unidirectional fabric UD300. Despite of the uncertainties for the determination of the regression functions for the model parameters a and b , the resulting capillary progression is very close to the experimental evaluation as can be seen in Figure 57.

As a preliminary result, it can be stated that the presented model derivation is capable to describe the capillary rise inside different types of fibrous reinforcements. The consideration of a peripheral fluid flow behind the detectable flow front and its impact on the ascent velocity, as it is described by the porous tube approach, seems to be reasonable adjustment for the model to describe the capillary action inside the

fibrous materials. The resulting deviations between the empirical and the modeled data are likely due to uncertainties in relation to the derivation of the regression functions for the model parameters associated with the peripheral fluid velocity v_w .

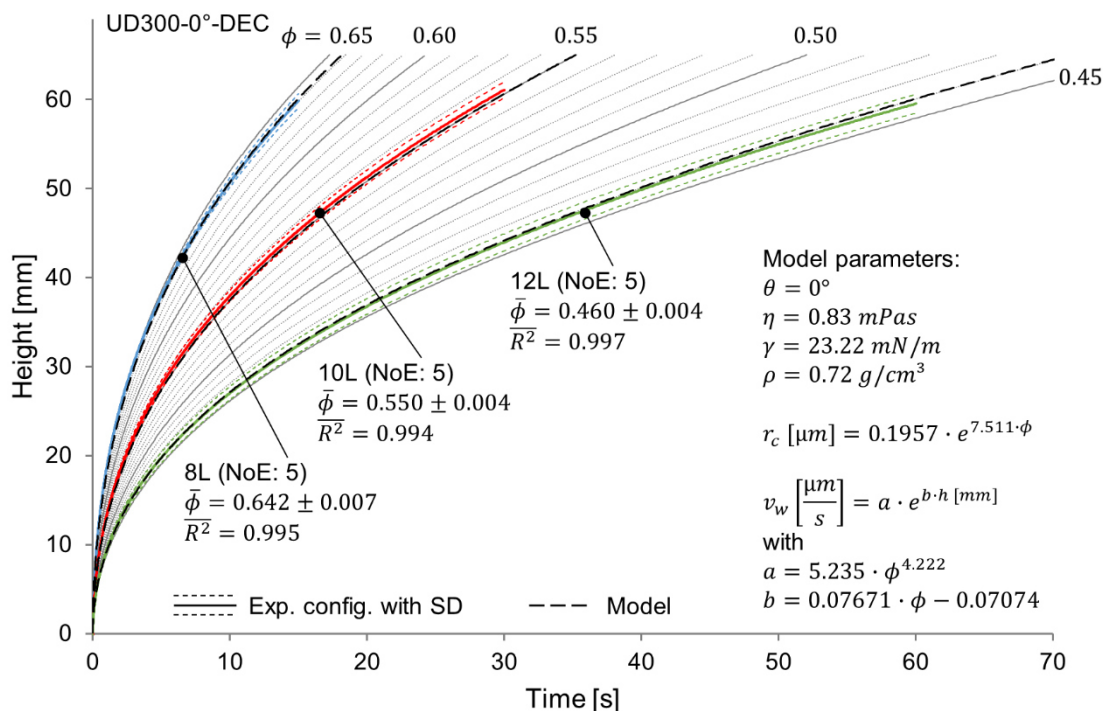


Figure 57: Resulting porous tube model and comparison with the empirical data for the UD300-0° configuration with n-Decane

To conclude, a detailed view is taken to the initial phase of the capillary experiment, since this section is of particular interest with regard to the optimization approaches for the impregnation processes. The moment of contact between the test fluid and the open edge of the textile sample gives detailed information of the capillary action in the surrounding at the pressure driven flow front in LCM processes. Therefore, the model should also be capable to achieve a high precision in the first phase of the experiment. The diagrams in Figure 58 show the model results at the experiment start in comparison with the measured data of the individual experiments for all four fabric types, respectively.

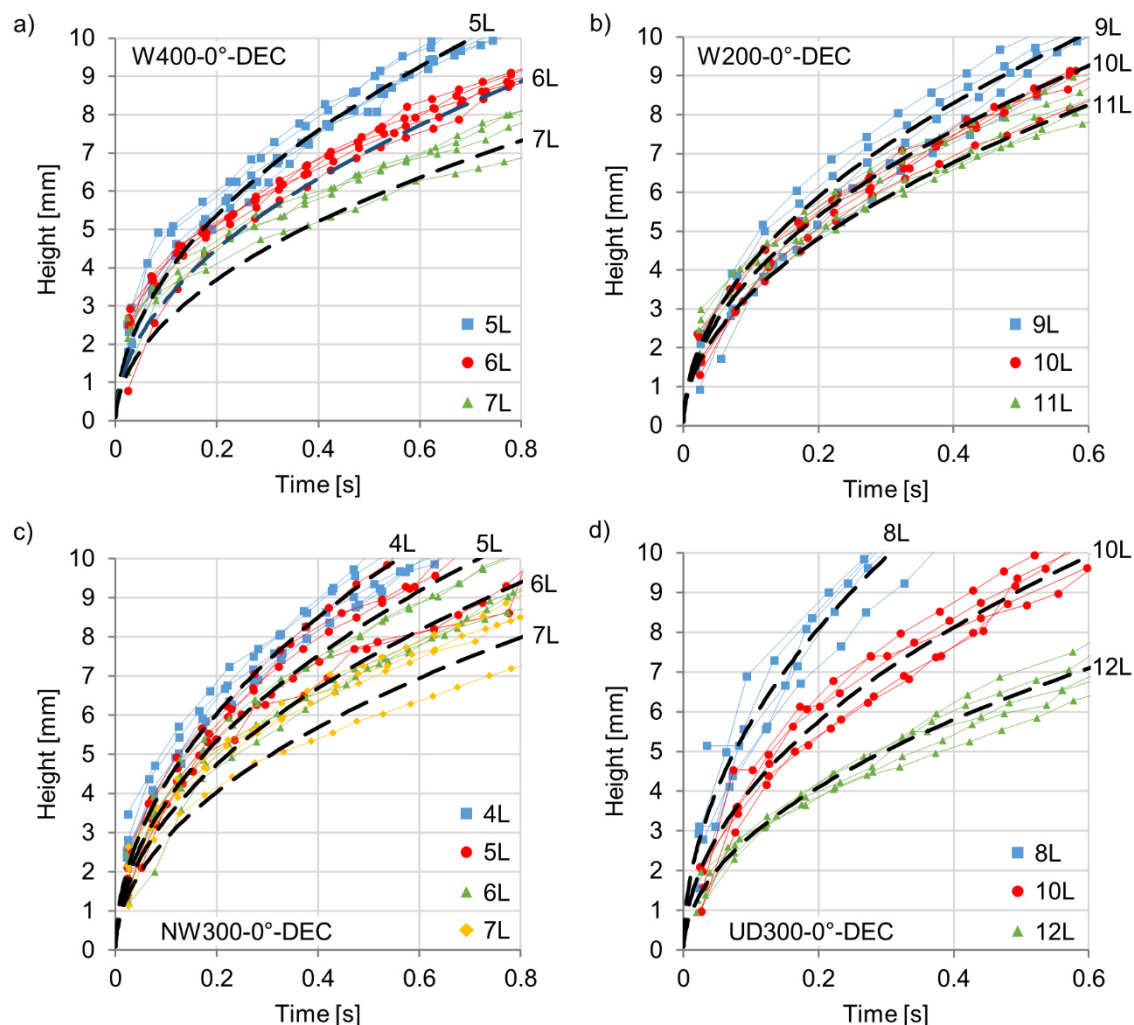


Figure 58: Initial phase of the capillary measurements and modeled progression for all tested fabrics with n-Decane

The results indicate an overall good accuracy in the initial phase. However, the measurement accuracy and the reproducibility of the individual experiments is limited particularly in the range up to ca. 5 mm. For the W400, the W200 and the NW300 fabric the differences between the configurations with varying porosity content is hardly recognizable within the first millimeters of capillary rise, as can be seen in diagram a), b) and c), respectively. In case of the W200 textile the narrow porosity range and in case of the NW300 fabric the high variability of the fabric areal weight contributes to the present situation, respectively. For the W400 and the NW300 fabric it is also noticeable that the measured progressions surpass the model curves within this initial phase. This behavior can presumably be traced back to the imperfections of the open specimen edge. Small shifts of the layers in the

stack and/or the loss of fibers and yarns at the textile edge result in a locally smaller fiber content. In addition, the open edge at the bottom has no support during compaction which allows the material to move outwards to a certain extent which results in a lower degree of compaction at the edge region. As mentioned before, a similar effect leading to a faster fluid progression was observed at the left and right specimen edges. These influences cause variability between the individual experiments and result in a potentially higher porosity state at the open specimen edge which leads to a faster capillary rise at the very start.

The observed variances and influences at the initial phase of the experiment underline the importance of an overall reasonable and accurate model approach for the representation of the capillary saturation inside the reinforcements.

Criteria check for the valid application of the porous tube model

In the following, the requirements related to the flow conditions which were assumed during the model derivation shall be checked for correctness. First, the consideration of the inertial flow regime shall be evaluated in this context. The relevant time t^* which is characterized by a flow regime dominated by inertial forces increases proportional to the capillary radius squared, according to the presented criterion in chapter 2.2.3 (Eq. (54)). The estimation of this initial time span is done considering representative fluid characteristics and the most critical input values based on the experimental results. With a large capillary radius of 100 μm , a typical fluid density of 1 g/cm^3 and a low viscosity value of 1 $\text{mPa}\cdot\text{s}$ the critical time t^* is as follows:

$$t^* = \frac{r_c^2 \rho}{16 \eta} = \mathcal{O}(10^{-3} \text{s}) \quad (73)$$

The resulting timespan for the theoretical change from an inertial to viscous flow domain is in the order of magnitude of 10^{-3}s . This means that the fluid flow within this short time range is not detectable at all with the present experimental approach. Consequently, the influence of inertial forces on the measurements is seen to be irrelevant for the present analysis. With smaller radii and higher viscosities, the critical time span becomes even shorter. Therefore, the neglect of the inertial flow domain for the application of this model is reasonable.

In context to the derivation of the porous tube model in chapter 2.2.3, the justification for the lubrication approximation on tubes with permeable walls was associated with two criteria regarding the peripheral fluid flow situation. The first criterion considers again the ratio of inertial and viscous forces. According to Eq. (39) the Reynolds number related to the peripheral fluid flow through the permeable tube wall must be much less than 1 to ensure the dominance of viscous forces. If the same parameter values are used as before in Eq. (73), the criterion for the peripheral fluid velocity is as follows:

$$Re_w = \frac{\rho |v_w| R}{\eta} \ll 1 \Leftrightarrow |v_w| \ll \frac{\eta}{\rho \cdot r_c} = \frac{1 \text{ mPa} \cdot \text{s}}{1 \frac{\text{g}}{\text{cm}^3} \cdot 100 \mu\text{m}} = 10 \frac{\mu\text{m}}{\text{s}} \quad (74)$$

The highest velocities for the peripheral flow v_w are represented by the intensity parameter a according to Eq. (68), which describes the velocity of the peripheral fluid flow at the starting point ($h = 0 \text{ mm}$). The evaluated results for a in Figure 53 show highest values of the regression curves in the range of $1 \mu\text{m/s}$, while the highest individual values have a maximum in the range of $2 \mu\text{m/s}$. Therefore, the criterion is met even with the conservative inputs for the dimensions of the capillary radius and the fluid viscosity. The second criterion according to Eq. (40) requires a significantly lower peripheral fluid velocity v_w compared to the ascend speed of the fluid u inside the capillary. For the considered test configurations, the v_w/u -ratio is in a range below 10^{-3} across the entire capillary rise. Therefore, this second criterion is met for the present capillary investigations.

Consequently, the requirements of the theoretical approaches related to the porous tube model are fulfilled, which indicates its valid applicability for the present cases and most probably for a wide range of fibrous reinforcements with similar pore morphologies.

5.3.2 Dependence on the fluid properties

For a complete characterization of the fibrous material in terms of the capillary action, the influence of the fluid properties on the model is analyzed in the following. Considering the theoretical approaches for the classical L-W model and the adjusted porous tube model, the capillary radius r_c is already intended to represent the

materials pore morphology. It is assumed that this geometric parameter is independent on any fluid properties, at least if there are no interactions affecting the pore morphology like fiber swelling effects. What is not known so far is the influence of the fluid characteristics on the peripheral fluid flow of the porous tube model. The modeled fluid velocity through the tube wall v_w was determined based on empirical data. The objective in the following part is the separation of the fluid and textile dependent influences for this added parameter to achieve a pure textile-specific characterization of the fibrous material.

Evaluation results with different test fluids

For a variation of the liquid properties, test series were performed with two additional test fluids, 2-Propanol (IPA) and Polydimethylsiloxane (PDMS), as introduced in chapter 5.1.2. The evaluation of the capillary radii of the corresponding experiments on the W400 fabric reveals that the geometric parameter stays in good approximation constant and is, as expected, not significantly influenced by the fluid.

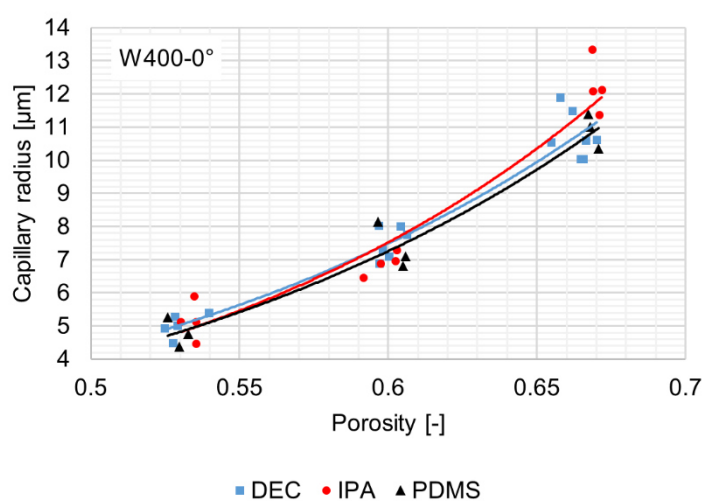


Figure 59: Comparison of the capillary radii based on measurements on the W400-0° configurations with n-Decane, 2-Propanol and Polydimethylsiloxane

The resulting r_c values related to the three different test fluids are depicted in Figure 59 including the corresponding exponential regression curves. Considering the uncertainties due to the scatter of the data, the assumption for the capillary radius to be a textile-specific parameter is reasonable. Thus, for the following model

derivations the regression curve, as evaluated before for n-Decane, is used further on to define the capillary radius over the porosity.

Furthermore, the regression functions for the parameters a and b according to Eq. (70) and Eq. (71), and to define the peripheral fluid velocity v_w , are analyzed. The results for n-Decane and 2-Propanol are depicted in Figure 60. For parameter a significant lower values can be observed in case of 2-Propanol, while the progression for parameter b shows no significant differences between both test fluids considering the present uncertainties. Regarding the exponential regression curve for the peripheral fluid velocity v_w according to Eq. (68), 2-Propanol leads obviously to lower initial values for v_w but the proportionate reduction of the velocity with increasing fluid heights seems to be unaffected by the test fluid properties.

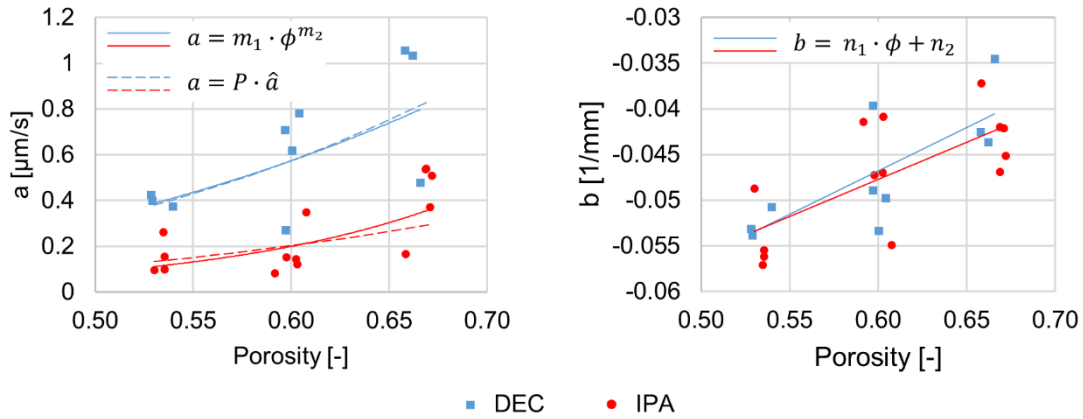


Figure 60: Comparison of the fluid dependent model parameters related to the peripheral fluid velocity v_w

Considering the dependence of the fluid properties on v_w , it is assumed that the peripheral fluid velocity through the tube wall is affected analogous to the fluid flow inside the non-porous capillary described by the classical L-W model. As shown in chapter 2.2.3 and according to Eq. (22) the fluid velocity of the L-W approach u_{LW} over the flow length h can be written as follows:

$$u_{LW}(h) = \frac{r_c}{4h} \cdot \frac{\gamma \cos(\theta)}{\eta} = \frac{r_c}{4h} \cdot P \quad \text{with} \quad P = \frac{\gamma \cos(\theta)}{\eta} \quad (75)$$

where P is the so-called penetrativity of the fluid which depends on its liquid surface tension γ , the dynamic viscosity η and the fluid-fiber contact angle θ [82]. This notation is intended to separate the fluid- and textile-specific influences on the

velocity. From Eq. (75) a direct proportionality between the fluid velocity and its penetrativity value can be identified. Transferring this relationship to the expression for the peripheral fluid velocity in the porous tube model, the corresponding regression curve becomes:

$$v_w(h) = a \cdot e^{b \cdot h} = P \cdot \hat{a} \cdot e^{b \cdot h} \quad (76)$$

where the parameter \hat{a} represents the fluid independent intensity factor based on the adjusted regression function which is defined as follows:

$$\hat{a} = \hat{m}_1 \cdot \phi^{\hat{m}_2} \quad (77)$$

For the derivation of \hat{a} the regression functions evaluated for a over the porosity ϕ , as shown in Figure 60, are used considering the mean penetrativities of n-Decane and 2-Propanol which are 28.03 m/s and 9.87 m/s, respectively. According to Eq. (76) the relationship between a and P is linear and defined by the slope \hat{a} as shown in diagram a) of Figure 61 for varying porosity contents.

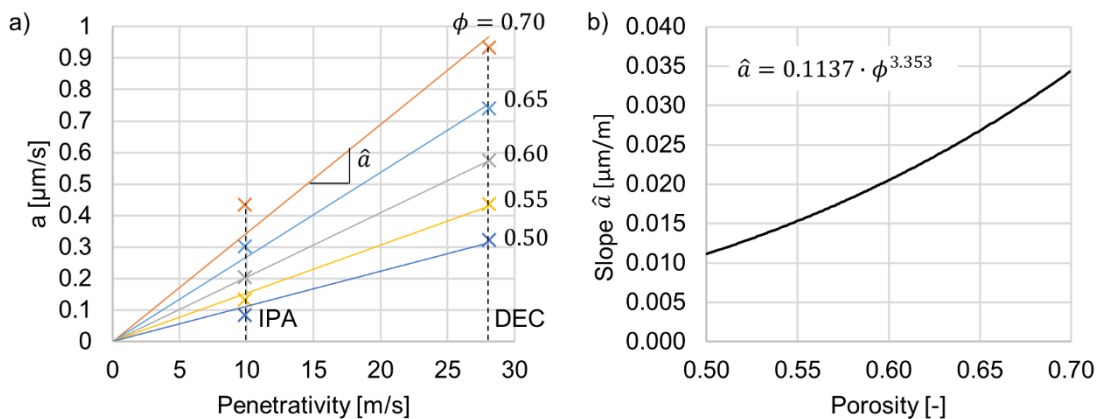


Figure 61: Derivation of the fluid independent regression function for \hat{a}

The corresponding function of \hat{a} over the porosity ϕ according to Eq. (77) is depicted in diagram b). To control the divergences made by this generalization approach the corresponding curves are included in Figure 60 a) for comparison. The differences between the original regression function for a and the generalized curve ($a = P \cdot \hat{a}$) is small and the changes are reasonable considering the overall scatter and uncertainties of this regression. Considering the changes related to this approach to separate fluid- und textil-specific influences, the velocity for the capillary rise in the porous tube model is defined as follows:

$$u(h) = \frac{r_c}{4h} \cdot P - \frac{r_c^2}{8\eta} \rho g - \frac{h}{r_c} \cdot P \cdot \hat{a} \cdot e^{b \cdot h} = u_{LW} - u_g - u_p \quad (78)$$

The first term represents the velocity based on the classical L-W equation with the textile-specific capillary radius r_c and the fluid-specific penetrativity P . The second term represents the velocity reduction due to gravitational forces depending also on r_c , the liquid density ρ and the dynamic viscosity η . The third term represents the velocity reduction due to the flow outwards of the porous capillary which depends on r_c , the fluid-specific penetrativity P and the model parameters \hat{a} and b . In this generalized form \hat{a} and b characterize the textile-specific behavior on the peripheral fluid flow.

For the sake of completeness it shall be mentioned that the contact angle between the liquid and the fibre surface depends obviously also on the fiber properties. Therefore, the wetting characteristics between the liquid and the fiber surface must be known and any changes on the fibrous material which affect them must be considered. This makes the penetrativity P strictly speaking not solely fluid dependent but defines its wicking capabilities in combination with the given fiber material. Since there are no changes of the fiber properties considered in this work, the penetrativity is used in the present context as a fluid-specific value.

The validity of the derived generalized model is analyzed by comparing the prediction with the experimental results for 2-Propanol and Polydimethylsiloxane. While the textile-specific parameters (r_c , \hat{a} and b) stay constant, only the changes of the fluid properties are considered for the model derivation by using the mean values for the dynamic viscosity η , surface tension γ and density ρ , respectively. Figure 62 depicts the results for 2-Propanol. The comparison of the imbibition times with the results for n-Decane in Figure 54 reveals a significant slower progress of the capillary rise in case of 2-Propanol, due to the lower fluid penetrativity. The accurate fit of the model, indicated by the R^2 values close to 1, supports the assumptions and adjustments related to the separation of fluid- and textile-specific influences.

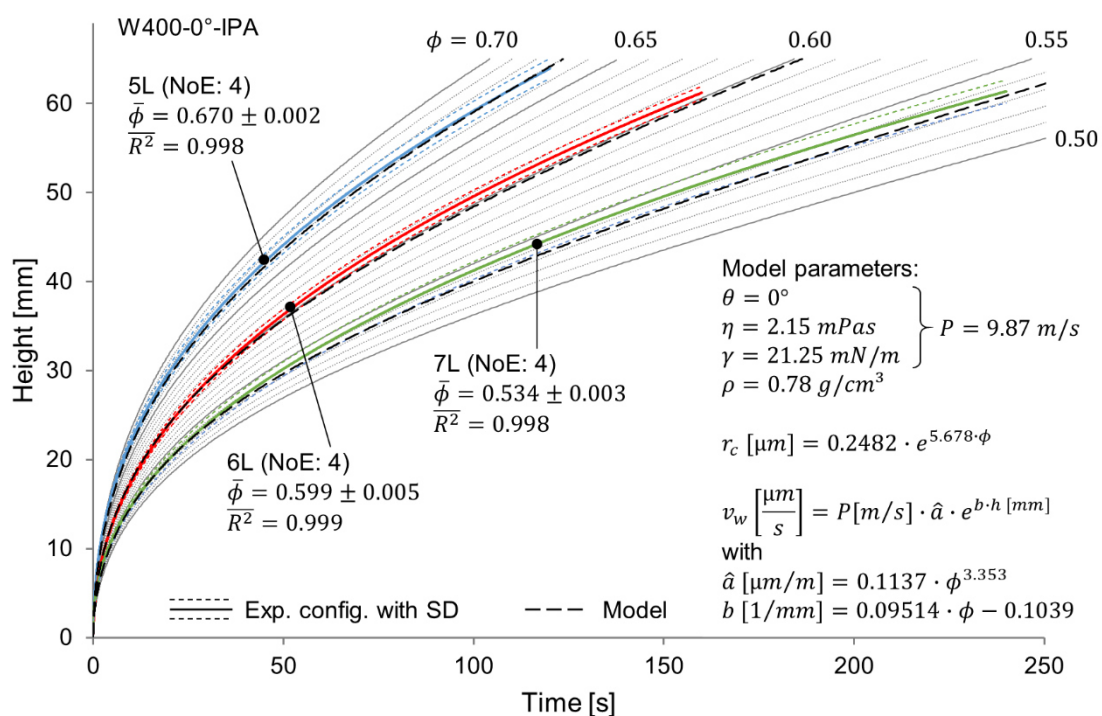


Figure 62: Resulting porous tube model and comparison with the empirical data for the W400-0° configuration with 2-Propanol

Due to its comparably high viscosity Polydimethylsiloxane (PDMS) extend the range of considered fluid penetrativities to cover the values of typical resin systems used for LCM infiltration processes. The model and experimental results for PDMS are depicted in Figure 63. According to the fluid properties, the progression of the capillary rise is significant slower. The experiments were stopped after a certain progress of around 15 to 20 mm was reached which allows an accurate evaluation of the experiments. Within the tested height range the model prediction shows again a high accuracy, considering that all textile-specific inputs were derived based on the measurements with n-Decane and 2-Propanol, thus test fluids with significantly different penetrativity characteristics.

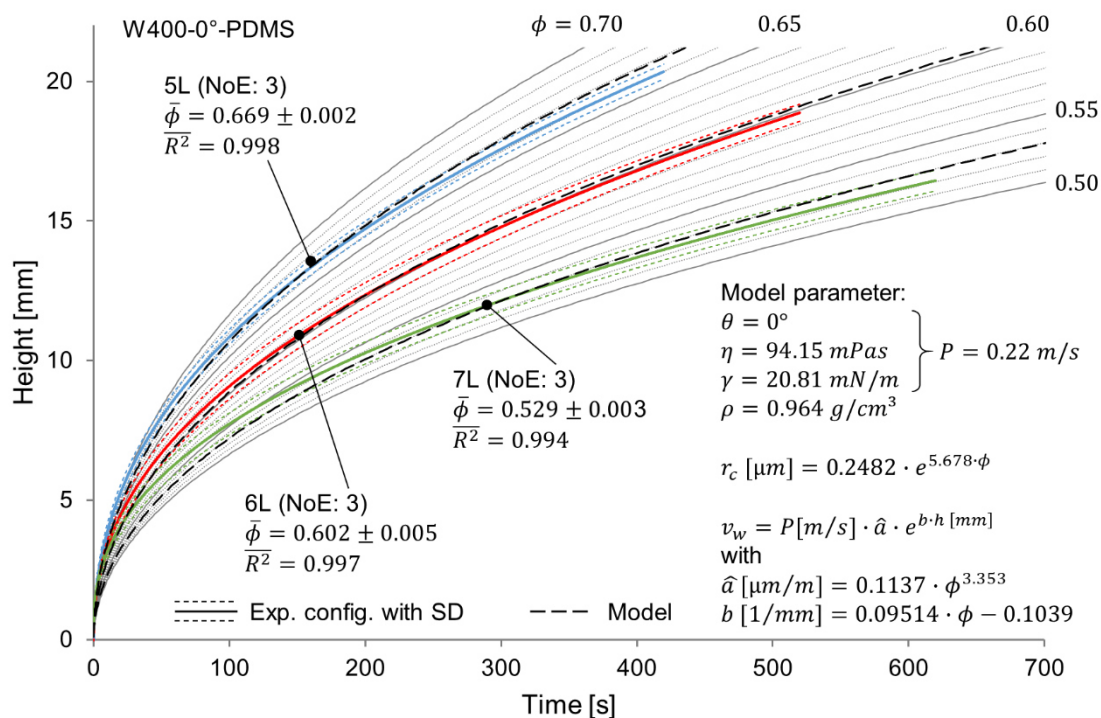


Figure 63: Capillary rise based on the porous tube model for the W400 fabric (0°) and Polydimethylsiloxane

The comparison of the model results and the empirical data at the initial phase of the capillary rise show the same tendencies, as observed for n-Decane in Figure 58. The detailed sections of the modeled progression and empirical data points are depicted in Figure 64 a) and b) for 2-Propanol and Polydimethylsiloxane, respectively. The overall accuracy of the model is reasonably good, but the measured progressions show again the tendency of a faster capillary rise within a fluid height of approximately 5 mm. As discussed before and based on the observations in Figure 58 the probable reason for this is related to the present deviations of the fibrous reinforcement at the open edge of the textile samples, which leads to a lower compaction state with locally larger pore spaces, thus a faster fluid rise in the initial phase.

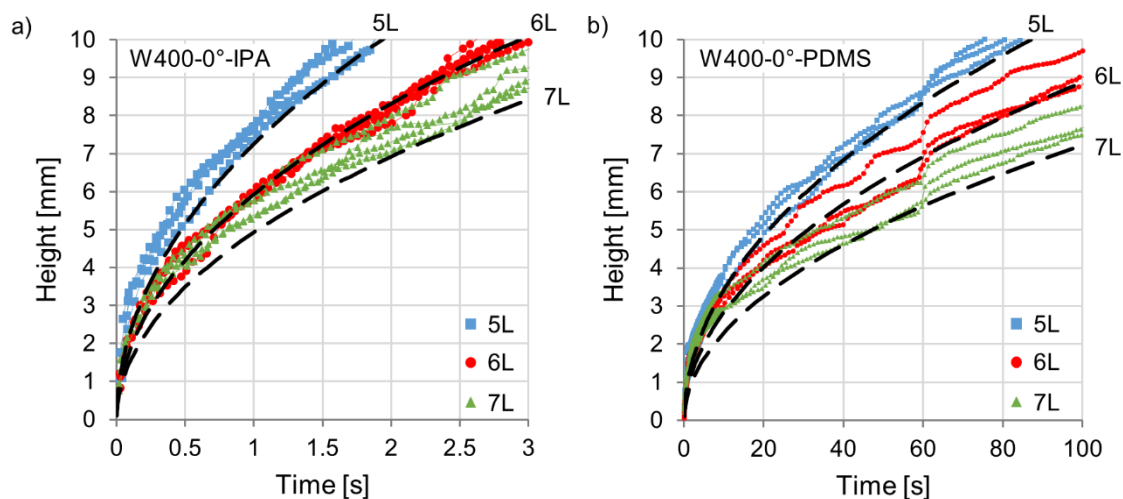


Figure 64: Initial phase of the capillary measurements and modeled progression for the W400-0° configuration with a) 2-Propanol and b) Polydimethylsiloxane

Capillary test results using the epoxy resin system

To check the transferability of the capillary rise model to a representative polymer system, additional experiments were performed using the epoxy resin/hardener system Epinal LR80 A2.01/Epinal LH80 B2.00, as presented in chapter 3.2. The experiments were performed at higher temperatures. Therefore, the W400 textile samples, the glass blocks of the specimen holder, the resin and the hardener component were heated up at 70°C using a convection oven (Model FDL 115, Binder GmbH, Germany). The relevant fluid parameters for the porous tube model were derived based on the measurements for its density and viscosity or estimated based on literature data. For the surface tension a value of 40 mN/m is used representing the mean value of literature test results for similar epoxy systems, which are in the range between 35 mN/m and 45 mN/m [149], [166]. [167]. The contact angle was defined to 55°, which is in the range of the measurement results from Pucci [149] which are $54.4^\circ \pm 1.5^\circ$ and $52.2^\circ \pm 2.4^\circ$ for a liquid multi-purpose epoxy resin and a biobased epoxy resin system on cellulose fibers, respectively.

During the preparation of the capillary experiment the preheated resin and hardener components were weighed and mixed with the intended mixing ratio of 100:25 by weight and poured into the fluid container of the test setup. The measured resin

temperatures during the test were in the range between 60°C and 70°C. The temperature differences of this test series are a critical factor in terms of uncertainties of the input parameters. In the present case the dynamic viscosity which is related to the viscosity measurement at 65°C was used to define the input value for the porous tube model. Therefore, the dynamic viscosity was set to 35 mPa·s considering the time needed from mixing of the components until the experiment start. The modeled results in comparison with the measured capillary rise are depicted in Figure 65. For both considered test configurations the deviations from the modeled curves increase with further progression. The start shows a relatively good fit and in accordance with the accuracies observed before for other test liquids. With further wicking heights the measured progression become slower than the modeled prediction.

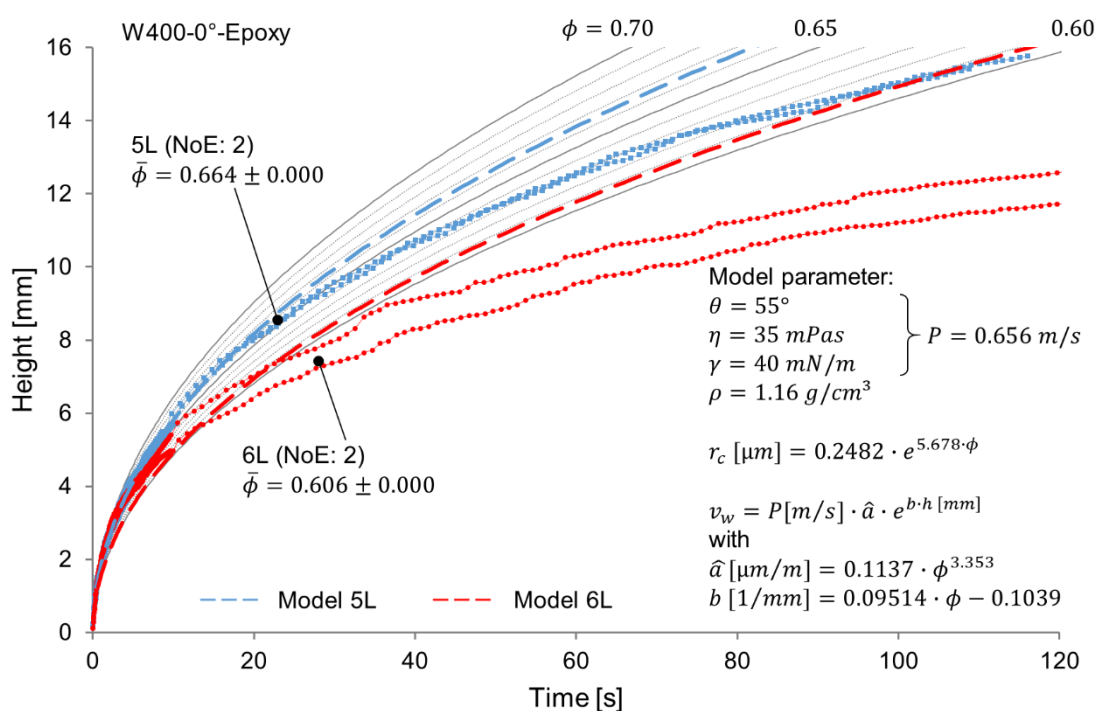


Figure 65: Capillary rise based on the porous tube model for the W400 fabric (0°) and the epoxy resin system

Two possible effects which were unconsidered so far could be the reason for the observed deviations. The first one is related to the fluid properties and its actual penetrativity. Due to the cross-linking reaction the viscosity of the resin system increases during the experiment time. This dynamic change of the related fluid

properties is not considered in the model. Figure 66 a) depicts the change of the capillary rise with varying penetrativity values considering a porosity content of 60.6% which represents the 6-layer configuration in this test series. According to Eq. (77) the penetrativity decreases with increasing viscosity which causes a slowing of the capillary rise, as observed before. The second influence considers a possible reduction of the effective capillary radius due to a liquid absorbing and swelling effects of the flax fibers. In Figure 66 b) the modeled fluid progressions related to varying sizes of the initial radius are shown. The reduction of the capillary radius leads also to a slower capillary rise. The tendency for natural fibers to swell in epoxy resins was reported by Massodi *et al* [168] who measured that time dependent effect on sisal fibers.

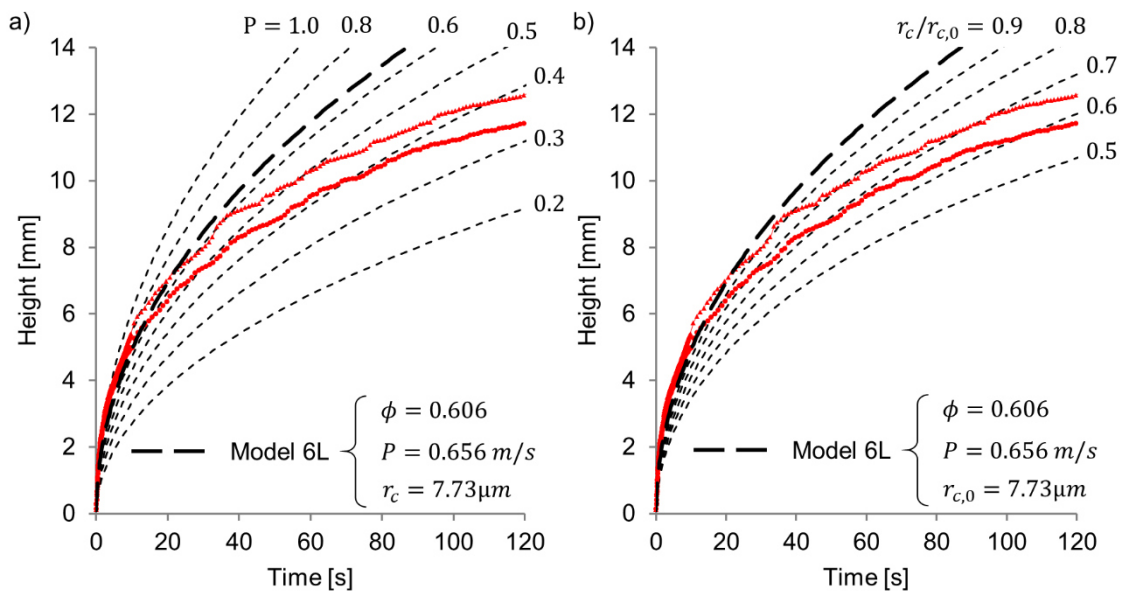


Figure 66: Influence of a) the penetrativity P and b) the capillary radius r_c on the modeled capillary rise progression

Based on the viscosity measurements on the epoxy system, as reported in chapter 3.2, the viscosity increase during the imbibition time of the experiment is in the range of 6 mPa·s which corresponds to a penetrativity reduction from 0.656 m/s to 0.560 m/s, whereby the estimated values for the contact angle and the liquid surface tension are assumed to be constant. The predicted progression for the penetrativities in this range still overestimates the measured data as can be seen in Figure 66 a). Therefore, a combination of both effects might be responsible for the actual behavior of the capillary action. The results of this test series indicate the

limitations of the derived model which does not consider such fiber-fluid interactions and dynamic changes of the fluid properties yet. Nevertheless, the model shows again a reasonably good prediction in the most relevant initial starting phase of the capillary rise, where the unconsidered time-dependent influences remain negligible.

5.4 Discussion

It was shown that the derived model, considering a peripheral fluid flow through a porous capillary wall, leads to an accurate representation of the capillary rise inside different flax fiber fabrics with various textile architectures. The observed deviations are explainable due to effects which were not explicitly considered in the model. Such as the generally faster initial capillary rise near the open specimen edge, due to a varying porosity state, or the overestimation with further progress in case of the epoxy resin system, due to the cure reaction and a possible fiber swelling effects. Furthermore, the analysis with different test fluid properties allowed the separation of textile- and fluid-specific input variables of the model and enabled a clear characterization of the capillary properties inside the fibrous reinforcement. Based on the experimental and modeled results, the optimization approach for the impregnation velocity, as presented in chapter 2.4, is discussed in the following. Furthermore, the influence of the capillary pressure on the textile permeability, which was neglected during the characterization in chapter 4, is analyzed.

5.4.1 Optimization of the fiber impregnation in liquid composite molding processes

In this section the utilization of the results from the capillary rise experiments for the estimation of an optimal impregnation conditions is discussed. The different textile architectures which were considered in this context showed similar characteristics related to their capillary properties, which allowed the application of the porous tube model equally for all tested fabric types. However, the specific fluid flow inside the textiles depends on the given pore morphology, which is interpreted more in detail in the following. In Figure 67 a schematic overview of the spontaneous capillary fluid imbibition is depicted for the different reinforcements, respectively. The common phenomenon is a delayed saturation of pore spaces, which takes places behind the

visible main capillary flow front. A logical justification for this is due to the irregular pore structure with varying pore sizes and shapes, which allow the fluid to wick faster in some locations than others. In case of the unidirectional yarn architecture, it is assumed that the larger channels between the yarns are responsible for the main flow front propagation, while the wicking into the smaller pore spaces takes place simultaneously but correspondingly slower. In case of woven textiles, the two yarn systems lead to a distribution of the fluid flow at every intersection point which causes in addition to the beforementioned effect a delayed saturation inside the perpendicular oriented yarns. The non-woven fabric also shows the tendency for a partly saturated area behind the capillary flow front which can be explained by the distribution of smaller and larger pore channels, thus a varying wicking velocity along the flow front. Consequently, it might be stated that the formation of microvoids can also result just from the spontaneous capillary driven saturation due to the present variances inside the porous structures.

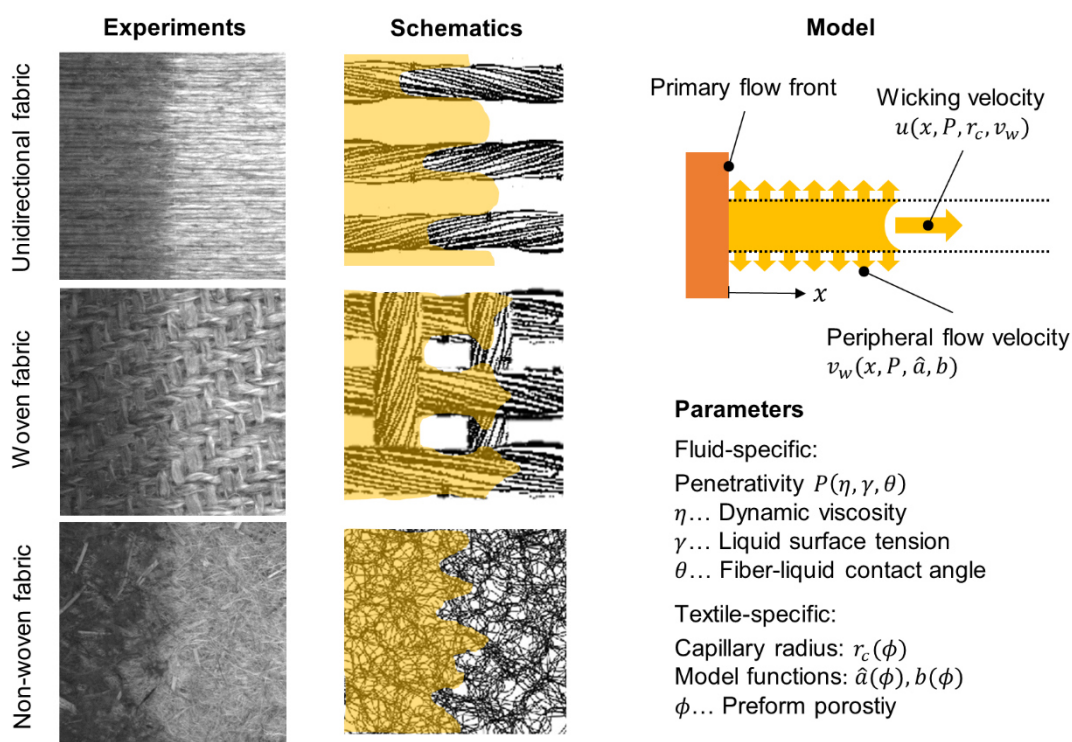


Figure 67: Overview of the porous tube model to predict the capillary wicking in different types of fibrous reinforcements

To minimize the detrimental effects of flow-induced void formation the approach, as shown in chapter 2.4, is applied which based on the textile-specific characteristic

mesoscopic length L_c . This is done based on the W400 woven fabric since the mesoscopic length value corresponds in this model with the yarn distance oriented perpendicular to the flow direction. This geometric information provides orientation for a first consideration of this model approach, which is not given for the unidirectional and non-woven textile architectures. A further validation of the optimal impregnation velocity on the unidirectional textile and the W400 woven fabric is covered in chapter 6 based on void measurements on an RTM test series.

According to Eq. (78) the velocity for the capillary driven flow without the influence of gravitational forces is given as follows:

$$u(x) = \frac{r_c}{4x} \cdot P - \frac{x}{r_c} \cdot P \cdot \hat{a} \cdot e^{b \cdot x} = u_{LW} - u_P \quad (79)$$

The capillary radius r_c and the parameters \hat{a} and b are model functions which depend only on the preform porosity ϕ . While these parameters represent the textile-specific behavior, the penetrativity P consists of the liquid properties: dynamic viscosity η , surface tension γ and contact angle θ . The velocity term u_{LW} represents the dynamic flow progression based on the L-W approach, while u_P considers the velocity reduction due to the peripheral flow. The gravitational influence is neglected due to a regarded flow direction in horizontal direction. Furthermore, since the initial fluid progression was derived based on the L-W equation, the influence of the peripheral flow on the resulting flow front velocity is small for short flow distances. The ratio between the two velocity terms u_P and u_{LW} with varying fluid heights is depicted in Figure 68. It can be observed that the proportion of u_P on the overall velocity is small at the start, reaches a maximum during the capillary rise and decreases again with further progression. This behavior is similar for all tested fabric types. The decreasing influence of the peripheral fluid flow is in accordance to the measurement results from LeBel [119] who observed, beside the initial capillary rise, a reduced flow progression for 'medium-term' heights which was described by a second application of the L-W model.

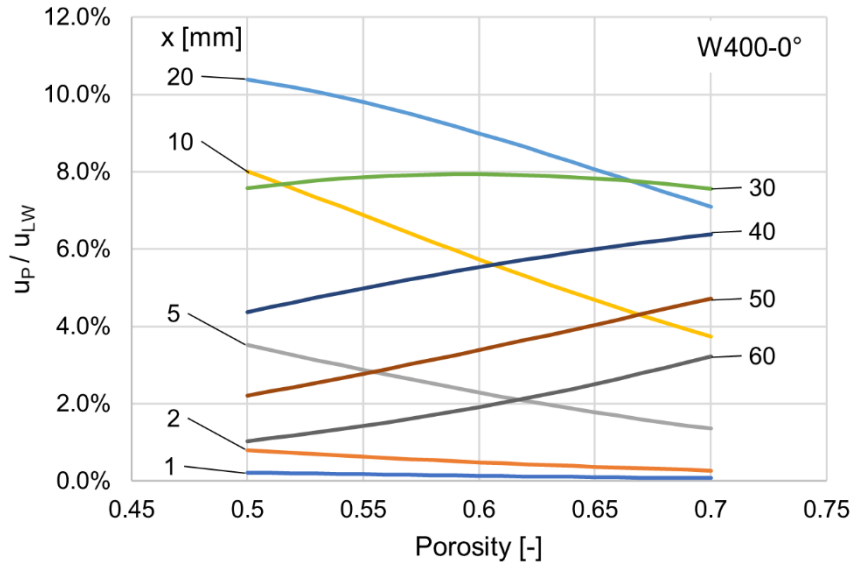


Figure 68: Influence of the peripheral fluid flow on the ascent velocity dependent on the flow length

Considering the flow velocity only for short distances, the relationship from Eq. (61) can be applied in good approximation which gives the following equation for the optimal impregnation velocity:

$$v_{p,opt} = u\left(\frac{L_c}{2}\right) = \frac{r_c}{2L_c} \cdot P - \frac{L_c}{2r_c} \cdot P \cdot \hat{a} \cdot e^{b \cdot x} \quad (80)$$

The modified capillary number Ca^* , as introduced in chapter 2.4, gives the following relationship considering the actual fluid penetrativity P :

$$Ca^* = \frac{\eta U}{\gamma \cdot \cos(\theta)} = \frac{v_p}{P} \quad \text{with} \quad P = \frac{\gamma \cos(\theta)}{\eta} \quad (81)$$

Inserting Eq. (80) in Eq. (81) gives the expression for the optimal modified capillary number Ca_{opt}^* depending on the characteristic mesoscopic length L_c and the textile-specific model parameters r_c , \hat{a} and b :

$$Ca_{opt}^* = \frac{r_c}{2L_c} - \frac{L_c}{2r_c} \cdot \hat{a} \cdot e^{b \cdot x} \quad (82)$$

The corresponding optimal impregnation velocity $v_{p,opt}$ for a liquid with penetrativity P is then given as follows:

$$v_{p,opt} = P \cdot Ca_{opt}^* \quad (83)$$

The application of this approach on the W400 woven fabric is depicted in Figure 69. Varying inputs for the mesoscopic length L_c were considered regarding the measured weft yarn distance D_{weft} according to the determined weave density, as reported in Table 6. The results indicate that the definition of the characteristic mesoscopic length L_c is quite sensitive to the prediction of optimal impregnation velocities. A variation of L_c was considered to take into account the uncertainties of this parameter in the given textile and to reveal the potential range of optimal capillary numbers, which is further validated in chapter 6.

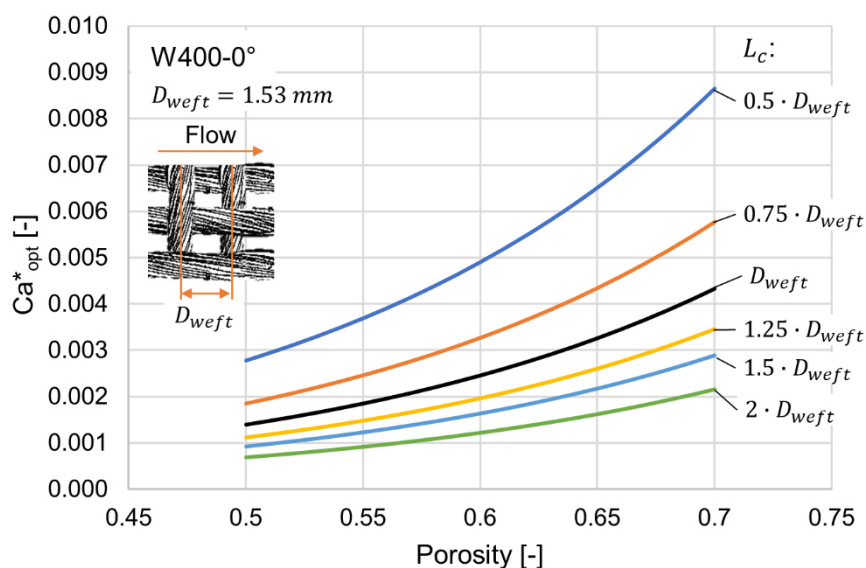


Figure 69: Optimal capillary number over porosity dependent on the characteristic mesoscopic length

The comparison of determined Ca_{opt}^* values, derived in previous studies, confirms the overall range of the present results. Patel and Lee reported Ca_{opt}^* ranges between $1.03 \cdot 10^{-3}$ and $3.01 \cdot 10^{-3}$ for a glass fiber woven fabric ($\phi = 0.61$), $0.70 - 2.15 \cdot 10^{-3}$ for a bidirectional glass fiber NCF ($\phi = 0.68$), $1.05 - 6.02 \cdot 10^{-3}$ for axial flow in an unidirectional NCF ($\phi = 0.57$) and $0.94 - 3.55 \cdot 10^{-3}$ for a random fiber mat ($\phi = 0.73$) [105]. Mahale derived optimal modified capillary numbers Ca_{opt}^* for different random glass fiber fabrics ($\phi = 0.76$ and $\phi = 0.72$) in the ranges of $4.04 - 4.46 \cdot 10^{-3}$ and $3.71 - 3.96 \cdot 10^{-3}$, respectively [108].

Based on the derived Ca_{opt}^* values, as depicted in Figure 69, a further analysis of the determination of optimal impregnation conditions is covered in chapter 6 based on an RTM test series with defined impregnation velocities and subsequent void measurements on the resulting composites.

5.4.2 The capillary pressure and its contribution on the permeability determination

A second approach to utilize the results from the capillary analysis is presented in the following, regarding the permeability characterization of the reinforcing fabrics. During the in-plane permeability characterization of the flax fiber fabrics in chapter 4 the capillary pressure at the flow front was not considered due to the lack of necessary and accurate input data. Based on the findings obtained from the capillary investigation, the resulting error related to this neglect shall be evaluated. Therefore, the one-dimensional fluid flow through the porous material is regarded, as depicted in Figure 70. In contrast to the scenario discussed in chapter 2.2.2, the pressure gradient considers the capillary pressure drop at the flow front. Consequently, the total pressure difference depends now on the inlet pressure over the ambient pressure p_{in} and the capillary pressure Δp_c . In Figure 70 Δp_c is plotted with the assumption of wetting fluid properties ($\theta < 90^\circ$), thus a flow-promoting pressure drop in negative direction.

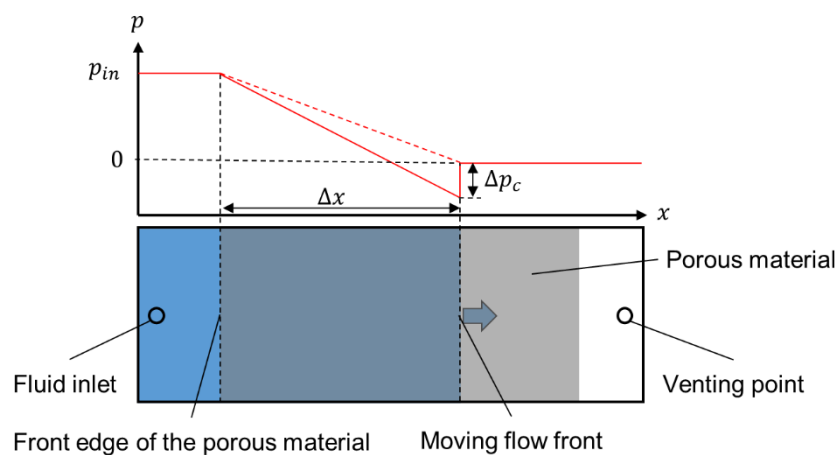


Figure 70: Pressure gradient for a one-dimensional fluid flow through a porous medium with consideration of capillary pressure

According to Eq. (12) the relationship between the flow front velocity $v_{p,x}$, the porosity ϕ , the dynamic fluid viscosity η , the flow length Δx and the product of the permeability k_x and the pressure difference Δp is given as follows:

$$k_x \cdot (-\Delta p) = v_{p,x} \cdot \phi \cdot \eta \cdot \Delta x \quad (84)$$

The right side of Eq. (84) is constant since the related parameters resulted from the flow front detection during the permeability experiment or are defined by the material and fluid properties. To calculate the error due to the neglect of capillary pressures, Eq. (84) gives the following equation:

$$k_x \cdot p_{in} = k_{x,c} \cdot (p_{in} + \Delta p_c) \quad (85)$$

where k_x and $k_{x,c}$ are the permeability values without and with consideration of the capillary pressure, respectively. Based on the Young-Laplace equation the capillary pressure is defined according to Eq. (21):

$$\Delta p_c = \frac{2\gamma \cos(\theta)}{r_c} \quad (86)$$

Considering Eq. (85) and Eq. (86) the proportional error of the permeability calculation e_k is defined as follows:

$$e_k = \frac{k_x - k_{x,c}}{k_{x,c}} = \frac{\Delta p_c}{p_{in}} = \frac{2\gamma \cos(\theta)}{p_{in} \cdot r_c(\phi)} \quad (87)$$

Analyzing the influencing factors based on Eq (87) the size of the error depends on the test fluid properties (surface tension γ and contact angle θ), the inlet pressure p_{in} and the capillary radius r_c . The consideration of Eq. (85) and Eq (87) gives the following term for the corrected permeability value which includes the presence of the capillary pressure at the flow front.

$$k_{x,c} = \frac{k_x}{(1 + e_k)} \quad (88)$$

The error analysis is exemplarily done for the k_1 permeability of the W400 fabric. The analysis based on a prediction of the fluid dependent factor $\gamma \cos(\theta)$ for the used plant oil which is estimated to 30 mN/m. This value corresponds with a surface tension of approximately 33-34 mN/m, based on the results from Esteban for different plant oils [169], and an estimated contact angle in a range between 25°

and 30°. The comparison of the permeability values k_x and $k_{x,c}$ is depicted in Figure 71. Considering the mean values for the different conducted test configurations, the maximal error is in the range between 4% and 5%.

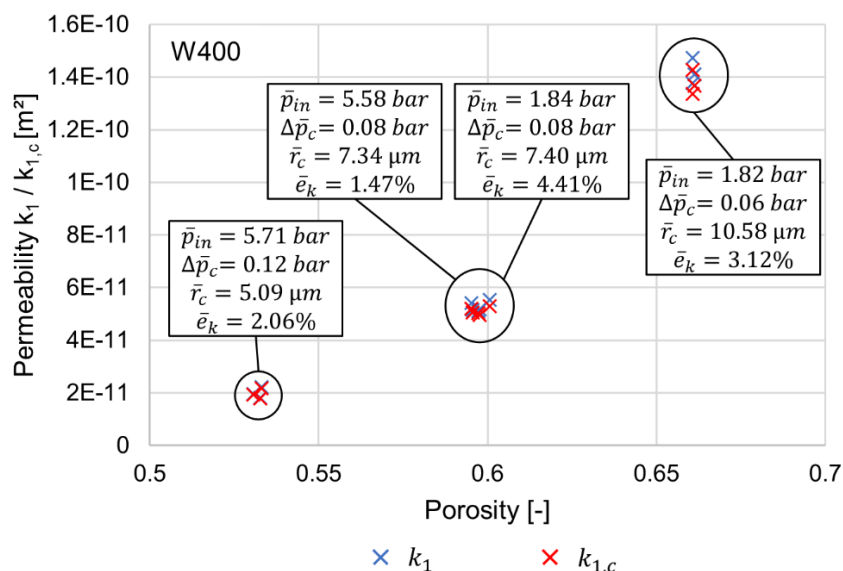


Figure 71: Resulting k_1 permeability values of the W400 fabric with and without consideration of capillary pressure

Based on the derived results it can be stated that the significance of capillary pressures on the permeability characteristics depends on the accuracy requirements and obviously on the overall accuracy of the experimental permeability determination. In this context the presented analysis allows the calculation of the error by including the results from the capillary rise experiments. The findings from Amico [142] and Francucci [143] on the influence of capillary pressures on the permeability of woven glass fiber and jute fiber fabrics confirm the present dependencies. The corresponding errors due to the neglect of the capillary forces are in both studies considerably higher compared to the measured deviations in the present work. This is in accordance with the respective experiment settings, in particular the application of significantly lower injection pressures which increases the error, according to Eq. (87). This supports the overall finding that the influence of capillary pressures depends on the specific test scenario. Therefore, the capability to determine the influence and deviations due to capillary pressures helps to provide a higher accuracy for the permeability characterization of reinforcing textiles.

6 Analysis of flow-induced voids in resin transfer molding processes

The objective in this chapter is the characterization of the composite material manufactured in RTM processes with varying impregnation velocities. This includes the analysis of the resulting void content as well as their impact on the mechanical properties, which is determined via density measurements and 3-point-bending tests, respectively. The laboratory RTM test series connects the characterization approaches for the permeability and capillary properties and validates the optimization approaches for optimal impregnation conditions based on a representative industrial LCM process.

6.1 Experimental setup

The manufacturing of the composite samples is done using a two-parted RTM tool with integrated tempering channels and a plane cavity with length and width dimensions of 270 mm x 270 mm and a height of 4 mm. The tool is installed in a mold carrier LZT-OK-80-SO from Langzauner GmbH (Austria) and the temperature is controlled with the temperature control unit Thermo-5-HB-180Z2 from HB-Therm AG (Switzerland). The upper mold allows the integration of tool-mounted sensors which is used to install three pressure sensors (KE2-6-M-B05D-1-2-E-S from Gefran S.p.A., Italy) along the centerline of the resin flow path. Additionally, a Pt100 temperature sensor, which is part of a tool-mounted direct current sensor from Synthesites Innovative Technologies Ltd (Greece), is positioned at the resin inlet side. In Figure 72 a) the schematic configuration of the RTM tool cavity with the installed sensors is depicted. The pressure sensors are used to detect the resin flow during the impregnation since the flow front arrival leads to a signal increase due to the hydraulic injection pressure. With the two-component injection unit Nodopur VS-2K from Tartler GmbH (Germany) the resin and the hardener component of the epoxy thermoset system are dispensed, mixed with a static mixer and injected in the resin inlet of the mold at a preset mass flow rate. The injection unit also allows the preheating of the resin component which is used to minimize the temperature

difference between the mixed resin and the mold. The temperature settings are defined to attain an isothermal target temperature of 70°C. A resin distribution channel at the inlet allows the resin to spread quickly along the cavity width, which is intended to ensure a uniform, one-dimensional resin flow along the preform length until the venting points are reached. The textile cuttings for the preform stacks have dimensions of 265 mm x 265 mm to fit properly in the cavity while the gaps between the left and right preform edges and the cavity are filled with sealing tape to prevent any race tracking effects. The resin system used for the test series is the epoxy resin/hardener system Epinal LR80 A2.01/Epinal LH80 B2.00 from bto epoxy GmbH (Austria), which was introduced in chapter 3.2. A release agent ACMOScoat for polyester and epoxy resins from Acmos Chemie KG (Germany) is preliminarily applied on the surfaces of the tool cavity.

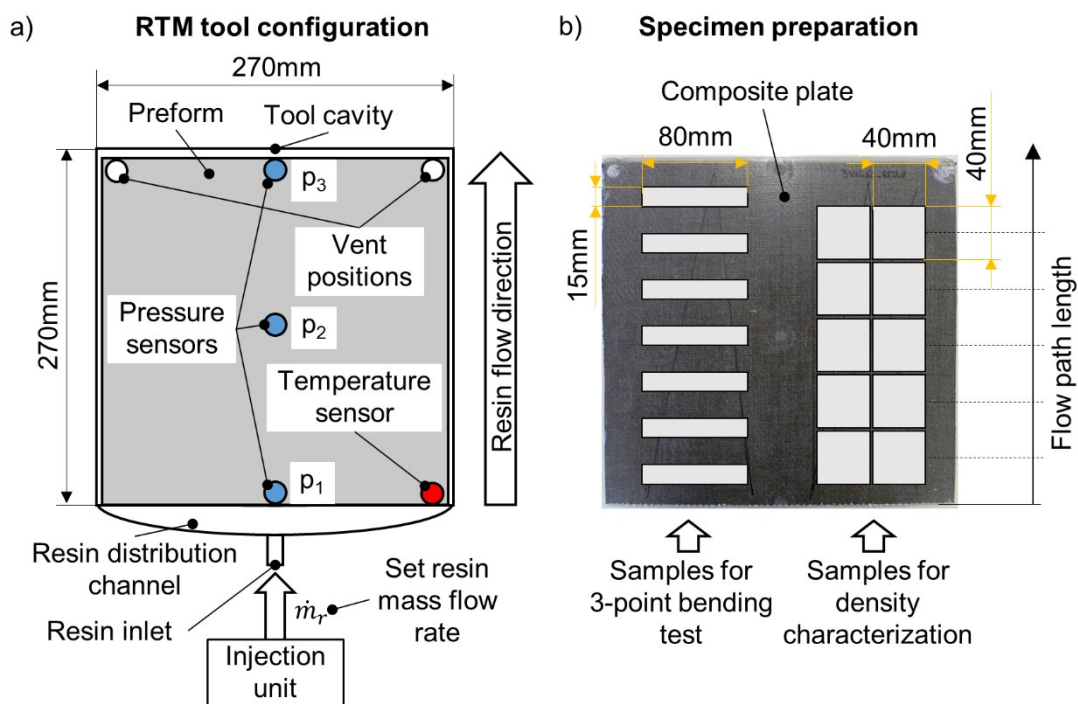
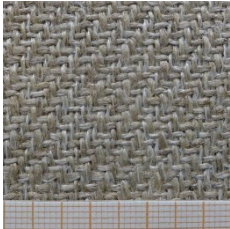



Figure 72: Overview of the experimental test setup for the RTM process (a)) and specimens used for the material characterization (b))

The different composite configurations which are manufactured and characterized are shown in Table 12. The W400 woven fabric and the UD300 textile with a unidirectional yarn orientation are considered, both with an orientation of 0° with respect to the resin flow direction. The preforms preparation considers two different

fiber volume contents, respectively, which are set by the number of layers used for the preform stack. Prior to the processing, the textile cuttings are dried in a convection oven (Model FDL 115, Binder GmbH, Germany) at 110°C to reduce any moisture related effects on the test results. The mass flow rate and therefore the impregnation velocity, are varied in a range between 150 g/min and 600 g/min, whereby the lower and the upper limit are restricted due the bottom limit of the injection unit and with regard to the necessary injection pressures, respectively.

Table 12: Test configurations specified by the fabric type, the number of layers and the resin mass flow rate used during the injection

Fabric type	
W400-0°	UD300-0°
	
5L 150 g/min 600 g/min	10L 150 g/min 600 g/min
6L 150 g/min 300 g/min 450 g/min 600 g/min	12L 150 g/min 375 g/min

Particular attention is paid do maintain consistent process conditions throughout the test series. This concerns the amount of resin used for the manufacturing of the composite plates. The injection is stopped manually after a certain fluid level inside the transparent venting tubes is reached and no significant air contents are flushed out, which typically appears shortly after the venting points are reached due to air entrapments in the rear section of the cavity. The corresponding resin masses, which are determined based on the recorded injection time and the set mass flow rate are depicted in the diagram of Figure 73. The amount of resin used for the RTM processes are in the range between 295 g and 376 g with the exceptions of two

injections with a flow rate of 600 g/min, due to slightly longer injection times which was needed to flush out entrapped air volumes in both cases. Besides the total resin masses, the excess resin content is depicted in Figure 73, too, which is defined as the proportion of the injected excessive resin volume used for flushing, with respect to the free volume inside the mold cavity. These values are in the range between 20% and 50% except for the two experiments mentioned before. The double W400-0°-5L configuration with 150 g/min flow rate is considered to check to reproducibility of this experimental approach on the evaluation results.

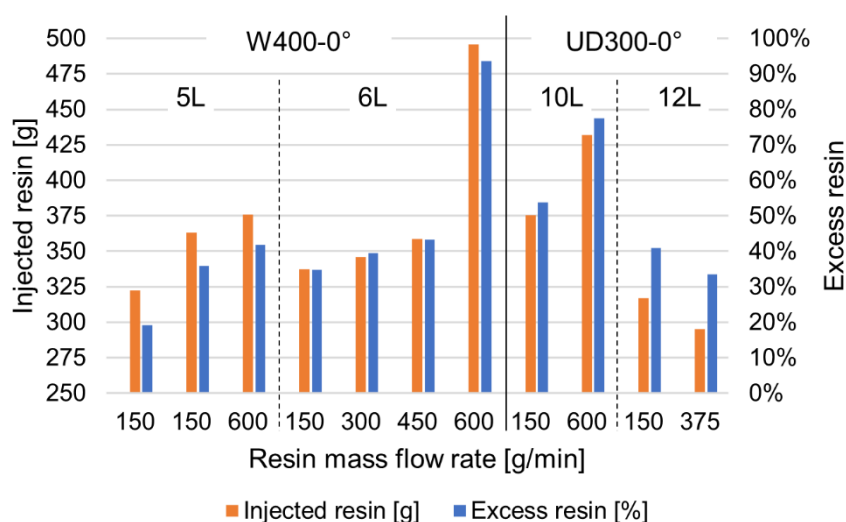


Figure 73: Overview of the injected amount of resin

By stopping the injection process any pressure is removed from the cavity. Therefore, the cure process takes place at atmospheric pressure. The demolding of the composite plates is made after at least 90 min cure time at 70°C. A subsequent temper process in a convection oven (ITHL Type from DBK David+Baader GmbH, Germany) for 24 h at 70°C with all test plates ensures a practically full cure state, regarding the cure characterization which was done on that resin system in the course of an associated research project [170]. For the characterization of the composite materials in terms of mechanical properties and impregnation quality, specimens are cut out from the test plates as illustrated in Figure 72 b).

The conduct of 3-point-bending tests is done in accordance to the test standard DIN EN ISO 14125 [171] using a Zwick Z250 universal test machine from Zwick/Roell GmbH & Co KG (Germany) with a 10 kN load cell installed. The specimen dimensions correspond to the preferred geometry class II of the test

standard with a length, width and thickness of 80 mm, 15 mm and 4 mm, respectively. The actual mean plate and specimen thicknesses are in the range between 4.16 mm and 4.42 mm. Thickness variations are present due to influences of the sealing in the mold parting line which cause a deviation from the originally intended cavity height. Therefore, the actual measured values are considered for the evaluation of the corresponding test results.

The determination of the pore content inside the composite material is oriented towards the procedure described in the standard test method ASTM D2734 [172]. Differing from the description in the test standard the resin content in the composite is not determined based on the ignition loss of cured reinforced resins (ASTM D2584). The determination of the resin mass is alternatively done using the weight difference of the composite and the calculated fiber mass based on the sample size and the areal weight of the installed preform. The fiber density is corrected considering the moisture removal due to the preparatory drying process. The density measurements on the pure resin and the composite samples are conducted using an analytical balance AG204 DeltaRange and the auxiliary Density Determination Kit from Mettler-Toledo AG (Switzerland). The specimen size used for these measurements is 40 mm x 40 mm. To avoid any fluid intake during the weight measurement in distilled water the cutting edges of the samples are preliminarily sealed with the same epoxy resin as used for the impregnation. The specimen positions on the composite test plate, as it is depicted in Figure 72 b), are marked which allows the consideration of the flow distance on the evaluated results.

6.2 Test results

6.2.1 Impregnation velocities

In the following, the actual flow velocity of the resin system during the textile impregnation according to the set process parameters is analyzed. Therefore, the theoretical fluid progress inside the porous textile preform and the measured values based on the detection of the flow front arrival on the pressure sensors are compared. For the calculation of the theoretical pore velocity $v_{p,th}$ a uniform

progression and a complete filling of the porous spaces is supposed which gives the following equation:

$$v_{p,th} = \frac{\dot{V}_m}{X_p} = \frac{\frac{\dot{m}_m}{\rho_m}}{\phi \cdot w \cdot t} = \frac{\frac{\dot{m}_m}{\rho_m}}{(1 - \phi) \cdot w \cdot t} \quad (89)$$

where X_p is the porous cross section in flow direction. X_p is assumed to be proportional to the volumetric porosity content of the preform ϕ which correlates directly with the fiber volume fraction φ inside the cavity. The variables w and t are the width of the preform and the height of the cavity, respectively. \dot{V}_m , \dot{m}_m and ρ_m are the volume flow rate, the mass flow rate and the resin density, respectively.

The fiber volume fraction φ is calculated according to Eq. (3) considering the weight and the size of the dried preform and the measured height of the composite plate. The change of the fiber density $\rho_{f,dry}$ due to the preparatory drying process is considered and corrected as follows:

$$\rho_{f,dry} = \frac{m_{f,dry}}{V_{f,dry}} = \frac{m_{f,dry}}{V_{f,0} - \frac{m_{H_2O}}{\rho_{H_2O}}} = \frac{m_{f,dry}}{\frac{m_{f,0}}{\rho_{f,0}} - \frac{(m_{f,0} - m_{f,dry})}{\rho_{H_2O}}} \quad (90)$$

where $m_{f,0}$ and $m_{f,dry}$ are the fiber weights before and after the drying process, respectively, $\rho_{f,0}$ is the initial fiber density, which is 1.50 g/cm³ analogous to the textile characterizations in the previous chapters and ρ_{H_2O} is the density of the removed moisture which is assumed to be equal to the density of water (1.00 g/cm³). The mean weight reduction due to the drying is 7.08 ± 0.81%, which results in an increase of the fiber density to 1.56 ± 0.01 g/cm³.

In Figure 74 the typical progressions of the three recorded pressure signals are depicted. The pressure values are set to zero after the preform compaction by closing the mold. Based on the detected resin arrival times the calculation of the mean flow front velocities between the sensors are determined. The initial pressure step in the flushing phase indicates a complete filling of the cavity, and excessive resin starts to stream out through the venting tubes. The final injection stop leads to a removal of the pressure since no post pressure is applied during the cure process.

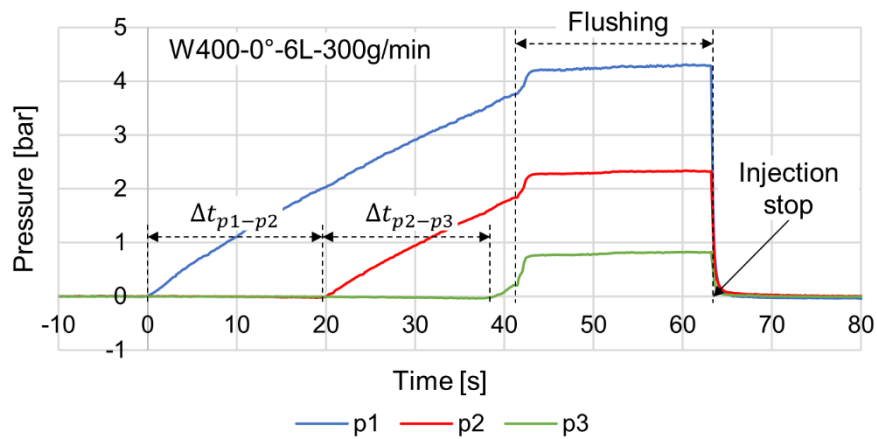


Figure 74: Pressure sensor signals during the impregnation process

The resulting velocities can be seen from Figure 75. Besides the theoretical impregnation speed according to Eq. (89) the evaluated values based on the pressure signals are depicted. While the matrix velocities between pressure sensors p1 and p3 represent the mean values along the flow path, the results between sensor 1 and 2 (p1 - p2) and sensor 2 and 3 (p2 - p3) are used to check the uniformity of the impregnation from start to end. The highest variances can be observed for the high mass flow rates which is most likely due to measurement uncertainties of the resin arrival times at the sensor positions. Considering this, the overall uniformity of the flow front velocity is consistent throughout the test series.

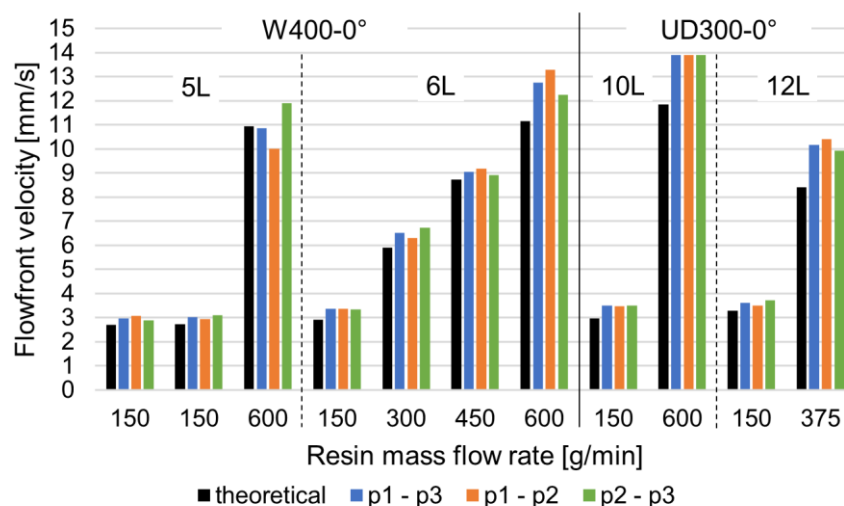


Figure 75: Resulting flow front velocities: Theoretical values and measured values based on pressure sensor signals

The resulting matrix flow velocities are in the range between 3 mm/s and 14 mm/s. Furthermore, it can be observed that the empirical velocities tend to be slightly higher than the theoretical values. This indicates that the resin flow front is obviously not a sharp line dividing the completely saturated preform and the dry reinforcement, as it is assumed for the theoretical calculation. The impregnation is rather characterized by partly saturated areas where porous spaces remain behind the flow front, which is in accordance with the expected void formation mechanisms. The interaction between the impregnation velocity and the resulting void content is presented in the following based on measurements of the resulting composite density.

6.2.2 Void contents

According to the operating instructions for the density determination [173] the specimen density ρ_{spec} is calculated as follows:

$$\rho_{spec} = \frac{m_A}{m_A - m_B} (\rho_{H_2O}(T) - \rho_{air}) + \rho_{air} \quad (91)$$

where m_A and m_B are the weights of the sample in air and immersed in the test liquid (distilled water), respectively. The density of water ρ_{H_2O} is used as given in the manual [173] which considers the temperature dependence. The variable ρ_{air} is the density of air (0.0012 g/cm³). As mentioned above, the edges of the specimens are preliminarily sealed using the same epoxy resin as used for the textile impregnation. Therefore, the volume of the composite V_c is corrected by considering the applied resin mass for the sealing $m_{m,seal}$ as follows:

$$V_c = V_{spec} - V_{seal} = \frac{m_A}{\rho_{spec}} - \frac{m_{m,seal}}{\rho_m} \quad (92)$$

where V_{spec} and V_{seal} are the volumes of the specimen and the added resin, respectively. ρ_m is the density of the epoxy resin, which was determined to 1.164 g/cm³ using the same measurement approach with cured resin specimens. The subsequent calculation of the void volume inside the composite material V_v is done according to the following equation:

$$V_v = V_c - V_f - V_m = V_c - \frac{m_{f,spec}}{\rho_{f,dry}} - \frac{(m_A - m_{m,seal}) - m_{f,spec}}{\rho_m} \quad (93)$$

$$\text{with } m_{f,spec} = \frac{A_{spec}}{A_{tex}} \cdot m_{f,dry}$$

where V_f and V_m are the volumes of the fiber and the matrix, respectively. The calculation of the fiber mass inside the specimen $m_{f,spec}$ base on the assumption of an even areal fiber distribution within the composite plate. The fiber weight is determined, considering the areal dimensions of the sample A_{spec} and the dimensions of the preform A_{tex} with the corresponding fiber weight after the preparatory drying process $m_{f,dry}$. The matrix volume is calculated based on the weight difference between the composite and the determined fiber weight. In the following, the void content inside the matrix component is analyzed which is defined as follows:

$$\varepsilon_m = \frac{V_v}{V_m} \quad (94)$$

The resulting ε_m values for the W400 fabric configurations are depicted in Figure 76.

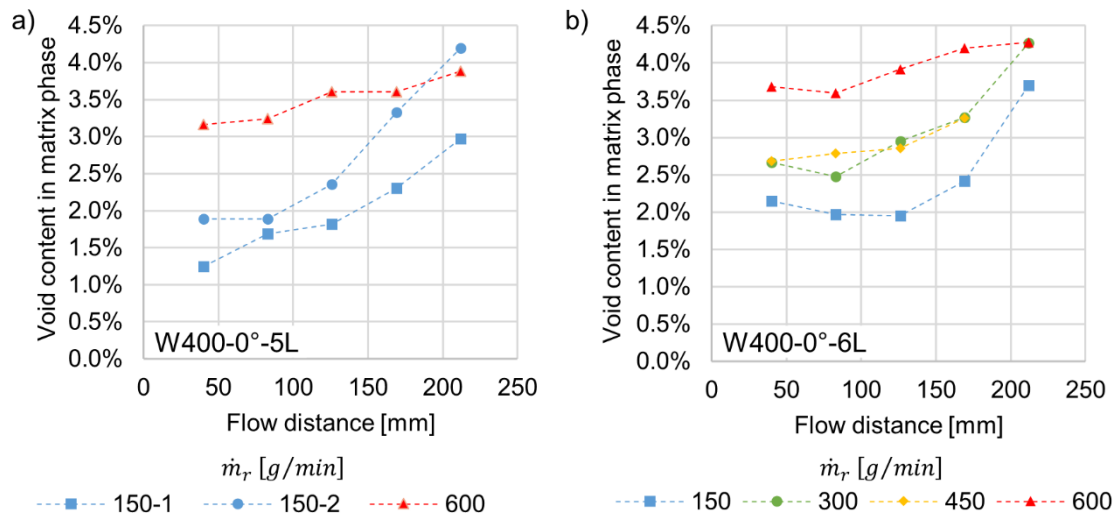


Figure 76: Void contents for the test series on the W400-0° configurations with
a) 5 layers and b) 6 layers

The results show the void contents of the specimens depending on the flow distance of the resin system, as it is depicted in Figure 72 b), which consider the mean values

of each pair of the two specimen rows. In every case the void content tends to increase with longer flow distances. In some cases, the values are stable in the first part, but the highest void contents belong always to the most distant specimens from the resin inlet. This behavior is related to the mobilization mechanisms of the entrapped voids due to the resin flow. Similar observations have been made in other studies which address the void formation in LCM processes [117], [123], [174]–[176]. It is also noticeable that slower resin mass flow rates lead to a significant reduction of the resulting void content but show the tendency for a more pronounced void increase over the flow distance compared to the higher mass flow rates. For the W400 configuration with 5 layers two plates with the same injection settings ($\dot{m}_m = 150$ g/min) were manufactured and tested. The corresponding deviations between both experiments demonstrate the unavoidable scatter of this characterization approach due to variations of the textile reinforcements, deviations during the process cycles and flow progressions and the overall measurement inaccuracies. Nevertheless, the overall relation between the impregnation velocity and the resulting void content can be confirmed. Differences due to the variation of the fiber volume fractions are less significant considering the accuracy of this characterization approach and the limited amount of test data.

The same tendencies continue for the configurations based on the UD300 fabric as can be seen from the diagrams in Figure 77.

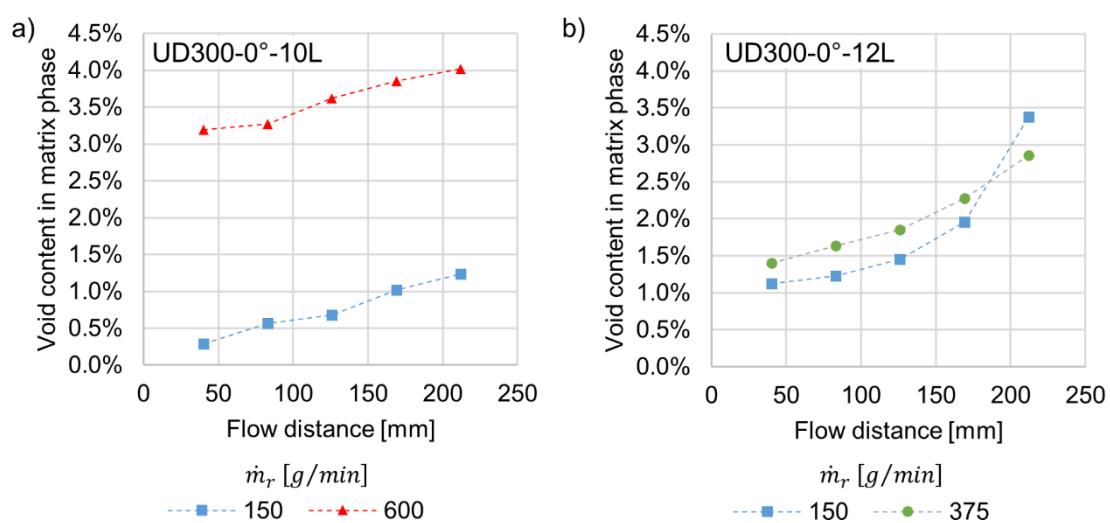


Figure 77: Void contents for the test series on the UD300-0° configurations with
a) 10 layers and b) 12 layers

While the difference between the 150 g/min and the 600 g/min resin mass flow rate for the 10-layer configurations is very pronounced the 375 g/min flow rate related to the 12-layer configuration leads to a less significant change of the resulting void content. The comparison of the 150 g/min settings between both configurations show slightly higher void values for the 12-layer configuration.

The comparison of both textiles show that the smallest void contents belong to the UD300-0°-10L configuration injected with a flow rate of 150 g/min, but the remaining void increase still indicates their formation and a subsequent mobilization during the impregnation process. Furthermore, there is a good correlation between the measured void contents and the visual appearance of the composite plates. In Figure 78 and Figure 79 sections of the density specimens from the first pair (near inlet) and the last pair (near vent) are depicted for the W400-0°-5L and the UD300-0°-10L configuration, respectively.

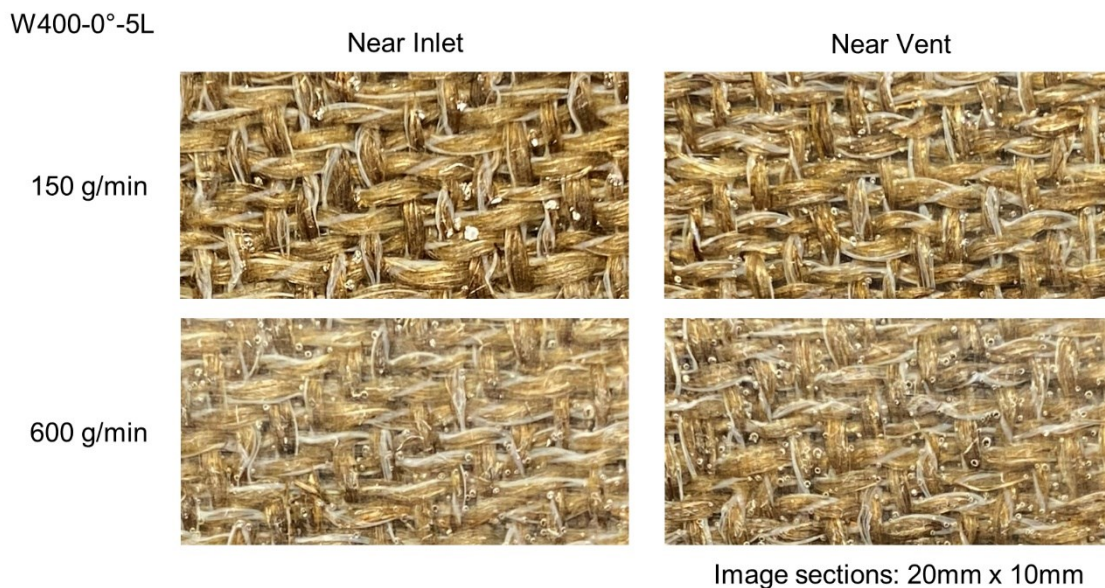


Figure 78: Visual appearance of the W500-0°-5L composite configurations

From the images it can be observed that for both fabric types the amount of visible voids in the matrix phase increase with further distance from the inlet and is generally higher for the faster impregnation settings. Although the voids are located in the visible pore spaces between the yarns it is unlikely that mechanisms related to macro void formations are responsible for the present appearance. This is assumed due to the relatively fast impregnation velocities not meeting the

requirements for the formation of macro voids. Patel, who observed visually the void formation during the impregnation in glass fiber fabrics, describes the effect of coagulating micro voids which forms larger voids outside the fiber tows [106]. An analogue mechanism in the natural fiber yarns is seen to be the reason for the resulting appearances as shown in Figure 78 and Figure 79, respectively.

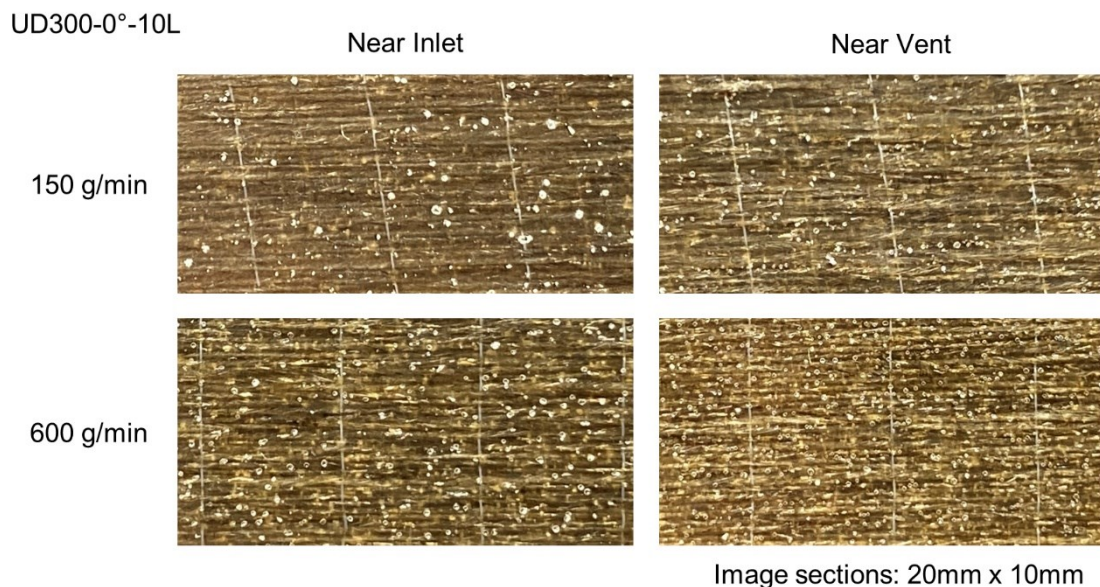


Figure 79: Visual appearance of the UD300-0°-10L composite configurations

6.2.3 Mechanical properties

The composite quality also affects the mechanical properties which can be seen from the results of the 3-point-bending tests. The resulting mean values for the bending stiffness and bending strength of the W400 test configurations are illustrated in Figure 80. The differences between the slow (150 g/min) and the fast (600 g/min) impregnation are more pronounced for the 5-layer configurations with a lower fiber volume fraction. The reduction of the bending stiffness and bending strength is 6.8% and 6.7%, respectively. Smaller changes can be observed for the higher fiber volume fraction (6L configurations). In this case the stiffness reduction between the slowest and the fastest resin flow rate is 2.2%, while the bending strength reduces by 2.6%. An exception of the decreasing tendency can be observed for the bending strength of the 450 g/min setting. The bending properties are mainly influenced by the textile reinforcement which explains the higher

mechanical properties for the 6-layer configurations. The higher variances of the strength values compared to the stiffness properties are in accordance with previous studies which subject the influence on voids on the mechanical properties [177].

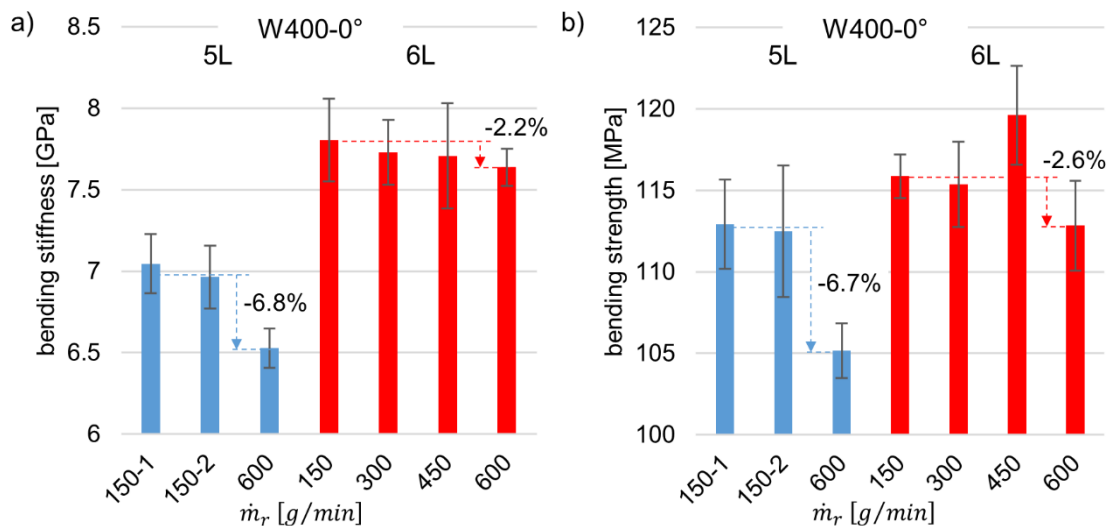


Figure 80: Bending stiffness (a) and bending strength (b) for the test series on the W400-0° configurations

The tendency for the reduction of the mechanical properties with faster impregnation velocities is also present for the UD300 fabric as it is shown in the diagrams of Figure 81.

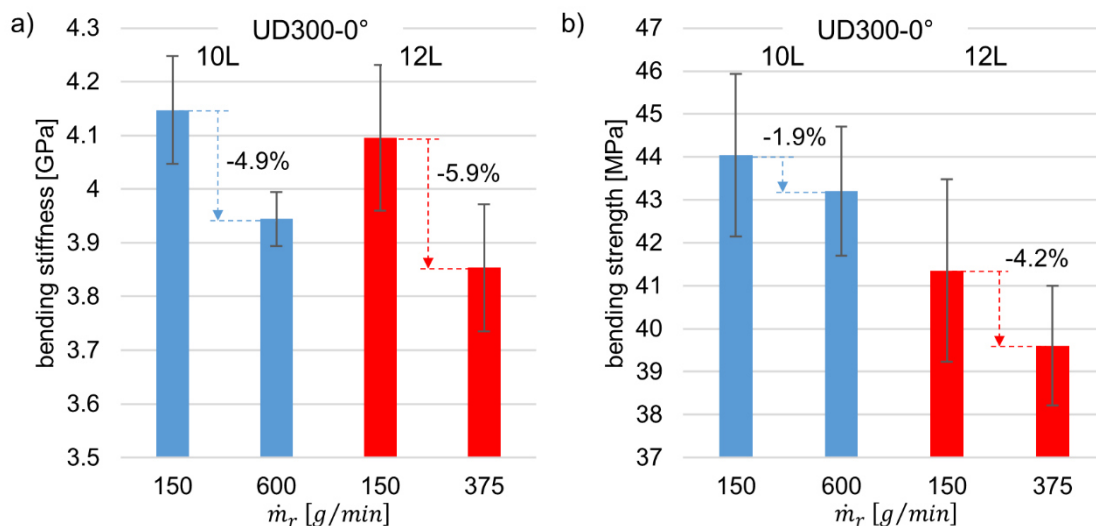


Figure 81: Bending stiffness (a) and bending strength (b) for the test series on the UD300-0° configurations

The bending test specimens were oriented perpendicular to the yarn orientation as it is depicted in Figure 72 b) to specifically evaluate the resin properties. The stiffness reduction related to the considered process settings is 4.9% and 5.9% for the 10-layer and 12-layer configuration, respectively, while the bending strength decreases by 1.9% and 4.2%, respectively.

The analysis of the mechanical composite properties confirms the variances and tendencies due to the variation of the impregnation conditions which became apparent from the void content determination. This indicates that suitable process settings for the impregnation of the textile reinforcement can improve the resulting quality of the composite in terms of their mechanical performance. Besides the quasi-static bending properties more crucial and detrimental effects can be expected for the inter-laminar shear, compression and dynamic fatigue properties of the composite material, which were found to be the most critically affected properties due to voids [20].

6.3 Discussion

In the following, the obtained results from the void content measurements are analyzed in context to the derivation of optimal impregnation velocities. The objective is the derivation of optimal capillary numbers for the considered reinforcing textiles based on the analytical optimization approach, as applied in chapter 5.4.1. In addition, further influencing factors of the LCM process on the resulting void content and appropriate measures for improvement are discussed.

6.3.1 Application of the Capillary number optimization approach

To compare the impregnation velocities used in the RTM test series with the optimal capillary numbers, as derived in chapter 5.4.1, the penetrativity P of the epoxy resin system is used considering the given relationship, according to Eq. (81):

$$v_p = P \cdot Ca^* = \frac{\gamma \cos(\theta)}{\eta} \cdot Ca^* \quad (95)$$

The surface tension γ and the contact angle θ are again estimated based on the literature data at 40 mN/m and 55°, respectively, analogous to the definition in

chapter 5.3.2. The viscosity is defined according to the viscosity measurements to 30 mPa·s, considering the recorded resin temperatures during impregnation which are in the range between 66°C and 72°C. A dynamic viscosity increase is not considered in this context since the impregnation time is under 100 s for all configurations which corresponds to an insignificant change in viscosity for the following evaluation considering the overall accuracy of this input value. The corresponding resin penetrativity is then 0.765 m/s. The diagram in Figure 82 illustrates the current situation for the W400 configurations. The depicted datapoints show the evaluated flow front velocities during impregnation and the resulting mean void contents of the composites, respectively. The lines show the derived optimal impregnation velocities with respect to the underlying characteristic mesoscopic length L_c over the considered porosity range.

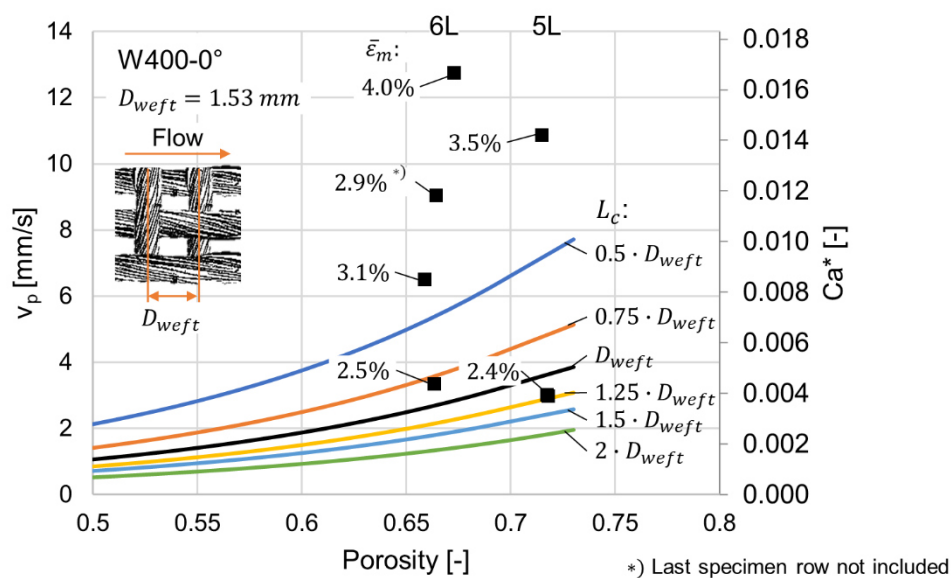


Figure 82: Comparison of the impregnation velocities during experiment and the derived range of optimal capillary numbers for the W400 configurations

As can be seen from Figure 82, the lowest impregnation velocities are within the range of estimated optimal conditions. This correlates with a mesoscopic length around the yarn distance D_{weft} as it was also used for a glass fiber NCF in the course of the studies from LeBel, Causse and Ravey [119], [122], [123]. Regarding the void formation mechanism, as depicted in Figure 23 a), it is assumed that macrovoids will not be a critical factor as long as the distance between the primary

flow front and the wicking flow front is no longer than the yarn distance D_{weft} . This applies for impregnation velocities which correlate with a mesoscopic length of $2 \cdot D_{weft}$, according to Eq. (61). Therefore, a mesoscopic length in a range between $1.25 - 2 \cdot D_{weft}$ is assumed to result in minimal flow-induced void contents. This is in accordance to the results from Causse [123] who also found the optimal impregnation velocities close to the lower bounds of the predicted range, thus generally lower velocities than the prediction based on a mesoscopic length of $1 \cdot D_{weft}$. In the present case, the related optimal modified capillary numbers are therefore in the range between 0.001 up to 0.004 depending on the actual porosity state.

The diagram in Figure 83 depicts the situation for the UD300 textile configurations. Since the characteristic mesoscopic length L_c is not defined in the same manner as in case of the woven fabrics the variable was varied with respect to the mean yarn distance oriented in flow direction. This was done with the intention to ensure a suitable scale for the present evaluation. The results indicate that a mesoscopic length L_c of approximately $6 \cdot D_{yarn}$ to $8 \cdot D_{yarn}$ seems to be reasonable to define suitable impregnation conditions with a minimal content of flow-induced voids.

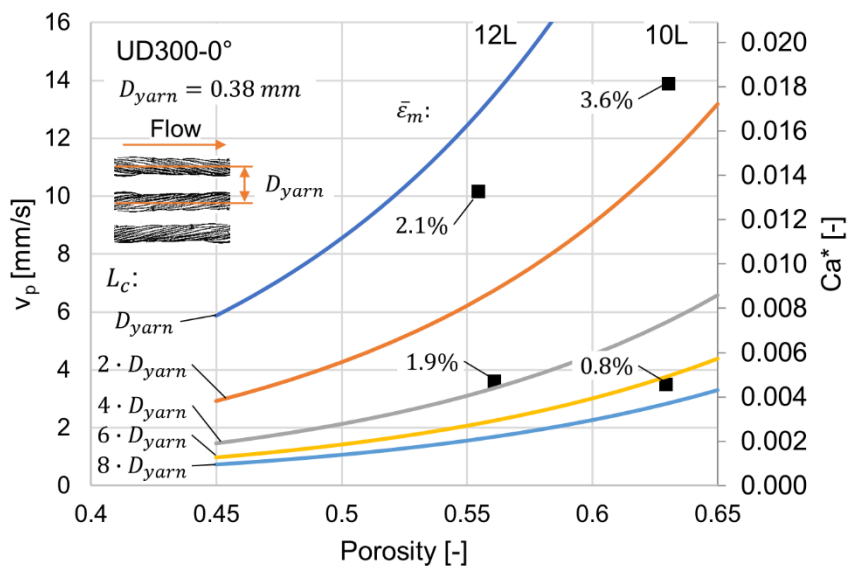


Figure 83: Comparison of the impregnation velocities during experiment and the derived range of optimal capillary numbers for the UD300 configurations

Although this length scale cannot be used as a general rule to predict an appropriate distance for the characteristic mesoscopic length, it can be observed that the resulting range for Ca_{opt}^* is similar to the one obtained for the W400 fabric. This might indicate that appropriate impregnation velocities commonly correlate with capillary numbers in the range of 0.001 to 0.005, which gives an orientation in the first instance. Dependent on the present porosity state the choice for the specification of the impregnation velocity is then on the lower or upper bound of this range.

Limitations for optimal flow conditions

In the following example, the effects due to the dynamic penetrativity change of the reactive resin system during the processing shall be discussed. This is of particular interest in case of longer injection times or fast curing systems. In this scenario a viscosity increase over time is considered corresponding to an isothermal cure temperature of 70°C for the used epoxy resin system, while the contact angle and the surface tension are assumed to remain constant. The pressure gradient for a one-dimensional flow, according to Eq. (11), is given as follows:

$$-\frac{dp}{dx} = v_{p,x} \cdot \frac{\phi \cdot \eta}{k_x} \quad (96)$$

where $v_{p,x}$ is the impregnation velocity, ϕ the preform porosity, η the dynamic resin viscosity and k_x the textile permeability in x-direction. Inserting Eq. (95) in Eq. (96) gives the following equation:

$$-\frac{dp}{dx} = Ca_{opt}^* \cdot \frac{\phi}{k_x} \cdot \gamma \cos(\theta) \quad (97)$$

From Eq. (95) it is apparent that an increasing viscosity leads to a decrease of the flow front velocity when optimal conditions shall be maintained. Figure 84 a) shows the corresponding velocity progressions for different underlying capillary numbers in the range between 0.002 and 0.004. The velocity reduction leads to a flow distance limit that can be achieved under optimal impregnation conditions. The maximal flow length can be seen from Figure 84 b) which also illustrates the progressions for the corresponding injection pressures. The latter depend on the

defined capillary number but also from the preform permeability, according to Eq. (97).

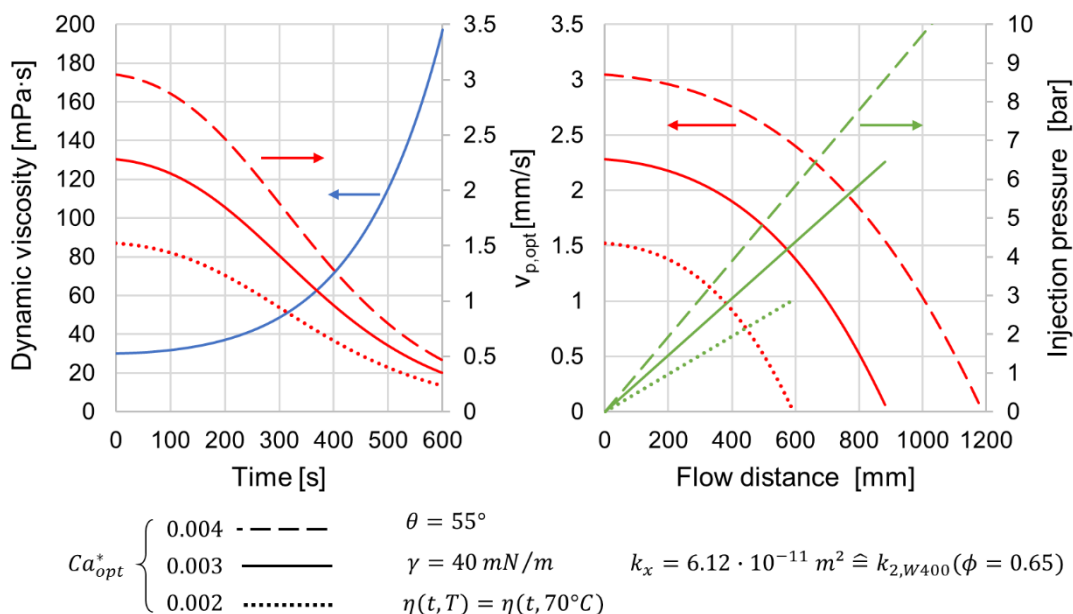


Figure 84: Influence of Ca_{opt}^* on the impregnation velocity and injection pressure progression considering an increasing resin viscosity

This example connects in this simple one-dimensional scenario the results from the permeability characterization and the optimization approach based on the capillary properties of the reinforcement. In context to an optimal process design, possible limitations related to the impregnation strategy and the characteristics of the thermoset resin system can be detected and the requirements for the injection unit and tool properties can be evaluated.

Besides the direct influence of the impregnation velocity, various other factors which affect the composite quality in terms of void formation are discussed in the following and appropriate measures for improvement are presented. This allows the consideration of further options to optimize the LCM process design in terms of void minimization.

6.3.2 Appropriate measures for void reduction

Based on the results from the RTM test series the appropriate adjustment of the resin flow velocity during the impregnation is a relevant factor for the void formation, thus the quality of the resulting composite material. However, the observations from the investigation of the capillary characteristics indicate that the complex pore morphology in common natural fiber reinforcements causes a void formation to a certain extent even at or close to the optimal impregnation velocities. This is due to the variances of the spontaneous capillary driven fluid flow inside the irregular pore structure, which cannot be influenced by the applied pressure or mass flow settings. Beyond this point, the resulting voids are affected by mobilization mechanisms which results in a characteristic increase of the void concentration along the flow path, which is apparent even at low total void contents. The following points consider further influencing factors related to void formation and address suitable measures for improvement.

Textile architecture and pore morphology

Considering the observed time lag between the capillary fluid rise and the peripheral saturation of pore spaces behind the flow front, as presented in chapter 5.2.2, significant differences between the textile architectures in terms of their fluid imbibition characteristics were identified. The extended fluid flow in saturated areas can be seen as a measure for the evenness of the capillary driven wicking process. In this context, the results in Figure 45 indicate the corresponding behavior of the tested fabrics. A pronounced peripheral flow is present for the W400 woven fabric but also for the non-woven fabric NW300, due to the delayed saturation of pore spaces inside the perpendicular yarn system and irregularities in the pore size distribution, respectively. The unidirectional fabric UD show a tendency for a more uniform fluid progression with decreasing porosity contents, which is the results of a smaller pore size distribution at higher compaction states. Therefore, it can be stated that depending on the fabric and preform architecture and the actual compaction state the proneness for void formation varies, even with optimal impregnation conditions. In the studies from Lundström [174] and Sisodia [178] the void formation on fiber bundles with different orientations to the flow direction were analyzed. The results show an increasing tendency in obliquely oriented fiber

bundles, thus confirm the dependence of the actual fiber architecture and layup on the resulting voids content. Therefore, the characterization of the capillary properties for different fabric architecture and layups can give valuable information according to their characteristics during saturation and vulnerability to void formation.

Flow distances during injection

Considering the trend of an increasing void content along the fluid flow path it is obvious that a reduction of the impregnation length has a positive effect in terms of void minimization. This is a measure which is generally considered during the design of suitable injection strategies for the respective composite part. In terms of void minimization, a shorter flow distance also allows the impregnation at lower impregnation velocities and allows better consideration of the derived optimal impregnation settings. Therefore, this measure is of particular importance since it enables the effective reduction of void contents and/or impregnation times.

Void mobilization

Due to the variances of pore sizes and based on the experimental observations in the present work it is unlikely that flow-induced voids can be completely avoided by optimal impregnation velocities. The void content can be significantly reduced under optimal conditions, but the formation to a certain extent still leads to the gradual void increase along the impregnation length. An extension of the flushing phase, thus longer times for void mobilization, might lead to a reduction of the void content but the necessary amount of excessive resin must be considered in this context for economic and ecological reasons. Based on the void mobilization model from Patel [106] and the observations from Chen [113] and Park [115], the mobilization of voids depends on a critical capillary number, thus high viscous forces, which correlate with a fast fluid flow. Therefore, a saturation with a lower, optimal impregnation velocity followed by a short and fast flushing phase is presumably a suitable strategy for an effective removal of remaining voids without wasting an excessive amount of resin. In this context, LeBel mentioned the 'pack and bleed' strategy which considers a sequence of a pulsing resin inlet pressure after the impregnation during the flushing phase for an efficient void mobilization. This approach was already successfully proven in industrial RTM processes [176].

Post-filling pressure during cure reaction

Considering the pressure state not just during the processing of the liquid resin system but also during the subsequent cure reaction, an applied post pressure effectively reduces the void volume in the final composite material. The results based on the experimental series from Lundström [174] and LeBel [176] show a significant influence of the cure pressure on the resulting void content. Therefore, the application of a post pressure is seen as an obligatory measure to achieve optimal composite qualities in addition to the preparatory minimization of flow-induced voids during the impregnation process.

Vacuum assistance

A further strategy to achieve an improvement of the composite quality in RTM processes is the application of a vacuum pressure on the venting side of the tool cavity. This measure is intended to remove the air from the porous preform before filling with the matrix component and has been proven to efficiently decrease the void content inside the composite part [174], [179]. A potential risk in connection with this strategy are the detrimental effects in case of leakages between the evacuated cavity and the surroundings due to inflowing air. Furthermore, the interactions between the vacuum pressure and a potential formation of volatiles due to degassing effects in the liquid resin or due to the residual moisture contents in the natural fibers should be considered [19].

The variety of approaches for the optimization of the preform impregnation allows a suitable design of the RTM process with respect to the individual case. Considering the influencing factors like the geometry and dimensions of the composite part, characteristics of the thermoset resin system and properties of the processing equipment and tooling, the appropriate application of selected measures allows an effective reduction of the void content in the final product.

7 Summary and Conclusion

The use of natural fibers for fiber reinforced polymer composites experienced growing interest over the past years. As an ecological-friendly alternative to synthetic fiber reinforcements this renewable resource profits from a growing environmental awareness. Besides the primary used manufacturing method via compression molding for non-structural components, recent developments consider the application of liquid composite molding (LCM) techniques like Resin Transfer Molding (RTM) to produce NFRP parts with higher load-bearing capacity and resilience. In this context the impregnation process of the textile reinforcements is a crucial factor regarding the resulting part quality, due to the presence of flow-induced void formation during the saturation with the liquid matrix system.

The main objective in the present work is the development of a methodical approach to derive optimal impregnation velocities for natural fiber reinforcements in LCM processes. Therefore, the mechanisms related to the fluid flow through different flax fiber fabrics were investigated considering the analysis of the permeability characteristics as well as the capillary action inside the porous structure. The latter was done with particular attention on capillary rise experiments, including the development of a test stand which enables the characterization of the material in a defined compacted state and similar to the situation in the real manufacturing process. Based on the observations and test results a new model approach for the dynamic capillary driven flow was derived and applied which considers a peripheral fluid flow behind the visible flow front. This model allows an accurate representation of the textile-specific capillary action. The evaluation results were used to apply an optimization approach for the evaluation of optimal impregnation velocities which considers the concurrent presence of viscous and capillary forces at the flow front.

The derived optimization results were further analyzed and verified based on an RTM test series with varying impregnation velocities. A reasonable consistency in connection with the measured void contents inside the composites was identified which indicates the overall applicability of the presented methodical approach for the derivation of optimal impregnation conditions.

Further benefits result from the utilization of the capillary characterization to improve the accuracy of the permeability determination by considering the capillary pressure component at the moving flow front during saturation.

Nevertheless, there were some issues identified which leaves room for improvement and further investigations:

The optimization approach for optimal impregnation velocities includes a textile-specific length scale, the characteristic mesoscopic length, which is related to the unit cell size of the fabric structure. For some flow scenarios and fabric types (woven fabrics, bidirectional NCFs) such characteristic dimensions are clearly defined, while in others (random fiber mats, unidirectional fabrics) the necessary information is not directly provided. Since similar mechanisms for the flow-induced void formation are present within all fabric types, a suitable approach should be derived which takes the differences of the textile architectures into account.

In context to this issue further investigations on the capillary action inside different reinforcements can be conducted to obtain more information related to the present flow situation. This refers on the one hand the further development of the experimental approaches, including the test setup, sensing technologies and data evaluation and on the other hand the model derivation to describe the capillary effects during saturation. Although the used model approach for the capillary rise, which considers a peripheral fluid flow through the porous capillary tube, demonstrated good results there are some relevant effects still unconsidered.

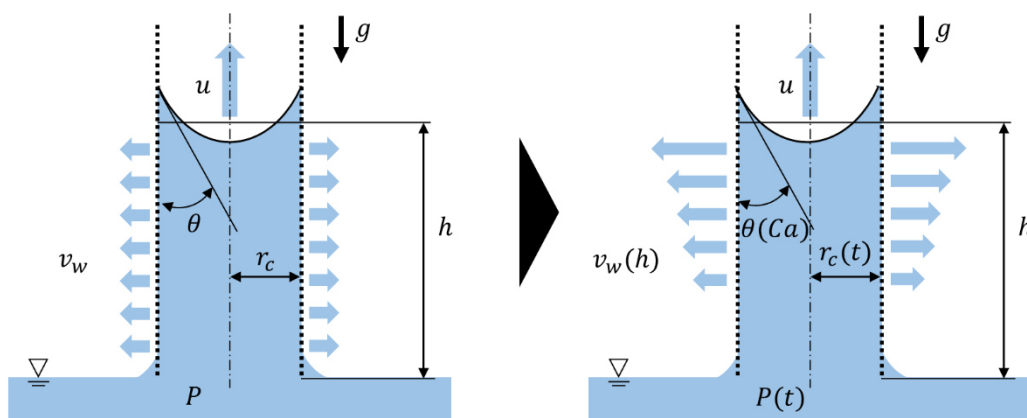


Figure 85: Possible adjustments related to the porous tube model approach for further investigations

In Figure 85 exemplary modifications are schematically depicted with respect to the actual state of the derived model approach. This includes for instance the consideration of the dynamic behavior of the contact angle, the fluid penetrativity and capillary radii, the change of fluid properties during flow (dynamic viscosity, surface tension) and fiber swelling effects. A further detailed analysis on the peripheral fluid flow could also improve the accuracy of the model which results in an enhanced understanding of the fluid flow processes inside the porous spaces. In this regard, the results, findings, and approaches of the present work provide relevant findings and information which can be used in future studies.

Literature

- [1] Lässig, R., Eisenhut, M., Mathias, A., Schulte, R.T., Peters, F., Kühmann, T., and Begemann, W.: Serienproduktion von hochfesten Faserverbundbauteilen: Perspektiven für den deutschen Maschinen- und Anlagenbau. Roland Berger Strategy Consultants (ed.), 2012.
- [2] Witten, E., Mathes, V., Sauer, M., and Kühnel, M.: Composites-Marktbericht 2018: Marktentwicklungen, Trends, Ausblicke und Herausforderungen. AVK Industrievereinigung verstärkte Kunststoffe, CCeV Carbon Composites eV (ed.), 2018.
- [3] Carus, M. and Partanen, A.: Bioverbundwerkstoffe: Naturfaserverstärkte Kunststoffe (NFK) und Holz-Polymer-Werkstoffe (WPC). Fachagentur Nachwachsende Rohstoffe e.V. (ed.), 2019.
- [4] Bioeconomy: A Strategy for Austria. Federal Ministry for Sustainability and Tourism (BMNT), Federal Ministry of Education, Science and Research (BMBWF), Federal Ministry for Transport, Innovation and Technology (BMVIT) (eds.), Vienna, 2019.
- [5] Bioeconomy in Germany: Opportunities for a bio-based and sustainable future. Federal Ministry of Education and Research (BMBF), Federal Ministry of Food and Agriculture (BMEL) (eds.), Bonn, Berlin, 2015.
- [6] Nationale Bioökonomiestrategie. Bundesministerium für Bildung und Forschung (BMBF), Bundesministerium für Ernährung und Landwirtschaft (BMEL) (eds.), Berlin, 2020.
- [7] Rahman, M.A., Parvin, F., Hasan, M., and Hoque, M.E., "Introduction to Manufacturing of Natural Fibre-Reinforced Polymer Composites," in *Manufacturing of Natural Fibre Reinforced Polymer Composites*, Salit, M.S., Jawaid, M., Yusoff, N.B., and Hoque, M.E. (eds.), Springer International Publishing, Cham, 2015.
- [8] Faruk, O., Bledzki, A.K., Fink, H.-P., and Sain, M.: Progress Report on Natural Fiber Reinforced Composites, *Macromol. Mater. Eng.*, 299, 2014, 9–26.

- [9] Pickering, K.L., Efendy, M.A., and Le, T.M.: A review of recent developments in natural fibre composites and their mechanical performance, *Composites Part A: Applied Science and Manufacturing*, 83, 2016, 98–112.
- [10] Rana, S., Pichandi, S., Parveen, S., and Fanguero, R., “Natural Plant Fibers: Production, Processing, Properties and Their Sustainability Parameters,” in *Roadmap to Sustainable Textiles and Clothing*, Muthu, S.S. (ed.), Springer Singapore, Singapore, 2014.
- [11] Joshi, S.V., Drzal, L.T., Mohanty, A.K., and Arora, S.: Are natural fiber composites environmentally superior to glass fiber reinforced composites?, *Composites Part A: Applied Science and Manufacturing*, 35, 2004, 371–376.
- [12] Shah, D.U., Schubel, P.J., and Clifford, M.J.: Can flax replace E-glass in structural composites? A small wind turbine blade case study, *Composites Part B: Engineering*, 52, 2013, 172–181.
- [13] Mathijssen, D.: The renaissance of flax fibers, *Reinforced Plastics*, 62, 2018, 138–147.
- [14] Riedel, U., “Biocomposites: Long Natural Fiber-Reinforced Biopolymers,” in *Polymer Science: A Comprehensive Reference*, Elsevier, 2012.
- [15] Bioconcept-Car: Basisinformationen. Fachagentur Nachwachsende Rohstoffe e.V. (ed.), 2013.
- [16] Hansen, O., Ganter, N., and Becker, N.: Naturfaserverstärkte Kunststoffe als Baustein einer nachhaltigen Mobilität?, *ATZ Prod*, 7, 2020, 48–51.
- [17] Flemming, M., Ziegmann, G., and Roth, S.: *Faserverbundbauweisen: Fertigungsverfahren mit duroplastischer Matrix*, Springer Berlin Heidelberg, Berlin, Heidelberg, 1999.
- [18] Konstantopoulos, S., Hueber, C., Antoniadis, I., Summerscales, J., and Schledjewski, R.: Liquid composite molding reproducibility in real-world production of fiber reinforced polymeric composites: a review of challenges and solutions, *Advanced Manufacturing: Polymer & Composites Science*, 5, 2019, 85–99.

- [19] Hamidi, Y.K. and Altan, M.C.: Process Induced Defects in Liquid Molding Processes of Composites, *International Polymer Processing*, 32, 2017, 527–544.
- [20] Mehdikhani, M., Gorbatiikh, L., Verpoest, I., and Lomov, S.V.: Voids in fiber-reinforced polymer composites: A review on their formation, characteristics, and effects on mechanical performance, *Journal of Composite Materials*, 53, 2019, 1579–1669.
- [21] Beldzki, A. K., Sperber, V. E., and Faruk, O.: Natural and wood fibre reinforcement in polymers, Rapra Technology Ltd, Shawbury, U.K, 2002.
- [22] Baley, C.: Analysis of the flax fibres tensile behaviour and analysis of the tensile stiffness increase, *Composites Part A: Applied Science and Manufacturing*, 33, 2002, 939–948.
- [23] M. Sain and O. Faruk, Eds.: Biofiber reinforcement in composite materials, Woodhead Publishing, Cambridge, England, Waltham, Massachusetts, Kidlington, England, 2015.
- [24] Völker, U. and Brückner, K.: Von der Faser zum Stoff: Textile Werkstoff- und Warenkunde, 35. ed., Büchner Handwerk und Technik, Hamburg, 2014.
- [25] Mohanty, A.K., Misra, M., and Hinrichsen, G.: Biofibres, biodegradable polymers and biocomposites: An overview, *Macromol. Mater. Eng.*, 276-277, 2000, 1–24.
- [26] van Hazendonk, J.M., van der Putten, J.C., Keurentjes, J.T.F., and Prins, A.: A simple experimental method for the measurement of the surface tension of cellulosic fibres and its relation with chemical composition, *Colloids and Surfaces A: Physicochemical and Engineering Aspects*, 81, 1993, 251–261.
- [27] van de Velde, K. and Kiekens, P.: Wettability of natural fibres used as reinforcement for composites, *Angew. Makromol. Chem.*, 272, 1999, 87–93.
- [28] Aranberri-Askargorta, I., Lampke, T., and Bismarck, A.: Wetting behavior of flax fibers as reinforcement for polypropylene, *Journal of Colloid and Interface Science*, 263, 2003, 580–589.

- [29] Aranguren, M.I. and Reboredo, M.M., "Plant-Based Reinforcements for Thermosets: Matrices, Processing, and Properties," in *Handbook of Engineering Biopolymers: Homopolymers, Blends, and Composites*, Fakirov, S. and Bhattacharyya, D. (eds.), Carl Hanser Fachbuchverlag, 2015.
- [30] Bledzki, A.: Composites reinforced with cellulose based fibres, *Progress in Polymer Science*, 24, 1999, 221–274.
- [31] Crosky, A., Soatthiyanon, N., Ruys, D., Meatherall, S., and Potter, S., "Thermoset matrix natural fibre-reinforced composites," in *Natural Fibre Composites*, Elsevier, 2014.
- [32] Baley, C. and Bourmaud, A.: Average tensile properties of French elementary flax fibers, *Materials Letters*, 122, 2014, 159–161.
- [33] Rowell, R.M., "Natural fibers: Types and properties," in *Properties and performance of natural-fibre composites*, Pickering, K.L. (ed.), CRC Press, Boca Raton, Cambridge, England, 2008.
- [34] Jawaid, M. and Abdul Khalil, H.P.S.: Cellulosic/synthetic fibre reinforced polymer hybrid composites: A review, *Carbohydrate Polymers*, 86, 2011, 1–18.
- [35] Flemming, M., Ziegmann, G., and Roth, S.: *Faserverbundbauweisen: Fasern und Matrices*, Springer Berlin Heidelberg, Berlin, Heidelberg, 1995.
- [36] Dai, D. and Fan, M., "Wood fibres as reinforcements in natural fibre composites: structure, properties, processing and applications," in *Natural Fibre Composites*, Elsevier, 2014.
- [37] The European Confederation of Flax and Hemp (CELC): Flax and Hemp Semi-products, URL: <http://news.europeanflax.com/technique/flax-and-hemp-semi-products/> (checked on 11. January 2021).
- [38] Goutianos, S., Peijs, T., Nystrom, B., and Skrifvars, M.: Development of Flax Fibre based Textile Reinforcements for Composite Applications, *Appl Compos Mater*, 13, 2006, 199–215.
- [39] Madsen, B.: Properties of plant fibre yarn polymer composites: An experimental study, BYG. DTU, Lyngby, 2004.

- [40] Young, T.: III. An essay on the cohesion of fluids, *Phil. Trans. R. Soc.*, 95, 1805, 65–87.
- [41] Zisman, W.A., “Relation of the Equilibrium Contact Angle to Liquid and Solid Constitution,” in *Contact Angle, Wettability, and Adhesion*, Fowkes, F.M. (ed.), American Chemical Society, Washington, D.C., 1964.
- [42] Owens, D.K. and Wendt, R.C.: Estimation of the surface free energy of polymers, *J. Appl. Polym. Sci.*, 13, 1969, 1741–1747.
- [43] Wu, S.: Polar and Nonpolar Interactions in Adhesion, *The Journal of Adhesion*, 5, 1973, 39–55.
- [44] Heng, J.Y.Y., Pearse, D.F., Thielmann, F., Lampke, T., and Bismarck, A.: Methods to determine surface energies of natural fibres: a review, *Composite Interfaces*, 14, 2007, 581–604.
- [45] Medina, L., Schledjewski, R., and Schlarb, A.K.: Process related mechanical properties of press molded natural fiber reinforced polymers, *Composites Science and Technology*, 69, 2009, 1404–1411.
- [46] Blöchl, Y. and Schledjewski, R.: A robust empirical model equation for the compaction response of textile reinforcements, *Polym. Compos.*, 2020.
- [47] van Wyk, C.M.: Note on the Compressibility of Wool, *Journal of the Textile Institute Transactions*, 37, 1946, T285-T292.
- [48] Beil, N.B. and Roberts, W.W.: Modeling and Computer Simulation of the Compressional Behavior of Fiber Assemblies: Part I: Comparison to van Wyk's theory, *Textile Research Journal*, 72, 2002, 341–351.
- [49] Beil, N.B. and Roberts, W.W.: Modeling and Computer Simulation of the Compressional Behavior of Fiber Assemblies: Part II: Hysteresis, Crimp, and Orientation Effects, *Textile Research Journal*, 72, 2002, 375–382.
- [50] Chen, B.: Compaction of woven-fabric preforms: nesting and multi-layer deformation, *Composites Science and Technology*, 60, 2000, 2223–2231.
- [51] Chen, B., Cheng, A.H.-D., and Chou, T.-W.: A nonlinear compaction model for fibrous preforms, *Composites Part A: Applied Science and Manufacturing*, 32, 2001, 701–707.

- [52] Chen, B., Lang, E.J., and Chou, T.-W.: Experimental and theoretical studies of fabric compaction behavior in resin transfer molding, *Materials Science and Engineering: A*, 317, 2001, 188–196.
- [53] Shah, D.U. and Clifford, M.J., “Compaction, Permeability and Flow Simulation for Liquid Composite Moulding of Natural Fibre Composites,” in *Manufacturing of Natural Fibre Reinforced Polymer Composites*, Salit, M.S., Jawaid, M., Yusoff, N.B., and Hoque, M.E. (eds.), Springer International Publishing, Cham, 2015.
- [54] Francucci, G. and Rodríguez, E.S.: Modeling of the compaction response of jute fabrics in liquid composite molding processes, *J. Appl. Polym. Sci.*, 37, 2011, 4789–4798.
- [55] Francucci, G., Rodríguez, E.S., and Vázquez, A.: Experimental study of the compaction response of jute fabrics in liquid composite molding processes, *Journal of Composite Materials*, 46, 2011, 155–167.
- [56] Francucci, G., Vázquez, A., and Rodríguez, E.S.: Key differences on the compaction response of natural and glass fiber preforms in liquid composite molding, *Textile Research Journal*, 82, 2012, 1774–1785.
- [57] Kruckenberg, T. M. and Paton, R.: *Resin Transfer Moulding for Aerospace Structures*, Springer Netherlands, Dordrecht, 1998.
- [58] Darcy, H.: *Les Fontaines Publiques de la Ville de Dijon*, Dalmont, Paris 1856.
- [59] Whitaker, S.: Flow in porous media I: A theoretical derivation of Darcy's law, *Transp Porous Med*, 1, 1986, 3–25.
- [60] Tucker, C.L. and Dessenberger, R.B., “Governing equations for flow and heat transfer in stationary fiber beds,” in *Flow and rheology in polymer composites manufacturing*, Advani, S.G. (ed.), Elsevier, Amsterdam, 1994.
- [61] Dullien, F. A. L.: *Porous media: Fluid transport and pore structure*, 2. ed., Acad. Press, San Diego, 1992.
- [62] Adams, K.L., Russel, B., and Rebenfeld, L.: Radial penetration of a viscous liquid into a planar anisotropic porous medium, *Int. J. Multiphase Flow*, 1988.

- [63] Adams, K.L. and Rebenfeld, L.: In-Plane Flow of Fluids in Fabrics: Structure/Flow Characterization, *Textile Research Journal*, 57, 1987, 647–654.
- [64] Weitzenböck, J.R., Sheno, R.A., and Wilson, P.A.: Radial flow permeability measurement. Part A: Theory, *Composites Part A: Applied Science and Manufacturing*, 30, 1999, 781–796.
- [65] Chan, A.W. and Hwang, S.-T.: Anisotropic in-plane permeability of fabric media, *Polym. Eng. Sci.*, 31, 1991, 1233–1239.
- [66] Carter, E.J., Fell, A.W., and Summerscales, J.: Appendix 2. A simplified model to calculate the permeability tensor of an anisotropic fibre bed, *Composites Manufacturing*, 6, 1995, 228–235.
- [67] Fauster, E., Berg, D.C., May, D., Blößl, Y., and Schledjewski, R.: Robust evaluation of flow front data for in-plane permeability characterization by radial flow experiments, *Advanced Manufacturing: Polymer & Composites Science*, 4, 2018, 24–40.
- [68] Adams, K.L. and Rebenfeld, L.: Permeability characteristics of multilayer fiber reinforcements. Part I: Experimental observations, *Polym. Compos.*, 12, 1991, 179–185.
- [69] Adams, K.L., Miller, B., and Rebenfeld, L.: Forced in-plane flow of an epoxy resin in fibrous networks, *Polym. Eng. Sci.*, 26, 1986, 1434–1441.
- [70] May, D., Aktas, A., Advani, S.G., Berg, D.C., Endruweit, A., Fauster, E., Lomov, S.V., Long, A., Mitschang, P., Abaimov, S., Abliz, D., Akhatov, I., Ali, M.A., Allen, T.D., Bickerton, S., Bodaghi, M., Caglar, B., Caglar, H., Chiminelli, A., Correia, N., Cosson, B., Danzi, M., Dittmann, J., Ermanni, P., Francucci, G., George, A., Grishaev, V., Hancioglu, M., Kabachi, M.A., Kind, K., Deléglise-Lagardère, M., Laspalas, M., Lebedev, O.V., Lizaranzu, M., Liotier, P.-J., Middendorf, P., Morán, J., Park, C.-H., Pipes, R.B., Pucci, M.F., Raynal, J., Rodriguez, E.S., Schledjewski, R., Schubnel, R., Sharp, N., Sims, G., Sozer, E.M., Sousa, P., Thomas, J., Umer, R., Wijaya, W., Willenbacher, B., Yong, A., Zaremba, S., and Ziegmann, G.: In-plane permeability characterization of engineering textiles based on radial flow experiments: A

- benchmark exercise, *Composites Part A: Applied Science and Manufacturing*, 121, 2019, 100–114.
- [71] Vernet, N., Ruiz, E., Advani, S., Alms, J.B., Aubert, M., Barburski, M., Barari, B., Beraud, J.M., Berg, D.C., Correia, N., Danzi, M., Delavière, T., Dickert, M., Di Fratta, C., Endruweit, A., Ermanni, P., Francucci, G., Garcia, J.A., George, A., Hahn, C., Klunker, F., Lomov, S.V., Long, A., Louis, B., Maldonado, J., Meier, R., Michaud, V., Perrin, H., Pillai, K., Rodriguez, E., Trochu, F., Verheyden, S., Wietgreffe, M., Xiong, W., Zaremba, S., and Ziegmann, G.: Experimental determination of the permeability of engineering textiles: Benchmark II, *Composites Part A: Applied Science and Manufacturing*, 61, 2014, 172–184.
- [72] Arbter, R., Beraud, J.M., Binetruy, C., Bizet, L., Bréard, J., Comas-Cardona, S., Demaria, C., Endruweit, A., Ermanni, P., Gommer, F., Hasanovic, S., Henrat, P., Klunker, F., Laine, B., Lavanchy, S., Lomov, S.V., Long, A., Michaud, V., Morren, G., Ruiz, E., Sol, H., Trochu, F., Verleye, B., Wietgreffe, M., Wu, W., and Ziegmann, G.: Experimental determination of the permeability of textiles: A benchmark exercise, *Composites Part A: Applied Science and Manufacturing*, 42, 2011, 1157–1168.
- [73] Lundström, T.S., Stenberg, R., Bergström, R., Partanen, H., and Birkeland, P.A.: In-plane permeability measurements: a nordic round-robin study, *Composites Part A: Applied Science and Manufacturing*, 31, 2000, 29–43.
- [74] Groessing, H., Becker, D., Kaufmann, S., Schledjewski, R., and Mitschang, P.: An evaluation of the reproducibility of capacitive sensor based in-plane permeability measurements: A benchmarking study, *Express Polym. Lett.*, 9, 2015, 129–142.
- [75] Nield, D. A. and Bejan, A.: *Convection in Porous Media*, 4. ed., Springer, New York, NY, 2013.
- [76] Carman, P.C.: Fluid flow through granular beds, *Chemical Engineering Research and Design*, 75, 1997, S32-S48.
- [77] Kozeny, J.: Über kapillare Leitung des Wassers im Boden, *Sitz. Ber. Math.-Nat. Kl. Akad. Wiss., Wien*, 1927, 271–306.

- [78] Rodriguez, E., Giacomelli, F., and Vazquez, A.: Permeability-Porosity Relationship in RTM for Different Fiberglass and Natural Reinforcements, *Journal of Composite Materials*, 38, 2004, 259–268.
- [79] van Nguyen, H., Lagardère, M., Park, C.H., and Panier, S.: Permeability of natural fiber reinforcement for liquid composite molding processes, *J Mater Sci*, 49, 2014, 6449–6458.
- [80] Masoodi, R. and Pillai, K.M., “Modeling the Processing of Natural Fiber Composites Made Using Liquid Composite Molding,” in *Handbook of Bioplastics and Biocomposites Engineering Applications*, Pilla, S. (ed.), John Wiley & Sons, Hoboken, 2011.
- [81] Gauvin, R., Kerachni, A., and Fisa, B.: Variation of Mat Surface Density and Its Effect on Permeability Evaluation for RTM Modelling, *Journal of Reinforced plastics and composites*, 13, 1994, 371–383.
- [82] Washburn, E.W.: The Dynamics of Capillary Flow, *Phys. Rev.*, 17, 1921, 273–283.
- [83] Lucas, R.: Über das Zeitgesetz des kapillaren Aufstiegs von Flüssigkeiten, *Kolloid-Zeitschrift*, 23, 1918, 15–22.
- [84] Bell, J.M. and Cameron, F.K.: The Flow of Liquids through Capillary Spaces, *J. Phys. Chem.*, 10, 1906, 658–674.
- [85] Masoodi, R. and Pillai, K. M.: *Wicking in Porous Materials*, CRC Press, 2012.
- [86] Bear, J.: *Dynamics of Fluids in Porous Media*, Dover Publications, Inc., New York, 2013.
- [87] Panton, R. L.: *Incompressible Flow*, Wiley, 2013.
- [88] Deen, W. M.: *Introduction to chemical engineering fluid mechanics*, Cambridge University Press, Cambridge, 2016.
- [89] Fries, N.: *Capillary transport processes in porous materials - experiment and model*, 1. ed., Cuvillier Verlag, Göttingen, 2010.
- [90] Quéré, D.: Inertial capillarity, *Europhys. Lett.*, 39, 1997, 533–538.

- [91] Bosanquet, C.H.: On the flow of liquids into capillary tubes, The London, Edinburgh, and Dublin Philosophical Magazine and Journal of Science, 45, 1923, 525–531.
- [92] Fries, N. and Dreyer, M.: The transition from inertial to viscous flow in capillary rise, Journal of Colloid and Interface Science, 327, 2008, 125–128.
- [93] H. Dodiuk, Ed.: Handbook of thermoset plastics, 3. ed., Elsevier, Amsterdam, 2014.
- [94] Mittal, V., Saini, R., and Sinha, S.: Natural fiber-mediated epoxy composites – A review, Composites Part B: Engineering, 99, 2016, 425–435.
- [95] Shahzad, A.: Hemp fiber and its composites – a review, Journal of Composite Materials, 46, 2012, 973–986.
- [96] Yan, L., Chouw, N., and Jayaraman, K.: Flax fibre and its composites – A review, Composites Part B: Engineering, 56, 2014, 296–317.
- [97] Asim, M., Saba, N., Jawaid, M., Nasir, M., Pervaiz, M., and Alothman, O.Y.: A Review on Phenolic Resin and its Composites, CAC, 14, 2018, 185–197.
- [98] E.S. Zainudin, H. Ismail, and S.M. Sapuan, Eds.: Natural fiber reinforced vinyl ester and vinyl polymer composites: Development, characterization and applications, Woodhead Publishing an imprint of Elsevier, Duxford, United Kingdom, 2018.
- [99] Anusic, A., Blöchl, Y., Oreski, G., and Resch-Fauster, K.: High-performance thermoset with 100 % bio-based carbon content, Polymer Degradation and Stability, 181, 2020.
- [100] Schledjewski, R., Lloret Pertegas, S., Blöchl, Y., Anusic, A., Resch-Fauster, K., Mahendran, A.R., and Wuzella, G.: High Performance Green Composites for Green Technologies, KEM, 742, 2017, 271–277.
- [101] Raquez, J.-M., Deléglise, M., Lacrampe, M.-F., and Krawczak, P.: Thermosetting (bio)materials derived from renewable resources: A critical review, Progress in Polymer Science, 35, 2010, 487–509.
- [102] Sharma, V. and Kundu, P.P.: Addition polymers from natural oils - A review, Progress in Polymer Science, 31, 2006, 983–1008.

- [103] Baur, E., Brinkmann, S., Osswald, T. A., Schmachtenberg, E., and Saechtling, H.: Saechtling Kunststoff Taschenbuch, 30. ed., Hanser, München, 2007.
- [104] M. Neitzel, P. Mitschang, and G. Beresheim, Eds.: Handbuch Verbundwerkstoffe: Werkstoffe, Verarbeitung, Anwendung, Hanser, München, 2004.
- [105] Patel, N. and Lee, L.J.: Effects of fiber mat architecture on void formation and removal in liquid composite molding, *Polym. Compos.*, 16, 1995, 386–399.
- [106] Patel, N. and Lee, L.J.: Modeling of void formation and removal in liquid composite molding. Part II, *Polym. Compos.*, 17, 1996, 104–114.
- [107] Patel, N. and Lee, L.J.: Modeling of void formation and removal in liquid composite molding. Part I: Wettability analysis, *Polym. Compos.*, 17, 1996, 96–103.
- [108] Mahale, A.D., Prud'Homme, R.K., and Rebenfeld, L.: Quantitative measurement of voids formed during liquid impregnation of nonwoven multifilament glass networks using an optical visualization technique, *Polym. Eng. Sci.*, 32, 1992, 319–326.
- [109] Patel, N.: Micro scale flow behavior, fiber wetting and void formation in Liquid Composite Molding, Dissertation. The Ohio State University, 1994.
- [110] Ruiz, E., Achim, V., Soukane, S., Trochu, F., and Breard, J.: Optimization of injection flow rate to minimize micro/macro-voids formation in resin transfer molded composites, *Composites Science and Technology*, 66, 2006, 475–486.
- [111] Labat, L., Bréard, J., Pillut-Lesavre, S., and Bouquet, G.: Void fraction prevision in LCM parts, *Eur. Phys. J. AP*, 16, 2001, 157–164.
- [112] Leclerc, J.S. and Ruiz, E.: Porosity reduction using optimized flow velocity in Resin Transfer Molding, *Composites Part A: Applied Science and Manufacturing*, 39, 2008, 1859–1868.

- [113] Chen, Y.-T., Davis, H.T., and Macosko, C.W.: Wetting of fiber mats for composites manufacturing: I. Visualization experiments, *AIChE J.*, 41, 1995, 2261–2273.
- [114] Chen, Y.-T., Macosko, C.W., and Davis, H.T.: Wetting of fiber mats for composites manufacturing: II. Air entrapment model, *AIChE J.*, 41, 1995, 2274–2281.
- [115] Park, C.H. and Lee, I.L.: Modeling void formation and unsaturated flow in liquid composite molding processes, *Journal of Reinforced plastics and composites*, 30, 2011, 957–977.
- [116] Park, C.H., Lebel, A., Saouab, A., Bréard, J., and Lee, W.I.: Modeling and simulation of voids and saturation in liquid composite molding processes, *Composites Part A: Applied Science and Manufacturing*, 42, 2011, 658–668.
- [117] Lee, G.-W. and Lee, K.-J.: Mechanism of Void Formation in Composite Processing with Woven Fabrics, *Polymers and Polymer Composites*, 11, 2003, 563–572.
- [118] LeBel, F., Fanaei, A.E., Ruiz, E., and Trochu, F.: Experimental characterization by fluorescence of capillary flows in dual-scale engineering fabrics, *Textile Research Journal*, 83, 2013, 1634–1659.
- [119] LeBel, F., Fanaei, A.E., Ruiz, É., and Trochu, F.: Prediction of optimal flow front velocity to minimize void formation in dual scale fibrous reinforcements, *Int J Mater Form*, 7, 2014, 93–116.
- [120] Parnas, R.S. and Walsh, S.M.: Vacuum-assisted resin transfer molding model, *Polym. Compos.*, 26, 2005, 477–485.
- [121] Ravey, C., Ruiz, E., and Trochu, F.: Determination of the optimal impregnation velocity in Resin Transfer Molding by capillary rise experiments and infrared thermography, *Composites Science and Technology*, 99, 2014, 96–102.
- [122] Ravey, C., LeBel, F., Ruiz, R., Courteau-Godmaire, H., and Trochu, F., “Void minimization and optimization of injection velocity in RTM processing,” in *Proceedings of the 19th International Conference on Composite Materials*

- (*ICCM-19*), Concordia Centre for Composites, Concordia University (ed.), 2013.
- [123] Causse, P., Ravey, C., and Trochu, F.: Capillary Characterization of Fibrous Reinforcement and Optimization of Injection Strategy in Resin Transfer Molding, *J. Compos. Sci.*, 2, 2018, 19.
- [124] Eco-Technilin SAS: Technical Data Sheet: Fibrimat F300.
- [125] Eco-Technilin SAS: Technical Data Sheet: Fibrimar F450.
- [126] Composites Evolution Ltd.: Technical Data Sheet: Biotex Flax 200g/m² 2x2 Twill.
- [127] Composites Evolution Ltd.: Technical Data Sheet: Biotex Flax 400 g/m² 2x2 Twill.
- [128] Bcomp Ltd.: Technical Data Sheet: AmpliTex 5009: AmpliTex flax unidirectional fabric 300 gsm.
- [129] bto-epoxy GmbH: Technical Data Sheet: Epinal RSBC-Epoxy-Infusionssystem: Epoxy Infusions-, Laminier- & Klebesystem, 2018.
- [130] Glück, J., Bobertag, M., Mischang, P., and Becker, D.: Schnelle Permeabilitätsbestimmung von Textilien in QS und F+E, *GAK - Gummi Fasern Kunststoffe*, 68, 2015, 168–172.
- [131] Fauster, E., Berg, D.C., Abliz, D., Grössing, H., Meiners, D., Ziegmann, G., and Schledjewski, R.: Image processing and data evaluation algorithms for reproducible optical in-plane permeability characterization by radial flow experiments, *Journal of Composite Materials*, 53, 2019, 45–63.
- [132] O'Leary, P. and Zsombor-Murray, P.: Direct and specific least-square fitting of hyperbolæ and ellipses, *J. Electron. Imaging*, 13, 2004, 492.
- [133] O'Leary, P., Harker, M., and Zsombor-Murray, P.: Direct and least square fitting of coupled geometric objects for metric vision, *IEE Proc., Vis. Image Process.*, 152, 2005, 687.

- [134] Harker, M., O'Leary, P., and Zsombor-Murray, P.: Direct type-specific conic fitting and eigenvalue bias correction, *Image and Vision Computing*, 26, 2008, 372–381.
- [135] Bookstein, F.L.: Fitting conic sections to scattered data, *Computer Graphics And Image Processing*, 9, 1979, 56–71.
- [136] Pilu, M., Fitzgibbon, A.W., and Fisher, R.B., "Ellipse-specific direct least-square fitting," in *Proceedings, International Conference on Image Processing: September 16-19, 1996, Lausanne, Switzerland*, New York, Piscataway, NJ, 1996.
- [137] Fitzgibbon, A.W., Pilu, M., and Fisher, R.B., "Direct least squares fitting of ellipses," in *Proceedings of the 13th International Conference on Pattern Recognition*, IEEE, 1996.
- [138] Grössing, H.: Contributing to the Optimization of the Preform LCM Process Chain: Permeability of Reinforcing Textiles, Dissertation. Montanuniversität Leoben, 2015.
- [139] Xue, D., Miao, M., and Hu, H.: Permeability anisotropy of flax nonwoven mats in vacuum-assisted resin transfer molding, *Journal of the Textile Institute*, 102, 2011, 612–620.
- [140] Liotier, P.-J., Govignon, Q., Swery, E., Drapier, S., and Bickerton, S.: Characterisation of woven flax fibres reinforcements: Effect of the shear on the in-plane permeability, *Journal of Composite Materials*, 49, 2015, 3415–3430.
- [141] Rieber, G., Jiang, J., Deter, C., Chen, N., and Mitschang, P.: Influence of textile parameters on the in-plane Permeability, *Composites Part A: Applied Science and Manufacturing*, 52, 2013, 89–98.
- [142] Amico, S. and Lekakou, C.: An experimental study of the permeability and capillary pressure in resin-transfer moulding, *Composites Science and Technology*, 61, 2001, 1945–1959.

- [143] Francucci, G., Vázquez, A., Ruiz, E., and Rodríguez, E.S.: Capillary effects in vacuum-assisted resin transfer molding with natural fibers, *Polym. Compos.*, 33, 2012, 1593–1602.
- [144] LeBel, F., Ruiz, É., and Trochu, F.: Experimental study of saturation by visible light transmission in dual-scale fibrous reinforcements during composite manufacturing, *Journal of Reinforced plastics and composites*, 36, 2017, 1693–1711.
- [145] Kuentzer, N., Simacek, P., Advani, S.G., and Walsh, S.: Permeability characterization of dual scale fibrous porous media, *Composites Part A: Applied Science and Manufacturing*, 37, 2006, 2057–2068.
- [146] Zhou, F., Kuentzer, N., Simacek, P., Advani, S.G., and Walsh, S.: Analytic characterization of the permeability of dual-scale fibrous porous media, *Composites Science and Technology*, 66, 2006, 2795–2803.
- [147] Bodaghi, M., Lomov, S.V., Simacek, P., Correia, N.C., and Advani, S.G.: On the variability of permeability induced by reinforcement distortions and dual scale flow in liquid composite moulding: A review, *Composites Part A: Applied Science and Manufacturing*, 120, 2019, 188–210.
- [148] Trochu, F., Ruiz, E., Achim, V., and Soukane, S.: Advanced numerical simulation of liquid composite molding for process analysis and optimization, *Composites Part A: Applied Science and Manufacturing*, 37, 2006, 890–902.
- [149] Pucci, M.F., Liotier, P.-J., and Drapier, S.: Tensiometric method to reliably assess wetting properties of single fibers with resins: Validation on cellulosic reinforcements for composites, *Colloids and Surfaces A: Physicochemical and Engineering Aspects*, 512, 2017, 26–33.
- [150] Wang, J., Fuentes, C.A., Zhang, D., Wang, X., van Vuure, A.W., and Seveno, D.: Wettability of carbon fibres at micro- and mesoscales, *Carbon*, 120, 2017, 438–446.
- [151] Qiu, S., Fuentes, C.A., Zhang, D., van Vuure, A.W., and Seveno, D.: Wettability of a Single Carbon Fiber, *Langmuir the ACS journal of surfaces and colloids*, 32, 2016, 9697–9705.

- [152] Fox, H.W. and Zisman, W.A.: The spreading of liquids on low energy surfaces. I. polytetrafluoroethylene, *Journal of Colloid Science*, 5, 1950, 514–531.
- [153] KRÜSS GmbH: Technical Note TN306e: Models for Surface Free Energy Calculation, 1999.
- [154] Yarce, C.J., Pineda, D., Correa, C.E., and Salamanca, C.H.: Relationship between Surface Properties and In Vitro Drug Release from a Compressed Matrix Containing an Amphiphilic Polymer Material, *Pharmaceuticals* (Basel, Switzerland), 9, 2016.
- [155] Binks, B.P. and Tyowua, A.T.: Oil-in-oil emulsions stabilised solely by solid particles, *Soft matter*, 12, 2016, 876–887.
- [156] D.R. Lide, Ed.: *CRC handbook of chemistry and physics: A ready-reference book of chemical and physical data*, 84. ed., CRC Press, Boca Raton, 2003.
- [157] DDBST GmbH: Dortmund Data Bank Software and Separation Technology, URL: http://www.ddbst.com/en/EED/PCP/SFT_C95.php (checked on 3. November 2020).
- [158] Estrada-Baltazar, A., Bravo-Sanchez, M.G., Iglesias-Silva, G.A., Alvarado, J.F.J., Castrejon-Gonzalez, E.O., and Ramos-Estrada, M.: Densities and viscosities of binary mixtures of n-decane+1-pentanol, +1-hexanol, +1-heptanol at temperatures from 293.15 to 363.15K and atmospheric pressure, *Chinese Journal of Chemical Engineering*, 23, 2015, 559–571.
- [159] Celsius SARL: *Caracteristiques Physiques des Fluides Thermiques: Physical Data of Thermal Fluids*, Isoporpanol.
- [160] Technical Data Sheet: XIAMETER™ PMX-200 Silicone Fluid, 50–1,000 cSt, 2017.
- [161] Dai, Q., Chong, Z., Huang, W., and Wang, X.: Migration of Liquid Bridges at the Interface of Spheres and Plates with an Imposed Thermal Gradient, *Langmuir the ACS journal of surfaces and colloids*, 36, 2020, 6268–6276.

- [162] Pucci, M.F., Liotier, P.-J., and Drapier, S.: Capillary wicking in flax fabrics – Effects of swelling in water, *Colloids and Surfaces A: Physicochemical and Engineering Aspects*, 498, 2016, 176–184.
- [163] Lekner, J. and Dorf, M.C.: Why some things are darker when wet, *Applied optics*, 27, 1988, 1278–1280.
- [164] Masoodi, R., Pillai, K.M., and Varanasi, P.P.: Darcy's law-based models for liquid absorption in polymer wicks, *AIChE J.*, 53, 2007, 2769–2782.
- [165] Masoodi, R., Tan, H., and Pillai, K.M.: Darcy's law-based numerical simulation for modeling 3D liquid absorption into porous wicks, *AIChE J.*, 57, 2011, 1132–1143.
- [166] Synytska, A., Michel, S., Pleul, D., Bellmann, C., Schinner, R., Eichhorn, K.-J., Grundke, K., Neumann, A.W., and Stamm, M.: Monitoring the surface tension of reactive epoxy-amine systems under different environmental conditions, *The Journal of Adhesion*, 80, 2004, 667–683.
- [167] Kopczynska, A. and Ehrenstein, G.W.: Sonderdrucke: Oberflächenspannung von Kunststoffen - Messmethoden am LKT.
- [168] Masoodi, R., Pillai, K.M., Grahl, N., and Tan, H.: Numerical simulation of LCM mold-filling during the manufacture of natural fiber composites, *Journal of Reinforced plastics and composites*, 31, 2012, 363–378.
- [169] Esteban, B., Riba, J.-R., Baquero, G., Puig, R., and Rius, A.: Characterization of the surface tension of vegetable oils to be used as fuel in diesel engines, *Fuel*, 102, 2012, 231–238.
- [170] Blöchl, Y., Hegedüs, G., Szabó, G., Tábi, T., Schledjewski, R., and Czigany, T.: Applicability of fiber Bragg grating sensors for cure monitoring in resin transfer molding processes, *Journal of Reinforced plastics and composites*, 2020.
- [171] DIN Deutsches Institut für Normung e.V.: Fibre-reinforced plastic composites - Determination of flexural properties.
- [172] D20 Committee: ASTM D2734 - Test Methods for Void Content of Reinforced Plastics, ASTM International, West Conshohocken, PA.

- [173]Mettler-Toledo AG: Operating Instructions Density Kit: For Solids and Liquids Determination, Greifensee, Switzerland, 2010.
- [174]Lundström, T.S. and Gebart, B.R.: Influence from process parameters on void formation in resin transfer molding, *Polym. Compos.*, 15, 1994, 25–33.
- [175]Lundström, T.S., Gebart, B.R., and Lundemo, C.Y.: Void Formation in RTM, *Journal of Reinforced plastics and composites*, 12, 1993, 1339–1349.
- [176]LeBel, F., Ruiz, É., and Trochu, F.: Void content analysis and processing issues to minimize defects in liquid composite molding, *Polym. Compos.*, 40, 2019, 109–120.
- [177]Varna, J., Joffe, R., Berglund, L.A., and Lundström, T.S.: Effect of voids on failure mechanisms in RTM laminates, *Composites Science and Technology*, 53, 1995, 241–249.
- [178]Sisodia, S.M., Garcea, S.C., George, A.R., Fullwood, D.T., Spearing, S.M., and Gamstedt, E.K.: High-resolution computed tomography in resin infused woven carbon fibre composites with voids, *Composites Science and Technology*, 131, 2016, 12–21.
- [179]Hayward, J.S. and Harris, B.: The effect of vacuum assistance in resin transfer moulding, *Composites Manufacturing*, 1, 1990, 161–166.

A Appendix

A.1 Navier-Stokes equation for incompressible fluids

$$\rho \left(\frac{\partial \mathbf{v}}{\partial t} + (\mathbf{v} \cdot \nabla) \mathbf{v} \right) = -\nabla p + \eta \Delta \mathbf{v} + \mathbf{f} \quad (98)$$

ρ ... density

\mathbf{v} ... velocity vector

p ... physical pressure

η ... dynamic viscosity

\mathbf{f} ... volume force vector

Components in a cartesian coordinate system:

$$\begin{aligned} x: \quad & \rho \left[\frac{\partial v_x}{\partial t} + v_x \frac{\partial v_x}{\partial x} + v_y \frac{\partial v_x}{\partial y} + v_z \frac{\partial v_x}{\partial z} \right] \\ & = -\frac{\partial p}{\partial x} + \eta \left[\frac{\partial^2 v_x}{\partial x^2} + \frac{\partial^2 v_x}{\partial y^2} + \frac{\partial^2 v_x}{\partial z^2} \right] + f_x \end{aligned} \quad (99)$$

$$\begin{aligned} y: \quad & \rho \left[\frac{\partial v_y}{\partial t} + v_x \frac{\partial v_y}{\partial x} + v_y \frac{\partial v_y}{\partial y} + v_z \frac{\partial v_y}{\partial z} \right] \\ & = -\frac{\partial p}{\partial y} + \eta \left[\frac{\partial^2 v_y}{\partial x^2} + \frac{\partial^2 v_y}{\partial y^2} + \frac{\partial^2 v_y}{\partial z^2} \right] + f_y \end{aligned} \quad (100)$$

$$\begin{aligned} z: \quad & \rho \left[\frac{\partial v_z}{\partial t} + v_x \frac{\partial v_z}{\partial x} + v_y \frac{\partial v_z}{\partial y} + v_z \frac{\partial v_z}{\partial z} \right] \\ & = -\frac{\partial p}{\partial z} + \eta \left[\frac{\partial^2 v_z}{\partial x^2} + \frac{\partial^2 v_z}{\partial y^2} + \frac{\partial^2 v_z}{\partial z^2} \right] + f_z \end{aligned} \quad (101)$$

Components in a cylindrical coordinate system:

$$\begin{aligned}
 r: \quad \rho \left[\frac{\partial v_r}{\partial t} + v_r \frac{\partial v_r}{\partial r} + \frac{v_\varphi}{r} \frac{\partial v_r}{\partial \varphi} - \frac{v_\varphi^2}{r} + v_z \frac{\partial v_r}{\partial z} \right] = \\
 = -\frac{\partial p}{\partial r} + \eta \left[\frac{\partial}{\partial r} \left(\frac{1}{r} \frac{\partial}{\partial r} (r v_r) \right) + \frac{1}{r^2} \frac{\partial^2 v_r}{\partial \varphi^2} - \frac{2}{r^2} \frac{\partial v_\varphi}{\partial \varphi} + \frac{\partial^2 v_r}{\partial z^2} \right] \\
 + f_r
 \end{aligned} \tag{102}$$

$$\begin{aligned}
 \varphi: \quad \rho \left[\frac{\partial v_\varphi}{\partial t} + v_r \frac{\partial v_\varphi}{\partial r} + \frac{v_\varphi}{r} \frac{\partial v_\varphi}{\partial \varphi} + \frac{v_r v_\varphi}{r} + v_z \frac{\partial v_\varphi}{\partial z} \right] = \\
 = -\frac{1}{r} \frac{\partial p}{\partial \varphi} \\
 + \eta \left[\frac{\partial}{\partial r} \left(\frac{1}{r} \frac{\partial}{\partial r} (r v_\varphi) \right) + \frac{1}{r^2} \frac{\partial^2 v_\varphi}{\partial \varphi^2} + \frac{2}{r^2} \frac{\partial v_\varphi}{\partial \varphi} + \frac{\partial^2 v_\varphi}{\partial z^2} \right] + f_\varphi
 \end{aligned} \tag{103}$$

$$\begin{aligned}
 z: \quad \rho \left[\frac{\partial v_z}{\partial t} + v_r \frac{\partial v_z}{\partial r} + \frac{v_\varphi}{r} \frac{\partial v_z}{\partial \varphi} + v_z \frac{\partial v_z}{\partial z} \right] = \\
 = -\frac{\partial p}{\partial z} + \eta \left[\frac{1}{r} \frac{\partial}{\partial r} \left(r \frac{\partial v_z}{\partial r} \right) + \frac{1}{r^2} \frac{\partial^2 v_z}{\partial \varphi^2} + \frac{\partial^2 v_z}{\partial z^2} \right] + f_z
 \end{aligned} \tag{104}$$

A.2 Continuity equation for incompressible fluids

$$\nabla \cdot \boldsymbol{v} = 0 \quad (105)$$

\boldsymbol{v} ... velocity vector

Cartesian coordinate system:

$$\frac{\partial v_x}{\partial x} + \frac{\partial v_y}{\partial y} + \frac{\partial v_z}{\partial z} = 0 \quad (106)$$

Cylindrical coordinate system:

$$\frac{1}{r} \frac{\partial}{\partial r} (r v_r) + \frac{1}{r} \frac{\partial v_\varphi}{\partial \varphi} + \frac{\partial v_z}{\partial z} = 0 \quad (107)$$

A.3 Derivation of the velocity profile for steady laminar flow (Poiseuille flow) through a circular tube

The flow of an incompressible, Newtonian fluid through a pipe of radius R is depicted schematically in Figure 86. The following derivation of the corresponding velocity distribution based on the conservation equations for mass (continuity equation) and momentum (Navier-Stokes equation).

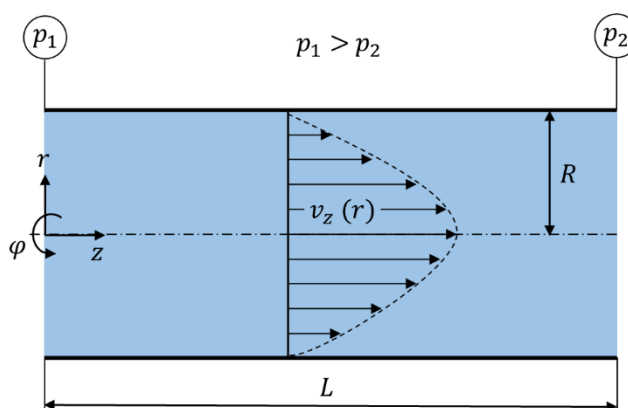


Figure 86: Schematics regarding the Hagen-Poiseuille equation

The present case is a pressure driven flow in positive z -direction with the inlet pressure p_1 and the outlet pressure p_2 , where $p_1 > p_2$.

The velocity field and its components are defined based on the following assumptions and conditions:

1. The pipe and the flow are cylindrically symmetric \rightarrow Independence of φ .
2. Steady state condition of the flow \rightarrow Absence of inertial forces.
3. The flow is fully developed \rightarrow Effects at the entry of the tube are negligible and the velocity vector is independent of z .
4. The tube walls are impermeable (no-penetration condition):

$$v_r(R) = 0 \quad (108)$$

5. No relative movement between fluid and solid tube wall at the interface (no-slip condition)

$$v_z(R) = 0 \quad (109)$$

6. No swirling motion of the fluid:

$$v_{\varphi} = 0 \quad (110)$$

7. The velocity in the center line is finite.

The continuity equation for the cylindrical coordinate system in Eq. (107) is, due to the definitions 2., 3. and 6., reduced to:

$$\frac{1}{r} \frac{\partial}{\partial r} (r v_r) = 0 \quad (111)$$

Due to the no-penetration condition 4., the radial velocity component must be zero ($v_r = 0$) to fulfill the mass conservation.

Therefore, the only non-zero velocity component is v_z , which is a function only dependent on r , due to the axis-symmetry (1.) and the fully developed flow (3.).

Considering that $v_r = v_{\varphi} = 0$ and the steady state condition 2., the Navier-Stokes equation for the three vectors in the cylindrical coordinate system is reduced to:

$$r: \quad \frac{\partial p}{\partial r} = 0 \quad (112)$$

$$\varphi: \quad \frac{\partial p}{\partial \varphi} = 0 \quad (113)$$

$$z: \quad \frac{\partial p}{\partial z} = \frac{\eta}{r} \frac{\partial}{\partial r} \left(r \frac{\partial v_z}{\partial r} \right) \quad (114)$$

Due to Eq (112) and Eq. (113) the pressure p is a function only dependent on z . Considering that $p = p(z)$ only and $v_z = v_z(r)$ only, both sides of Eq. (114) must be constant and ordinary differentials are appropriate.

Therefore $p(z)$ is a linear function, which can be written as:

$$\frac{dp}{dz} = \text{const.} \Leftrightarrow \frac{dp}{dz} = \frac{p_2 - p_1}{L} = -\frac{\Delta p}{L} \quad (115)$$

And the 2nd order ordinary differential equation can be solved by integration as follows:

$$\begin{aligned}
-\frac{\Delta p}{L} &= \frac{\eta}{r} \frac{d}{dr} \left(r \frac{dv_z}{dr} \right) \\
\int d \left(r \frac{dv_z}{dr} \right) &= - \int \frac{r \Delta p}{\eta L} dr \\
r \frac{dv_z}{dr} &= - \frac{r^2 \Delta p}{2\eta L} + c_1 \\
\int dv_z &= \int \left(- \frac{r \Delta p}{2\eta L} + \frac{c_1}{r} \right) dr \\
v_z &= - \frac{r^2 \Delta p}{4\eta L} + c_1 \ln(r) + c_2
\end{aligned} \tag{116}$$

Using the no-slip boundary conditions 5. and the finite fluid velocity at the tube axis, the integration constants c_1 and c_2 are as follows:

$$\begin{aligned}
v_z(R) &= - \frac{R^2 \Delta p}{4\eta L} + c_1 \ln(R) + c_2 = 0 \\
\Rightarrow c_2 &= \frac{R^2 \Delta p}{4\eta L} - c_1 \ln(R) = 0 \\
v_z(0) &= 0 + c_1 \ln(0) + c_2 = \text{finite} \\
\Rightarrow c_1 &= 0 \\
\Rightarrow c_2 &= \frac{R^2 \Delta p}{4\eta L}
\end{aligned} \tag{117}$$

The solution for the velocity distribution in the tube is then:

$$v_z(r) = \frac{R^2 \Delta p}{4\eta L} \left(1 - \frac{r^2}{R^2} \right) \tag{118}$$

A.4 Regression functions for the test fluid properties used for the capillary rise experiments

Variables:

T ... Temperature [°C]

η ... kin. Viscosity [mPa·s]

γ ... Surface tension [mN/m]

ρ ... Density [g/cm³]

n-Decane (DEC)

$$\eta = -1.624 \cdot 10^{-10} T^5 + 4.230 \cdot 10^{-8} T^4 - 4.693 \cdot 10^{-6} T^3 + 3.547 \cdot 10^{-4} T^2 - 2.381 \cdot 10^{-2} T + 1.279 \quad (119)$$

$$\gamma = -9.200 \cdot 10^{-2} T + 2.567 \cdot 10^1 \quad (120)$$

$$\rho = -5.136 \cdot 10^{-7} T^2 - 7.164 \cdot 10^{-4} T + 7.441 \cdot 10^{-1} \quad (121)$$

2-Propanol (IPA)

$$\eta = 9.753 \cdot 10^{-8} T^4 - 2.466 \cdot 10^{-5} T^3 + 2.593 \cdot 10^{-3} T^2 - 1.492 \cdot 10^{-1} T + 4.507 \quad (122)$$

$$\gamma = -5.602 \cdot 10^{-6} T^3 + 8.954 \cdot 10^{-4} T^2 - 1.366 \cdot 10^{-1} T + 2.402 \cdot 10^1 \quad (123)$$

$$\rho = -1.352 \cdot 10^{-6} T^2 - 8.507 \cdot 10^{-4} T + 8.036 \cdot 10^{-1} \quad (124)$$

Polydimethylsiloxane (PDMS)

$$\ln(\eta) = 1833 \cdot \frac{1}{T} - 8.473 \quad \eta [Pa], T [K] \quad (125)$$

$$\gamma = 20.9 - 0.0463 \cdot (T - 25) \quad \gamma [mPa \cdot s], T [°C] \quad (126)$$

$$\rho = 0.964 \quad \rho [g/cm^3] \quad (127)$$

Publications

The following objects were published in the course of the research work for this dissertation.

Research articles:

Blöchl, Y. and Schledjewski, R.: A robust empirical model equation for the compaction response of textile reinforcements, *Polym. Compos.*, 2020. (DOI: 10.1002/pc.25825)

Blöchl, Y., Hegedüs, G., Szebényi, G., Tábi, T., Schledjewski, R., and Czigany, T.: Applicability of fiber Bragg grating sensors for cure monitoring in resin transfer molding processes, *Journal of Reinforced plastics and composites*, 2020. (DOI: 10.1177/0731684420958111)

Szebényi, G., Blöchl, Y., Hegedüs, G., Tábi, T., Czigany, T., and Schledjewski, R.: Fatigue monitoring of flax fibre reinforced epoxy composites using integrated fibre-optical FBG sensors, *Composites Science and Technology*, 199, 2020. (DOI: 10.1016/j.compscitech.2020.108317)

Anusic, A., Blöchl, Y., Oreski, G., and Resch-Fauster, K.: High-performance thermoset with 100 % bio-based carbon content, *Polymer Degradation and Stability*, 181, 2020. (DOI: 10.1016/j.polymdegradstab.2020.109284)

Conference contributions:

Blöchl, Y. and Schledjewski, R., "Natural fiber textile characterization for dual-scale flow prediction," in *Proceedings of the 18th European Conference on Composite Materials (ECCM18)*, European Society for Composite Materials (ed.), 24.-28. June 2018, Athens, Greece.

Blöchl, Y. and Schledjewski, R., "Analysis of the spontaneous, capillary driven wetting behaviour in reinforcing textile structures," *14th International Conference on Flow Processes in Composite Materials (FPCM14)*, 30. May – 1. June 2018, Luleå, Sweden.